THE UNIVERSITY *of* EDINBURGH

Dynamical effects of satellite accretion on the Milky Way

Rashid Ibrahim Saad Yaaqib

Doctor of Philosophy
The University of Edinburgh
November 2025

Abstract

ΛCDM cosmology predicts that galaxies grow through the process of hierarchical structure formation. In the Milky Way (MW) galaxy, evidence of satellite accretion is present through observations of stellar streams in the outer halo, and chemo-kinematically distinct stellar populations in the inner regions. Recent surveys of the MW stars such as *Gaia* and the Sloan Digital Sky Survey (SDSS) provide an unprecedented view of the kinematic structure of stars in the MW halo and disc. In this thesis, I explore through simulations and data the small and large scale dynamical signatures arising in the kinematics of stars due to the infall of satellites.

In Chapter 2, I explore the dynamical effects of perturbations on the galactic disc. At relatively small galactic scales, perturbations to the galactic disc show distinct features in the vertical position-velocity structure. Data from the *Gaia* mission shows prominent phase-space spirals that are the signatures of disequilibrium in the MW disc. In my work, I explore a novel perspective of phase-space spiral in angular momentum (AM) space. Using *Gaia* DR3, I detected a prominent AM spiral in the solar neighbourhood. I demonstrate in this Chapter the relationship between the well-known $z-v_z$ spiral and the AM spiral. I show how $z-v_z$ maps to AM through simplifying assumptions. Further, by analytic modelling the orbits of stars in AM, I develop a generative model for the spiral where the disc is perturbed by a bulk tilt at an earlier time. My model successfully produces a winding spiral that varies with L_z and generally matches the salient features in the data across most L_z bins, though only a *chi-by-eye* fit. I find that modelling the phase spiral in AM is a promising method to constrain the timing and magnitude of the disc perturbation, and simultaneously fit MW disc potential parameters. The AM framework simplifies the interpretation of the phase spiral and offers a robust approach to modelling disequilibrium in the MW disc using all six dimensions of phase space.

Large scale perturbations, such as those arising from the infall of the Large Magellanic Cloud (LMC) into the MW, also leave distinct kinematic features in the outer halo of the MW. In Chapter 3, I measure the kinematic signature arising from the MW disc moving with respect to the outer stellar halo, which is observed as a dipole signal in the kinematics of stellar halo tracers and is called the reflex motion. I quantify how the reflex motion varies as a function of Galactocentric distance, finding that (i) the amplitude of the dipole signal increases as a function of radius, and (ii) the direction moves across the sky. I then compare the reflex motion signal against a compilation of published simulations that follow the MW–LMC interaction. These models show a similar trend of increasing amplitude of the reflex motion as a function of distance, but they do not reproduce the direction of the disc motion with respect to the stellar halo well. I also measure mean motions for the stellar halo as a function of distance, and discover radial compression in the outer halo and non-zero prograde rotation at all radii. By analysing a suite of n-body simulations in the literature, and measuring the reflex corrected bulk motions, I found that the compression signal is also present in MW–LMC models. On the other hand the rotation is not present, which suggests that it is not induced by the LMC. To validate the technique of measuring reflex, I constructed idealised tests and analysed the effects of sky coverage, binning and uncertainties in the data. I discuss prospects for directly constraining the mass and orbital history of the LMC through the impact on the motion of the MW stellar disc, and how the modelling of the reflex motion can be improved as more and better data become available.

Following the work in Chapter 3 that identified a wide range of reflex- and bulk- motions measure in literature simulations. In Chapter 4, I investigate the variation of the reflex and bulk motions in the MW halo as a function of the density profile in the outer MW, motivated to understand how the reflex motion responds to assumptions of the MW halo model. I model the MW halo as a broken NFW profile, where the outer halo is a power law beyond some characteristic break radius. I then used the analytic model to generate initial conditions and run a suite of simulations in basis function expansion code `EXP` . Each successive simulation had a MW halo with a steeper slope past the break radius. I then compute the reflex motion parameters for each simulation at the present day. I find that the amplitude of the reflex motion is not sensitive to a wide range of outer halo truncations with fixed LMC mass, while the MW–LMC mass ratios vary significantly due to the changing MW halo profile. To quantify the density perturbations, I analysed the basis function expansion coefficients,

which encode the gravitational response. The result reveals systematic effects with stronger outer halo truncations. I find that a stronger outer halo truncation produces a smaller dipole distortion, while the quadrupole becomes stronger. I also find the signatures of a halo instability, arising from the truncation of the halo, whose oscillation frequency increases with increasing truncation slope.

In the final Chapter, I conclude the thesis and provide a future outlook on the research, building on the wealth of results and insights built throughout this thesis.

Lay Summary

The Milky Way (MW) galaxy is a vast system composed of billions of stars; it is also the system in which our solar system resides. We now know that the Universe is comprised of billions of galaxies, yet vast distances separate our galaxy from the rest. In our cosmic backyard, we have a unique opportunity to learn about how galaxies in the Universe evolved by observing our own.

In the past, it was thought that the Milky Way galaxy was an isolated system, and the development of research on the MW proceeded with this idea in mind. The assumption of an isolated system paved the way for the development of mathematical relations between properties we can observe and models we can use to study the Galaxy. These isolated models of the galaxy were static in time and could be used to answer questions such as: *What is the velocity of a star at some distance* r*?*, *How many stars should I expect at any given distance?*, or *How bright is the Milky Way given a specific distribution of stars?*

While these models were extremely useful in learning about our galaxy, recent data from *Gaia* of the MW disc and halo stars from the Sloan Digital Sky Survey (SDSS) have challenged the state-of-the-art isolated/static models. This thesis studies how the satellites of the MW affect the 'expected' quantities derived from these models. I explore alternative models for different parts of the MW that could explain these time-varying features. I also explore the signature left by satellites during their interaction on the velocities of MW stars.

In Chapter 2, I study the effect (that can arise from the MW interacting with the Sagittarius dwarf galaxy, a satellite of the MW) of perturbations to the disc of the MW, and how these perturbations have a distinct signature in the angular momentum of stars in the disc. In the *Gaia* data, it was discovered that if we plot the z coordinate of MW disc stars versus their corresponding vertical velocity v_z, a spiral pattern emerges. To get a better picture of what causes the

spiral, we can imagine that the disc is a body of water that is rotating. If I then throw a pebble into the rotating disc (water), ripples flow outward and create waves. Because the disc is rotating, these waves shear and, over time, form a spiral pattern in the vertical coordinates. While many studies have modelled this pattern in the vertical coordinates, not many studies have treated the problem in full, as the data also show that there is a spiral in the radial coordinate and velocity (akin to shaking the rotating body of water perpendicular to its rotation axis). In this chapter, I present a new way to model both the radial and vertical patterns through modelling the spiral feature in angular momentum space. Using my model, I show that the angular momentum model can reproduce the main features of the spiral pattern observed in the data. The model I use also gives us valuable insight about the MW disc. In order to match the spiral pattern, the model requires the specification of the MW disc parameters such as its mass and shape, and also the time when the MW disc was perturbed. I find that the timing of the perturbation of the disc is in agreement with the last closest approach time of the Sagittarius dwarf galaxy.

On galactic scales, these time-varying features like the spiral occur over relatively small distances. However, studies show that the influence of satellites can also be felt on much larger scales—particularly in the outer halo of the MW, where stars take billions of years to complete a single orbit. In Chapter 3, I turn my attention to this large-scale region and study the reflex motion of the Milky Way disc: a subtle "wobble" that arises from the gravitational pull of the Large Magellanic Cloud (LMC), the most massive satellite of the MW.

The MW is usually decomposed into multiple components, two of which are the disc and the dark matter (DM) halo. The former extends only to about ~ 15 kpc in size, while the latter reaches out to ~ 300 kpc. The LMC today is at its pericentre (the point of closest approach) at a distance of ~ 50 kpc. The satellite exerts a gravitational pull on the different parts of the MW. The time it takes these different parts to respond is related to how long stars take to orbit in the disc and halo. In the outer MW halo, stars take more than a billion years to complete an orbit, while in the disc, the timescale is approximately five times shorter. This differential response causes the disc to jerk in the direction of the LMC, while the outer halo has not yet responded. This relative motion between the disc and halo is termed *reflex motion*. It has a measurable signature for observers (like us) in the disc: when looking at stars in the halo, part of the halo appears to move towards us, and on the opposite side, it appears to move away.

The speed at which the halo stars seem to move closely matches the speed of the disc motion induced by the LMC.

To measure this motion, I use a sample of over 4,000 halo stars from SDSS/SEGUE, split into four distance bins ranging from 20 to nearly 60 kiloparsecs. The splitting of the data into distance bins compares the motion of the disc against parts of the halo where the response timescale is similar to the disc itself (at 20 kpc), and where the halo lags the most in its response (60 kpc). If the MW disc is being displaced by the LMC, then distant stars in the halo should appear to move in the opposite direction—producing a measurable velocity dipole. The expectation is that parts of the halo that respond like the disc (i.e., at 20 kpc) will produce a small relative motion, while parts of the halo that lag the most (60 kpc) will produce the largest relative motion.

My results show that the amplitude of the reflex increases with distance: from 16.9 km/s at 25 kpc to over 40 km/s at 59 kpc, consistent with expectations that the disc's motion relative to the inertial outer halo grows over time. I also find that the apex of the motion—its direction on the sky—shifts gradually with radius, aligning more and more with the past orbital path of the LMC. This agreement offers strong evidence that the LMC is indeed responsible for this large-scale dynamical signature. It also provides a way to learn about the past trajectory of the satellite.

In addition to the disc's motion, I also measure the internal motions of the halo itself. I find a consistent radial infall velocity of about -27 km/s at 45 kpc, suggesting that halo stars are 'falling inward' due to the mass that the LMC has added to the MW. Moreover, I detect a small but significant prograde rotation in the halo of around -24 km/s, which is not predicted by isolated halo models and adds another clue that the halo is far from equilibrium.

Furthermore, to interpret these findings, I compare the measured reflex motion with simulations of the MW–LMC interaction. I test several models—ranging from analytic approximations to fully self-consistent N-body simulations—and show that while many models can recover the trend of increasing reflex amplitude, they often fail to match the exact direction of motion I observe. This mismatch highlights the need for improved modelling and shows that reflex motion offers a new and powerful constraint on the MW–LMC system.

Finally, in Chapter 4, I aim to understand how the choices of the MW halo model affect the reflex motion direction and magnitude that was found in Chapter

3. I performed 11 fully self-consistent N-body simulations of the MW–LMC interaction, modelling the system from > 2 Gyr ago to the present day. Each simulation used the same LMC model, but I systematically altered the Milky Way halo by truncating ("chopping off") its density profile at ~ 50 kpc while increasing how strong the truncation is. This allowed me to isolate how the extent of the MW halo influences the resulting reflex motion.

In this experiment, I found that truncating the MW halo has a strong effect on where the velocity dipole points relative to the intermediate parts of the halo. I also found that by truncating the halo, the MW becomes unstable and shows expansions and contractions with time—even in the absence of the LMC. I also find that the LMC causes the initially spherically symmetric distribution of the MW halo to become lopsided, where the amount of asymmetry is correlated with the amount of material in the outer halo.

In summary, the results of this thesis demonstrate that the Milky Way is not a static or isolated galaxy. It is still responding dynamically to the gravitational forces of its satellites—whether in the form of ripples in the disc or reflex motion on halo-wide scales. These time-dependent signatures, now directly observable thanks to modern surveys, provide a new way to test models of our galaxy and its interactions. I highlight the need to move away from static and isolated MW models by showing (and interpreting) the effects of satellites on the MW galaxy.

Declaration

I declare that this thesis was composed by myself, that the work contained herein is my own except where explicitly stated otherwise in the text, and that this work has not been submitted for any other degree or professional qualification except as specified.

The text in Section 2.4.1 and Section 2.4.3 was composed mostly by Aneesh Naik (second Author) as part of the publication.

Chapters 2, 3 and 4 of this thesis has been published in the *Monthly Notices of the Royal Astronomical Society* are available in Yaaqib et al. (2025a), Yaaqib et al. (2024a) and Yaaqib et al. (2025b).

(*Rashid Ibrahim Saad Yaaqib, November 2025*)

Acknowledgements

I am extremely grateful for the support of my supervisor Jorge Peñarrubia who has guided me throughout the PhD. You have passed down to me more wisdom than I could remember and showed me how to be an effective researcher. I am grateful for your time, for the countless tangents on angular momentum and Fourier space and showing me that I can keep focused on my PhD even when exploring new ideas. I am grateful for the walks around Blackford Hill that we called meetings, and your suggestion to take these meetings outside in the first place.

I am also grateful and deeply in debt to my advisor Michael Petersen. Thank you for taking me under your wing and teaching most of what I know about simulating galaxies. Thank you for giving me opportunities to work on other projects and giving me many occasions to broaden my skill set. Thank you for sharing your amazing coffee and pointing me to the sources. Thank you for being a positive academic (and non-academic) role model. I am and will always be grateful for your effort and time and hope only to reciprocate in the future.

I am forever grateful for the love, care and support of my beautiful wife Maithah. There are no combinations of words that will come close to expressing the gratitude I have for you. Thank you for putting up with my insomniac sleeping schedule. Thank you for being patient during this time period when we are far away. Thank you for ordering me groceries when I have been too stressed, and your amazing recipes. Thank you for lifting my spirits everyday. Thank you for making my days brighter and life more colourful than ever. I am truly lucky to have you by my side.

I would also like to thank my family, parents and siblings for their support during my academic journey. In particular, my brothers Saad and Amin, for always being there to impart wisdom, providing support and keeping me motivated on my journey.

I would like to also thank the many PhD students I have met over the years who have made being at the Institute for Astronomy a wonderful experience. Ryan Begley - your friendship over the years has been invaluable, thank you for listening to my rants and being someone I could always lean on for support. Thank you also to Althea Lai, Lea Ferrelic, Thomas Stanton, Callum Donnan for being the best office neighbours. Thank you for your kindness, for the positive atmosphere

you foster wherever you are and for always agreeing to coffee breaks.

Finally, I would like to thank the members of the Dynamics Tea reading group Simon Rozier and Aneesh Naik and the rest. Our weekly meetings has been a great source of inspiration and learning. Your collective questions during my presentations have helped me tremendously in my confidence and abilities.

Contents

List of Figures

List of Tables

Chapter 1

Introduction

The Milky Way (MW) galaxy has long been at the forefront of astrophysical interest. Its striking appearance in the night sky—before the widespread impact of light pollution—has inspired similar etymologies across many languages. In in Arabic it has been called the "Straw Path" (*darb at-tabbāna*; Toivanen & Sipila, 2025). Long before the advent of telescopic equipment and the Newtonian revolution in astrophysics, this luminous cloud stretching across the sky was the subject of countless origin myths. The term "Milky Way" itself traces back to Greek mythology. Today, we understand the MW as our galactic home—the vast system made of billions of stars in which our solar system resides.

While the MW's appearance was once a source of myth and legend, it is now a subject of scientific inquiry. Since the earliest efforts to systematically observe the Galaxy, models have been essential to interpreting the available data. In the beginning, when observations were limited and coarse, only simple models were required. But as observational capabilities advanced, so too did the need for more sophisticated frameworks.

This thesis is primarily concerned with the modelling of the MW. To set the stage for the remaining chapters, I provide here an overview of how MW modelling has evolved in step with increasingly precise and extensive observations. I highlight the strengths of equilibrium models and motivate the transition to disequilibrium frameworks based on both theoretical developments and observational discoveries. This leads to the central focus of this thesis: the study of dynamical disequilibrium features imprinted on the MW through interactions with satellite galaxies.

As the chapters in this thesis are (mostly) self consistent, this Chapter aims to provide historical context on how galaxies (in particular the MW) are modelled at present, and the progression of mass models of Galaxies and the MW. I also motivate the need for the science presented in Chapters 2-4 through new insights gained from the abundance of data available today on MW stars.

1.1 Early Models of the Milky Way

In the early 20th Century, our understanding of our place in the universe was transformed by the confirmation that many of the nebulae observed in the sky (unresolved or blurry sources in the sky) were all themselves galaxies (Hubble, 1929) and all receding from us in what was now termed Hubble's Law. Early observations of galaxies produced a classification system that was convenient for categorising the diversity of galaxies we observe. The Hubble classification scheme (Hubble, 1926), shown in Figure 1.1, categorises galaxies as being either elliptical, spiral or irregular. Spiral galaxies were further split into a barred category. While these classifications were visual, these galaxies (as we know now) are dynamically distinct. For example, spiral or disc galaxies are rotationally supported (ordered motion) while elliptical galaxies has little to no rotation and supported by a large velocity dispersions (random motions). Furthermore barred spiral galaxies are dynamically distinct than their spiral siblings, as the bar introduces changes to the disc dynamics in via the gravity of the rotating bar acting on the remainder of the disc.

The modelling of galaxies during this period proceeded on two fronts, the observational front and the theoretical one. In the former, attempts to characterise the light profile of galaxies was promising (Sersic, 1968; de Vaucouleurs, 1948) where an analytic form of the light profile of galaxies we observe in projection was developed. This was a major step forward in understanding the structure of galaxies. An example parameterisation of the surface light profile of galaxies, that is still used today, is the Sersic profile (Sersic, 1968). This profile describes the surface brightness of a galaxy as a function of radius, and is given by

$$I(R) = I_e \exp\left(-b_n \left(\frac{R}{R_e}\right)^{1/n}\right). \tag{1.1}$$

PLATE XIII

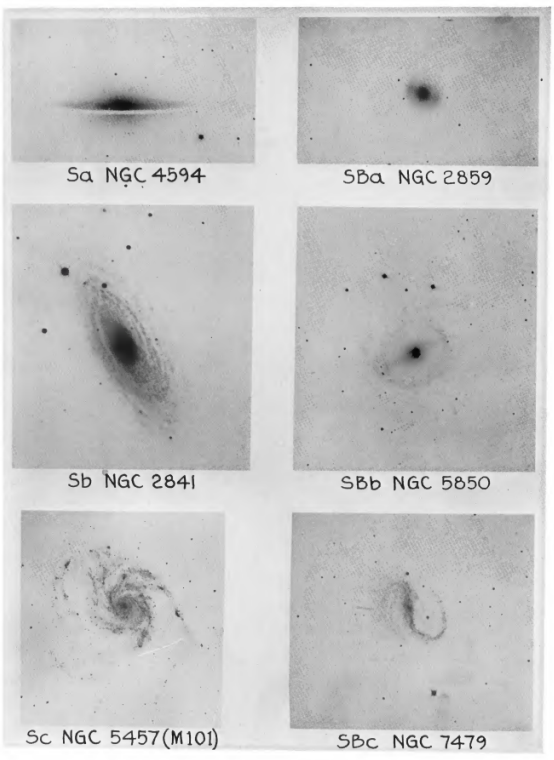

NORMAL AND BARRED SPIRALS

TABLE V

FREQUENCY DISTRIBUTION OF TYPES

Type	Number	Percentage	Mean Mag.
Elliptical Nebulae			
E0	17	18	11.40
1	13	14	11.43
2	14	15	11.52
3	10	11	11.99
4	13	14	11.95
5	6	6	10.97
6	7	8	10.93
7	5	5	11.02
Pec.	8	9	11.55
Total	93	23*	11.53
Normal Spirals			
Sa	49	21	11.69
b	70	29	11.55
c	115	49	11.75
Pec.	3	1	12.80
Total	237	59*	11.68
Barred Spirals			
SBa	26	44	11.66
b	16	27	11.48
c	15	26	11.87
Pec.	2	3	11.70
Total	59	15*	11.66
Irregular Nebulae			
	11	3*	11.34
Totals			
All types	400	100	11.63

* Percentages of 400, the total number of nebulae investigated. The percentages of the subtypes refer to the number of nebulae in the particular type.

Figure 1.1: Hubble's morphological classification of galaxies, adapted from Hubble (1926). *left*: Examples of galaxies classified as Spirals (Sa-c, first column) where the lower case letter is a visual indication of how spiral the galaxy appears. Barred Spirals (SBa-c, second column) where the lower case letter denotes how barred the spiral appears. *Right*: The frequency table for the sample of 400 galaxies in Hubble (1926).

This profile was best suited for galaxies that were of the 'regular' type, such as elliptical and spiral galaxies. The Sersic index n describes the shape of the profile, with $n = 1$ corresponding to an exponential profile (typical of spiral galaxies) and $n = 4$ corresponding to a de Vaucouleurs profile (typical of elliptical galaxies). The parameters I_e and R_e are the surface brightness and effective radius, respectively.

The light distribution of a galaxy is not only a descriptor of the light, but can also be related directly to the mass distribution of the galaxy if one makes some assumptions. The mass distribution of a galaxy is a key factor in understanding its dynamics and evolution. It can be inferred from the light distribution using the assumption of a mass-to-light ratio, whereby a constant mass-to-light ratio is a reasonable approximation for many galaxies. However, this assumption breaks down for galaxies with significant dust content or for galaxies that are not in

equilibrium. The relation between the surface brightness $\Sigma(R)$ and the 3D mass density is given by

$$\Sigma(R) = \Upsilon \int_{-\infty}^{\infty} \rho(R, z) dz \ . \tag{1.2}$$

Where Υ is an assumed mass-to-light ratio and $\rho(R, z)$ is the 3D mass density of the galaxy. The explicit integral over z assumes that the z-axis of the galaxy is aligned with the observer line-of-sight. This relation is used to infer the mass distribution of galaxies from their light distribution. Such connection between the light and mass was the key to understanding the dynamics of galaxies, and it was the foundation for the development of equilibrium models.

In galactic dynamics, given a density distribution $\rho(r)$ we can infer through Poissons equation the gravitational potential $\Phi(r)$

$$\nabla^2 \Phi = 4\pi G \rho \ . \tag{1.3}$$

This equation relates the gravitational potential to the density distribution of the galaxy.[1] We can go even further, under this assumption and calculate for a given density profile the circular velocity profile as follows

$$v_c(r) = \sqrt{-r \frac{d\Phi}{dr}} \ . \tag{1.4}$$

It is remarkable at this point, that through these relations, we can infer key dynamical quantities of a gravitational system in equilibrium. The simplicity of this approach paved the way for the development of many types of equilibrium models, which I will now discuss in more detail.

Self-gravitating systems in the universe exist on many different scales each of which requires different treatments owing to their size and complexity. The solar system is an example of gravitation on the smallest scales. Gravity here can be described as was first proposed by Isaac Newton in his seminal manuscript "*Philosophiæ Naturalis Principia Mathematica*"(Newton & Cotes, 1713). In the

[1] G is the gravitational constant.

solar system, most of the mass is concentrated in the sun (99.86%). In this case, the potential in the solar system can be approximated by the potential of a point mass. We can perform, in this case, the exercise of the solving Poisson's equation straightforwardly, assuming that all the mass distribution in the solar system is $\rho(r) = M_\odot \delta(r)$, where $M_\odot$ is the sun's mass and $\delta(r)$ is the Dirac delta function. Solving Equation 1.3 with the aforementioned density profile yields

$$\Phi(r) = -\frac{GM_\odot}{r} \ , \tag{1.5}$$

and a circular velocity in the solar system of

$$v_c(r) = \sqrt{\frac{GM_\odot}{r}} \ . \tag{1.6}$$

With a few simple steps, I can now write the (circular) velocity of stars at a given radius r in the solar system given the Sun's mass.[2] This neat set of steps can be repeated for density profiles more suited to describing systems on the larger scales - galaxies, in particular the MW galaxy. In the following subsection I will introduce equilibrium models of the MW galaxy that have been built to match the observed velocity curve of the MW stars in data.

1.1.1 The density profile of the Milky Way

Given that the Poisson equation in Eq. 1.3 is a linear partial differential equation, a galaxy can be split as the sum of its components, where components may be conveniently defined. Two of the main components usually used for galaxies are the disc and a Dark Matter (DM) halo. The latter component came only after the discovery of DM. Let us do a simple exercise of building a velocity curve using a Plummer sphere density distribution, that fits well the observational density distribution of globular clusters. Using the same steps as in the previous section we start with a Plummer sphere density profile (Plummer, 1911a)

[2] In many applications e.g. sending a satellite into interplanetary space - the gravitational perturbations of the planets are very important when requiring 100s or even 1000s km accuracy for trajectories.

$$\rho(r) = \frac{3M}{4\pi b^3}\left(1 + \frac{r^2}{b^2}\right)^{-5/2} \quad , \tag{1.7}$$

where M is the total mass and b is the scale radius. Now, we solve Poisson's to find the potential

$$\frac{1}{r^2}\frac{d}{dr}\left(r^2\frac{d\Phi}{dr}\right) = 4\pi G\rho(r) \ . \tag{1.8}$$

The first integration step yields the mass profile finding

$$M(< r) = \int_0^r 4\pi r^2 \rho(r)\ dr \tag{1.9}$$

$$= \frac{3M}{b^3}\int_0^r r^2\left(1 + \frac{r^2}{b^2}\right)^{-5/2} dr \ . \tag{1.10}$$

Solving this integral yields

$$M(< r) = \frac{Mr^3}{\left(r^2 + b^2\right)^{3/2}} \ . \tag{1.11}$$

At this point, we could continue to solve for the potential, but since the velocity curve requires only the derivative of the potential (i.e. the mass profile), we can find the circular velocity profile by simple substitution of the potential derivative into the circular velocity Equation 1.4

$$\frac{d\Phi}{dr} = -\frac{GM(r)}{r^2} \tag{1.12}$$

$$= -\frac{GMr}{(r^2 + b^2)^{3/2}} \ , \tag{1.13}$$

and the circular velocity is now

$$v_c(r) = \sqrt{\frac{GMr^2}{(r^2 + b^2)^{3/2}}} \ . \tag{1.14}$$

This characteristic velocity curve, rises linearly at $r \ll b$, peaks at $r = \sqrt{2}b$, and falls off as $r^{-1/2}$ for $r \gg b$. When observing galaxies, we see them only in projection, it is instructive then to project the Plummer density profile to obtain

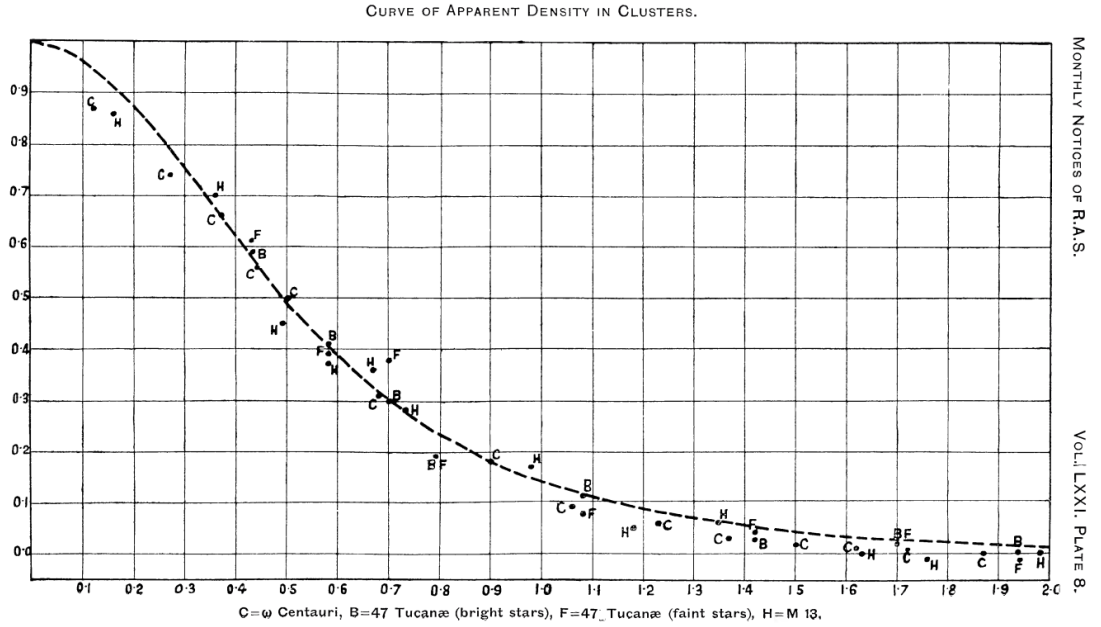

Figure 1.2: This figure, adapted from Plummer (1911a) shows the (scaled) counts of stars at different distances from the centre for three globular clusters ω-Centauri (C), 47 Tucanae (bright stars) (B), 47 Tucanae (faint stars) (F) and M13 (H). The projected Plummer profile showed remarkable agreement with the star counts (or surface density).

the surface density via

$$\Sigma(R) = \int_{-\infty}^{\infty} \rho(r(z))dz \ , \tag{1.15}$$

after some algebra our integrand becomes

$$\Sigma(R) = 2\int_{0}^{\infty} \frac{3b^2M}{4\pi(b^2+z^2+R^2)^{5/2}}dz \tag{1.16}$$

$$= \frac{Mb^2}{\pi(b^2+R^2)^2} \ . \tag{1.17}$$

Where the factor 2 (and changing integral limits) are placed as the profile is symmetric about z. The solution to the integral can be found through trigonometric substitutions. At this point we are well equipped to compare this model with data. Figure 1.2 shows the fit of the surface brightness made by (Plummer, 1911a) to three globular clusters in the MW: ω-Centauri, 47 Tucanae and M13. This profile remarkably fit different clusters extremely well, the implication from their seminal work was that globular clusters follower a universal profile in density. This work was an early example of how a relatively simple mass model for clusters explains the observations well.

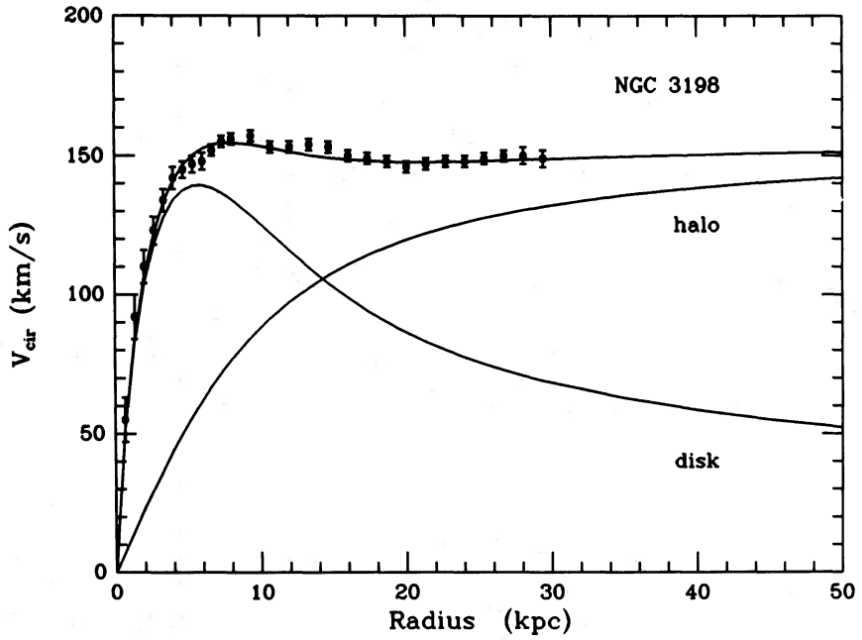

Figure 1.3: The circular velocity curve of NGC 3198 adapted from van Albada et al. (1985). The velocity curve model is comprised of a think exponential disc and a spherical halo model. The inclusion of the halo model remedies the flattening of the velocity curve at large radii.

One of the earliest galaxies with a measured rotation curve was the Andromeda galaxy (M31). In a pioneering study, Babcock (1939) extended velocity measurements of M31 to large radii, well beyond its bright stellar disc. His findings showed that the rotation curve remained flat, or even rose slightly, at large distances— beyond the stellar disc (using the velocity of the gas in M31). At the time of Babcock's paper, Hubble had determined the mass-to-light ratio of M31 to be ~ 0.001 in the innermost region of the galaxy ($< 1'$ about the centre), but this ratio rose to 62 in the outermost region($< 80'$ about the cetnre) when fitting the velocity curve. This order of magnitude increase was questioned by Babcock: "the great range of mass ratio to luminosity in proceeding outward from the nucleus suggests that ... perhaps, new dynamical considerations are required".

This discrepancy was profound. If mass truly followed light, the outer regions of M31 should exhibit falling rotation speeds. Instead, the persistence of high velocities implied the presence of an unseen mass component extending far beyond the optical disc. These early observations were among the first empirical indications of what we now call DM. In the seminal work of Rubin & Ford (1970), the rotation curve of M31 had been extended out to 24 kpc. They found with

certainty that the rotation curve in M31 flattens[3] past the inner regions of the disc. Their work was the first significant evidence of DM. Subsequent studies (Roberts & Rots, 1973; Einasto et al., 1974) confirmed that flat rotation curves were not unique to M31—they were a generic feature of spiral galaxies. No single Plummer sphere, exponential disc, or bulge model could account for the flatness on its own. A new component, now understood as a DM halo, was required to reconcile the observed kinematics with gravitational theory. Figure 1.3 shows the rotation curve of NGC 3198 adapted from van Albada et al. (1985). The inclusion of an additional mass component here reconciled the flattening of the circular velocity in the outer regions of the galaxy. In addition to the previous evidence for DM, other lines of evidence came from observations of galaxy cluster mergers. In Clowe et al. (2006), X-ray observations of the Bullet Cluster revealed the interaction between two colliding galaxy clusters. The X-ray data traced the distribution of hot gas, which contains most of the baryonic matter in clusters, and showed that this gas had been slowed and compressed during the collision. Weak gravitational lensing maps, which trace the gravitational distortion of background galaxies by foreground mass, were then created for the same region. The weak lensing maps revealed the distribution of total mass and traced the gravitational potential. Surprisingly, the gravitational potential peaks were spatially offset from the X-ray gas distribution, instead coinciding with the collisionless matter that passed through the collision largely unimpeded. This spatial segregation demonstrates both the collisionless nature of DM and that it comprises a large fraction of the cluster mass.

DM halo models are most commonly used today work to add non-luminous mass to the outskirts of galaxies to provide mass required to sustain the velocities at large radii. To much surprise, DM is now measured to make up about 85% of all matter in the universe (Planck Collaboration et al., 2020). This profound realisation has galvanised research into the role of DM in the universe, and precisely what its make up is. As of the writing of this thesis, the nature of DM has yet to be uncovered (Feng, 2010) but its effects on both galactic and cosmological scales are now well understood.

To conclude our segue into modelling of disc galaxies, most recent mass models of the MW galaxy decompose the MW into three (sometimes more) main components. In order of distance scales they are the bulge - a centrally

[3]At the time, the flattened parts of the rotation curve were fit with polynomials of order > 3, as DM halo models were not yet used.

concentrated region of stars much smaller than the disc, the disc - the main stellar component of the galaxy extending out to $\sim$ 20 kpc and the DM halo. Each of these components has a characteristic velocity curve, which we have solved only for one (the bulge is usually modelled as a Plummer sphere). To compare velocity curves (and test the mass models) the velocity curves of each individual component can be added in quadrature

$$v_{c,\mathrm{tot}}^2 = v_{c,\mathrm{bulge}}^2 + v_{c,\mathrm{disc}}^2 + v_{c,\mathrm{halo}}^2 + v_{c,\mathrm{gas}}^2 \tag{1.18}$$

all of which are functions of radius, to form the velocity curve of a given galaxy. Figure 1.4 shows the current state-of-the-art galactic rotation curve of the MW galaxy (Eilers et al., 2019a). It shows the decomposition of the total velocity curve, it is evident from the figure that with such precise measurements of the circular velocity, the inclusion of the dark halo is needed nearly all radii. It is also clear that even at 5 kpc, the contribution to the circular velocity curve from the halo component is significant.

Before moving on to explore disequilibrium, it is important to emphasise just how far we can go with equilibrium models. At the start of the subsection we covered spherically symmetric systems, but many (observationally motivated) axissymmetric models exist for the MW halo (e.g. triaxial, oblate or prolate shaped models), and of course, the disc itself has axissymmetric prescriptions. Modern techniques that model the MW leverage multiple components that make up the mass distribution in the galaxy. For example, the `MWPotential2022` in the `Gala` python package (Price-Whelan, 2017) is an example of commonly used multi-component mass model of the MW. It consists of a Herniquist bulge and nucleus, a three component exponential disc matched with Eilers et al. (2019a), and an NFW halo. This (static) potential matches observational data of the circular velocity well, but does not incorporate features such as a galactic bar.

A much more detailed approach to mass-modelling the MW is taken in `AGAMA` (Vasiliev, 2019), which is a general-purpose software library for stellar dynamics. `AGAMA` provides a framework for the creation of arbitrarily complex potentials, including time-dependant features such as bars. In Hunter et al. (2024), `AGAMA` was used to perform hydrodynamical simulations of the MW, where the potential was decomposed as i) supermassive black hole ii) nuclear stellar cluster iii) nuclear stellar disc iv) rotating galactic bar v) stellar galactic disc vi) two-component gas

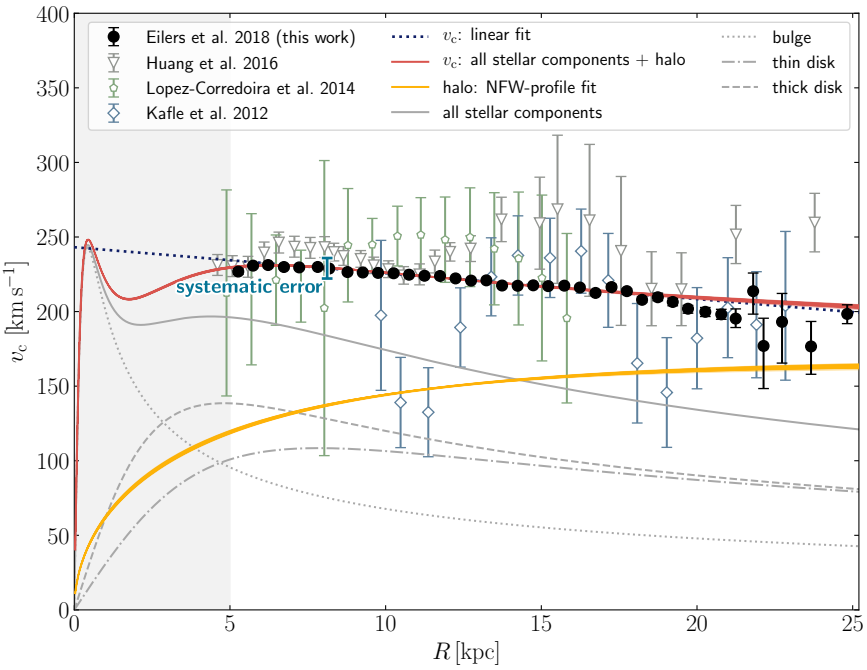

Figure 1.4: The MW rotation curve adapted from Eilers et al. (2019a). The data are shown in scattered points from Eilers et al. (2019a) and others. The total velocity curve shown in the solid red line is a combination of a four-component model made of a thick disc, thin disc, bulge and NFW halo. The contribution from the dark halo becomes important even at radii smaller than 15 kpc, then becomes the dominant source of the velocity curve beyond 15 kpc.

discs vii) spiral arms viii) DM halo. The parameters of each component were set by the parameters of existing detailed studies of those regions and/or fit the data directly. While in Hunter et al. (2024) a hydrodynamical simulation was run in this potential to systematic uncertainty in kinematic distance measurements of gas in the MW, the use of this time-evolving potential (where the bar is rotating, but all other parts are static) is an excellent example of pushing (semi-)static MW models to the limits and using them to make inferences on observations or develop intuition about observations of the MW.

1.2 From Equilibrium to Cosmological Context: The Role of Structure Formation on Dynamics

1.2.1 The success and challenges of equilibrium models

In the context of collisionless gravitational systems, the ergodic hypothesis postulates that the long-term time average of a star's observable properties (e.g. its position or velocity) is equivalent to an ensemble average over phase space. This assumption underpins many models of stellar systems, allowing us to statistically describe the structure and kinematics of galaxies without solving individual trajectories.

If a system is in equilibrium and the potential is time-independent, it is often assumed to be ergodic (or approximately so). Functionally, this means that instead of waiting a long time to infer, for example, the density profile of a galaxy from the trajectory of a single star, we can sample a population of stars at a single time since they are representative of the full phase-space distribution. This property - ergodicity - is the assumption that underpins the comparison between a static model and observations.

I notice at this point that these galactic models—some of which I have shown how to extract kinematic quantities from—are extremely useful, particularly because many (though not all) have analytically integrable or differentiable forms. Beyond their mathematical tractability, they are also *stationary in time*. Time-independence is a reasonable assumption when modelling the present-day state of the Galaxy,[4] but within a cosmological context, galaxies evolve continuously

[4]We will see why this also eventually becomes problematic!

over cosmic time.

Here, I will put into context the challenges to equilibrium models through the lens of cosmology, briefly covering the expectations put forth by structure formation theory for galaxies like the MW.

In the ΛCDM framework, galaxies form hierarchically through the accretion and merger of smaller structures (White & Frenk, 1991). For any galaxy we observe today, its growth history—the accretion history—describes how it accumulated mass over time. Cosmological simulations show that the mass spectrum of accreted satellites follows a steeply declining power law, where most mergers involve low-mass satellites (typically contributing less than 1% of the host's mass) (Bullock & Johnston, 2005; Cooper et al., 2010). Nevertheless, occasional high-mass mergers dominate the structural evolution of the stellar halo and can leave strong dynamical signatures.

The implication is that the MW did not form as a pristine, isolated object. Instead, it is the result of repeated gravitational interactions between smaller galaxies and their DM halos. This stands in contrast to the assumptions made by equilibrium models, which treat the Galaxy as a stationary, time-independent system, largely unperturbed by its surroundings.

These two perspectives—hierarchical accretion and dynamical equilibrium—are fundamentally in tension. While equilibrium models have been remarkably successful in reproducing many properties of the MW, ΛCDM cosmology challenges their foundational assumptions by emphasizing the inherently time-dependent and interactive nature of galaxy formation. Reconciling these views is central to understanding the MW as both a snapshot in time and a product of its cosmological history. To set the context for the later chapters in the thesis, I will introduce two features of disequilibrium that have been detected in the MW disc (small scale) and halo (large scale).

1.3 Small-Scale Disequilibrium: Phase-Space Spirals

In an idealised, smooth, axisymmetric model of the MW disc, the motions of stars are highly ordered. In such a system, if one constructs spatially binned maps of

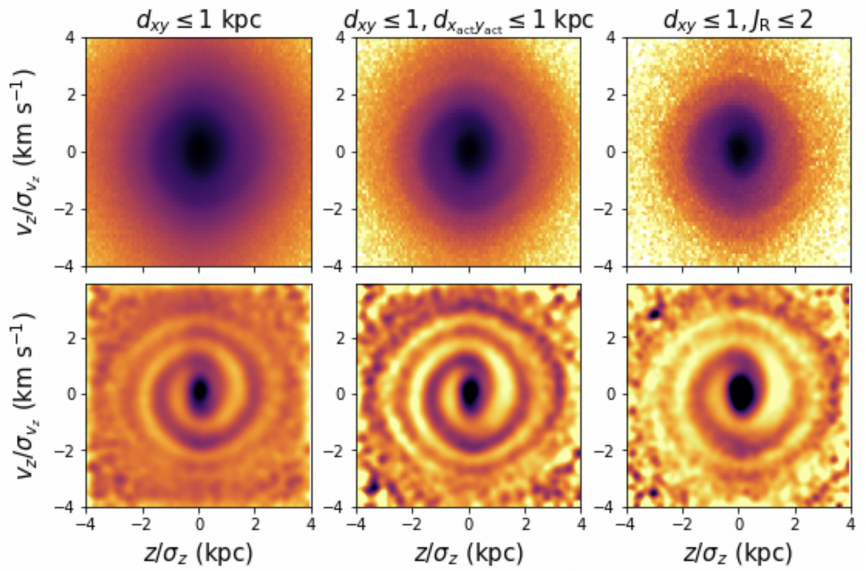

Figure 1.5: The $z - v_z$ spiral in *Gaia*, adapted from Hunt et al. (2022). The first column contains only stars within a 1 kpc cylinder about the Sun. The second column contains stars also within 1 kpc but their distance is instead computed through their actions. The right column shows stars within 1 kpc of the sun, but keeping only stars with a low radial actions J_R. The bottom row is identical in selection to the top row except a smooth Gaussian background has been subtracted which enhances the ridges of the spiral.

stellar velocities in the disc would show mean radial and vertical velocities close to zero, while azimuthal velocities would vary predictably with radius (depending on the choice of disc potential). If the MW were perfectly symmetric and in dynamical equilibrium, the kinematics of stars in the solar neighbourhood would be unremarkable. However, as has often been the case in astronomy, the data tell a different story.

The most transformative dataset for MW stellar kinematics comes from the European Space Agency's *Gaia* mission. As of the time of writing, Gaia DR3 has provided a six-dimensional phase-space catalogue for over 34 million stars (Gaia Collaboration et al., 2023), the vast majority of which lie within the disc of the MW. A large subset of these stars resides in the solar neighbourhood, enabling an unprecedented view of local disc dynamics.

Among the surprising features revealed by Gaia was the discovery of a striking spiral pattern in the vertical phase-space distribution of stars (Antoja et al., 2018). When plotting the vertical position z versus vertical velocity v_z of stars within ~1 kpc of the Sun, an overdensity relative to the background in the form of a spiral becomes apparent (see Figure 1.5). This phase-space spiral is not a

feature one would expect in an axisymmetric, equilibrium disc. Instead, it is a clear signature of vertical disequilibrium and ongoing dynamical evolution.

The physical origin of this spiral lies in the process of phase mixing. When a collisionless stellar system is perturbed out of equilibrium—such as by the passage of a satellite galaxy—stars at different radii respond with different vertical oscillation frequencies. This leads to a winding spiral pattern in z–v_z space, which becomes visible when the background stellar distribution is subtracted (Tremaine, 1999; Candlish et al., 2014b).

To illustrate this behaviour more concretely, consider a single star oscillating vertically about the disc mid-plane (as it moves along a circular orbit). Its vertical position as a function of time is

$$z(t) = z_0 \cos(\Omega_z t + \phi) \ . \tag{1.19}$$

Where z_0 is the amplitude of oscillation (i.e. the maximal height of the star above the plane), Ω_z is the vertical frequency, and ϕ is the phase offset. Taking the time derivative, the corresponding vertical velocity is

$$v_z(t) = \frac{dz}{dt} = -z_0 \Omega_z \sin(\Omega_z t + \phi) \ . \tag{1.20}$$

Together, these equations describe an elliptical trajectory in the z–v_z plane:

$$\left(\frac{z}{z_0}\right)^2 + \left(\frac{v_z}{z_0 \Omega_z}\right)^2 = 1 \ . \tag{1.21}$$

Thus, an individual unperturbed star traces a closed loop in vertical phase space.

Now consider an ensemble of stars, each with slightly different oscillation amplitudes, frequencies, and phases. In equilibrium, the phases are randomly distributed, and the overall distribution in z–v_z space appears smooth and symmetric. However, if a perturbation acts to coherently shift the vertical motions—such as the passage of a satellite galaxy perpendicular to the disc

plane—then a correlation is introduced between the phases. As the system evolves, stars with different vertical frequencies begin to wind around phase space at different rates. The vertical frequency can be computed analytically for some disc models by calculating the free-fall time of a star at some initial height above the disc plane. For a Miyamoto-Nagai disc $\Omega_z \propto z_0^2$ (Candlish et al., 2014a). This means that stars with smaller vertical extent rotate around this phase space slower than stars with larger vertical extents. This process of differential oscillation in vertical phase space shears the initial correlation into a spiral: the phase-space spiral is the observable imprint of phase mixing following a vertical perturbation. I stress here that the above example is an illustrative one, an analytic treatment of the vertical phase space spiral can be found in Widmark et al. (2021).

The question that arises here is - What caused the MW disc to be perturbed in this way?

The most widely supported explanation is the impact of the Sagittarius (Sgr) dwarf galaxy. Sgr is a satellite of the MW that has undergone several pericentric passages, with a pericentre of roughly $15 - 20$ kpc (Laporte et al., 2019; Hunt et al., 2021; Bland-Hawthorn & Tepper-García, 2021). Each of these encounters imparts gravitational perturbations to the disc, exciting both in-plane and vertical motions. Simulations have shown that the timing and amplitude of the vertical phase-space spiral are consistent with such a perturbation occurring approximately 500−800 Myr ago (Laporte et al., 2019; Bland-Hawthorn & Tepper-García, 2021). There are however other mechanisms that can form the spiral such as a slowing galactic bar (Hunt et al., 2022), stochastic heating from DM subhaloes (Tremaine et al., 2023) and torques from a distorted DM halo (Grand et al., 2023).

To date, many studies have explored the vertical oscillations in the disc using both n-body simulations and test particle simulations (Binney & Schönrich, 2018; Bennett & Bovy, 2018a; Bland-Hawthorn & Tepper-García, 2021). On the numerical side, simulations of the Sgr dwarf galaxy's recent passages have been used to track the resulting response of disc stars, reinforcing the idea that satellite perturbations drive the formation of the observed perturbations. On the analytical front, current models have primarily focused on describing vertical phase-space spirals (Widmark et al., 2022b). In addition to structure in $z - v_z$ there are also structures observed in $R - v_r$ which is likely a result of mixing in the radial direction. This structure is expected as in the case of a satellite falling into the MW disc, both vertical and radial forces will be imparted by the satellite onto

the disc. However, few existing analytic frameworks capture the coupled radial and vertical structure of the response (but see a notable exception in Widrow, 2023). This limitation provided the key motivation for Chapter 2 of this thesis.

The presence of the phase space spiral presents challenges for modelling the MW disc on very small scales - assuming a static axissymmetric disc will not do well to explain the data. However, when measuring e.g. the circular velocity curve (See Figures 1.4 and 1.3), which averages the velocity of stars out to large distances. An axisymmetric model here is sufficient to model the data as vertical phase mixing will have a very small effect at the larger scales. The need for time-dependant modelling arises in the case of the phase spiral when equilibrium models are not able to explain data of the MW. Chapter 2 of this thesis is dedicated to investigating this disequilibrium feature using angular momentum space. Describing the phase space spiral in angular momentum incorporates the radial and vertical motions by definition, therefore it is a natural space to model the spiral formation and evolution mechanisms. I develop a new modelling approach that begins with individual stellar orbits and traces how their orbits evolve in angular momentum after application of a global tilt to the disc. An additional novelty of my work is the application of a likelihood-based approach where perturbation parameters (and the galactic potential parameters) can be fit directly to the angular momenta of stars in the MW.

1.4 Large-Scale Disequilibrium: The Reflex Motion of the MW Disc

In galaxies—and perhaps most visibly in disc galaxies—there exist features that break the axis-symmetry often assumed in analytic models. These include spiral arms, bars and warps. Even in the absence of external perturbers, there has long been a need for time-dependent models. Features like bars and spiral arms are not static; they evolve over time and play a significant role in redistributing angular momentum and reshaping stellar orbits within galaxies (Sellwood & Sánchez, 2010). The dynamics of bars and spiral arms is a rich topic in its own right, and much has been done in the way of creating time-evolving models that incorporate the time evolving features on top of static potentials. This section focuses specifically on large-scale disequilibrium sourced by external perturbations—particularly the effect of infalling satellites on an

otherwise equilibrium system.

As established earlier, ΛCDM cosmology predicts that galaxies do not evolve in isolation but are constantly shaped by mergers and interactions. In the case of the MW, these interactions are ongoing. Several satellites are either currently interacting with the Galaxy or show signs of past close encounters (Law & Majewski, 2010a). Of these, the most massive and dynamically influential today is the Large Magellanic Cloud (LMC).

The LMC has been observed in the southern sky since antiquity and is now recognized as the most massive satellite of the MW. It is unique not only for its mass but also for its dynamical context: the LMC has a close companion, the Small Magellanic Cloud (SMC), with which it has likely interacted, and it hosts a system of satellites of its own. Recent studies have shown that a subset of satellites currently in the MW halo may have originally been associated with the LMC, based on stellar population analysis and orbital history (Erkal & Belokurov, 2020; Jethwa et al., 2016; Correa Magnus & Vasiliev, 2022).

The LMC's orbital history (beyond the MW's halo) remains an open question. While the current consensus is that it is on its first infall into the MW, alternative scenarios involving a second pericentric passage have also been proposed (Vasiliev, 2024). The distinction between these scenarios hinges on the total masses of both the LMC and the MW. In a second-infall scenario, the LMC would have passed its first pericentre over 5 Gyr ago at a distance of approximately 100 kpc. At present, it is near pericentre, located around 50 kpc from the Galactic centre, and is moving at a total velocity of roughly 327 km/s.

Historically, the LMC's mass was thought to be only about 1% of the total mass of the MW–LMC system, based on stellar mass and its asymptotic rotation velocity. However, mounting evidence suggests that the LMC is significantly more massive—likely in the range of $(1-2)\times10^{11}\ M_\odot$. For instance, Peñarrubia et al. (2015) applied the timing argument to the MW–LMC–M31 system and inferred a total LMC mass of up to $0.25\times10^{12}\ M_\odot$. The timing argument, first applied by Kahn & Woltjer (1959) to the MW-M31 system, estimates the mass of a binary system from the observed positions and velocities of the galaxies in an expanding universe. In the Friedmann-Lemaître-Robertson-Walker metric, the equation of motion for the separation between two galaxies is

$$\frac{d^2r}{dt^2} = -\frac{GM}{r^2} + H_0^2\Omega_\Lambda r \tag{1.22}$$

where gravitational attraction competes with cosmological expansion. Here H_0 is the Hubble constant and Ω_Λ is the vacuum energy density. The method assumes purely radial orbits and uses the age of the universe($\sim$ 13 Gyr) as the total time available for orbital motion. By using the present-day separations and velocities as initial conditions and integrating the equation of motion backward in time, the observed dynamics constrain the total mass of the system i.e. heavier systems require stronger gravity to reverse the Hubble expansion on the cosmic timescale.

Furthermore, stellar-to-halo mass relations also imply a halo mass an order of magnitude larger than estimates from stellar content alone. Additional constraints from the LMC's own satellite population and internal dynamics also place its mass in this range (see review in Vasiliev, 2023a).

Given this high mass, the LMC must have a significant dynamical influence on the MW. One of the most striking consequences of its infall is the displacement of the MW's disc relative to the halo—an effect known as reflex motion. Simulations by Gómez et al. (2015a) showed that the LMC can displace the centre of mass of the inner 50 kpc of the MW by as much as 30 kpc, at velocities up to 75 km/s, over timescales of 300–500 Myr. This displacement has direct implications for mass modelling of the MW. Studies then showed that failing to account for this motion can lead to an overestimation of the Galaxy's mass by up to 20% (Erkal et al., 2020).

Displacement of the inner halo barycentre also affects the modelling of satellite orbits, such as that of the Sgr dwarf galaxy and its associated tidal debris (Gómez et al., 2015a; Laporte et al., 2019), and imparts bias onto the velocity distributions of stellar streams (Lilleengen et al., 2022; Koposov et al., 2023a). These perturbations produce observable kinematic signatures, most notably a large-scale dipole in the radial velocities of distant halo stars. This effect was first proposed and modelled by Petersen & Peñarrubia (2020b), and subsequently confirmed in data by Petersen & Peñarrubia (2021b), in both satellites of the MW and stellar tracers of the halo. The velocity dipole is a direct manifestation of the reflex motion of the disc with respect to the outer halo.

The dynamical mechanism behind this effect can be understood through the lens of gravitational response timescales. The inner regions of the MW—particularly the disc and inner halo—have relatively short dynamical timescales and therefore respond rapidly to perturbations. The outer halo, by contrast, responds more slowly to the perturber. The dynamical timescale at radius r can be approximated

as for spherical halos:

$$t_{\rm dyn} \sim \sqrt{\frac{r^3}{GM(<r)}} \tag{1.23}$$

For an NFW-like halo, this timescale is approximately < 300 Myr at $r < 30$ kpc, increasing to > 700 Myr beyond 50 kpc. As the LMC approaches pericentre, the inner Galaxy is effectively "dragged" (toward the LMC) while the outer halo lags, creating a differential motion between the disc and the halo. This is the reflex motion: a bulk displacement of the MW disc induced by the gravitational pull of a massive infalling satellite.

In this thesis, Chapters 3 and 4 focus on two key dynamical consequences of the LMC's infall. Chapter 3 quantifies the motion of the barycentre of the MW disc in response to the LMC relative to increasingly large shells of the halo. Orbital timescales of halo stars will vary radially, being comparable to the disc at very small radii. The changing orbital timescales will translate to a variation in the measured velocity dipole signal. I also discover in Chapter 3 a 'compression' of the MW halo in response to the LMC, where I found that stars in the MW halo have -on average- a negative radial velocity. In Chapter 4, I study how the reflex motion changes with systematic variations in the pre-infall profile of the MW halo. I find that depending on what the profile of the MW was, the resulting reflex motion signature varies systematically. The variation in the reflex was found to be tied to the deformations that the halo experiences.

1.5 Implications for Galactic Modelling and the Need for a Holistic Approach

The passage of the LMC is expected to deform the density distribution of the MW halo (Garavito-Camargo et al., 2019a, 2021), with tentative observational detections reported in literature (Conroy et al., 2021a). To model a time-dependent potential, one requires a framework in which the shape of the gravitational potential can evolve dynamically over time.

A promising approach—underpinning the EXP simulation software used in

Chapter 4 to model the MW–LMC interaction—is the basis function expansion (BFE) method (Petersen et al., 2022a). In the BFE framework, the gravitational potential is expanded as a sum over spherical harmonic indices (l, m) and radial basis functions indexed by n, which are eigenfunctions of the Sturm–Liouville equation (of which the Poisson equation is a special case). In this basis, the potential of any given spherical system is fully described by a set of expansion coefficients A^n_{lm}. BFE methods have a long history in modeling dynamically evolving haloes (e.g. Hernquist & Ostriker, 1992).

While the numerical integration details of EXP are beyond the scope of this thesis, the interpretive power of its output is essential to highlight. After running a simulation in EXP, I obtain the expansion coefficients A^n_{lm}, from which I define $A_l = \sum_{n,m} |A^n_{lm}|^2$. This provides a scalar measure of the system's self-gravity within each harmonic subspace l. To quantify the relative contribution of dipolar deformation to the total potential, one simply computes the normalized amplitude $P_1 = A_1/A_0$. Normalization is necessary since A_l is model-dependent and evolves with time as the system responds to perturbations.

Figure 1.6, adapted from Lilleengen et al. (2023), illustrates how the relative power in the dipole and quadrupole components grows over time during the LMC's passage for both the MW and LMC haloes. In their study, the LMC and MW were modelled such that they match the present-day circular velocity curves of each. Using EXP, they calculated the forces exerted by the *deformed* MW and LMC potentials on the Orphan stream and provided a quantitative assessment of deviations in the stream's velocity structure. Their results demonstrate that both the LMC's passage *and* the induced deformation of the MW halo leave measurable imprints on observable stream properties. The BFE approach, as implemented in EXP, thus provides a powerful framework for integrating orbits in time-varying potentials.

The LMC now effects two key parameters of the MW: i) its velocity structure by imprinting a reflex motion signal and ii) its density profile by inducing a dipolar (and quadrupolar) deformation. Following the characterisation of the radial variation of the reflex motion of the MW in Chapter 3. I asked the question - how do the parameters of the MW halo (prior to the infall of the LMC) affect the resulting reflex motion signal?

As I will show in Chapter 3, this question arose naturally because the reflex motion signal (with radius) for many LMC-MW simulations in the literature yielded very

different results - a consequence of pre-LMC infall parameter choices made for the MW and LMC models.

In Chapter 4, I explore the connection between the reflex motion parameters -which is an observable signature- and the deformations to the MW using a series of controlled simulations. A family of MW-LMC simulations are run where each successive MW model has a steeper outer halo profile. I found that the outer halo profile (pre-LMC infall) sets the relative amplitude of the dipole and quadrupole deformations of the MW at present day. Additionally, even though the LMC arrives at (almost) the same position at present day in the simulations, the resulting reflex motion signal systematically changes in the inner MW. I present in Chapter 4 the analysis of these simulations and attempt to connect three concepts: a) the velocity field in the MW, b) the density deformations, and c) pre-infall parameters of the MW halo.

1.6 A Hierarchical View of Disequilibrium: Unifying the Large and Small Scales

By this point, it becomes clear that the evidence overwhelmingly indicates the MW is not in a state of equilibrium. In current literature, these different scales of disequilibrium are often treated independently, with only a few works (Vasiliev et al., 2021) attempting to simulate the MW's interaction with both the LMC and Sgr simultaneously. At smaller scales, particularly within the Galactic disc, clear signatures of phase mixing are present in the vertical and radial kinematics of stars. The discovery of the phase-space spiral in the solar neighbourhood is compelling evidence of phase mixing due to a perturbation of the disc. While at larger scales the LMC is displacing the barycentre of the MW disc and deforming the MW halo potential. In the galaxy, disequilibrium is not just limited to the effects of satellites. In the velocities of disc stars structure is found in the U-V plane of disc stars which can arise as a consequence of the interaction between the galactic bar and disc stars(Dehnen, 2000). In each of these cases, assuming an equilibrium model (e.g. a non-rotating bar or omitting the LMC interaction) will not fully explain the effects we observe today.

However, these phenomena are not separate in origin. They are fundamentally linked by the interaction of the MW with its satellite system in a time-evolving

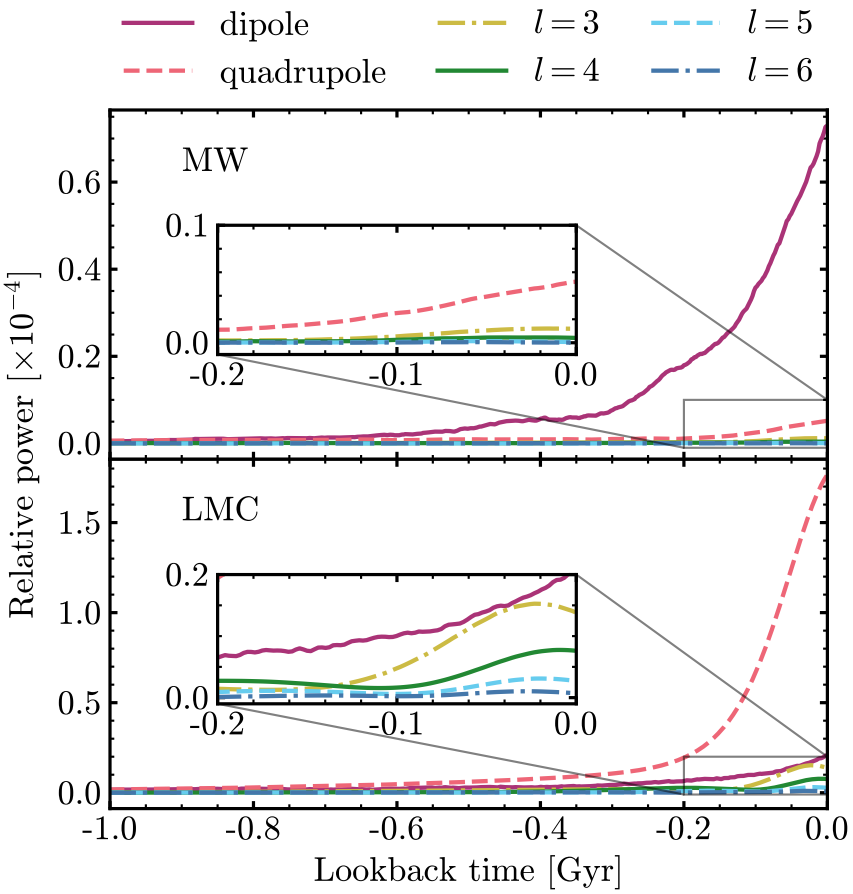

Figure 1.6: The relative power in the dipole and quadrupole of MW-LMC simulations in Lilleengen et al. (2022). The top panel shows the deformations to the MW halo over time using the relative power in the BFE coefficients. The bottom panel shows the same information for the LMC halo. Although this thesis is only concerned with the MW halo, the use of BFE coefficients to characterise deformations also applies to satellites in EXP. The coloured and dashed lines correspond to different types of deformations experienced in the simulations. Most of the deformation in the density of the MW halo is in the dipole term, while the next-largest is the quadrupolar deformation.

gravitational potential. Reflex motion, phase-space spirals, and other non-equilibrium features not addressed in this work are all part of a larger narrative describing the Galaxy's present-day state and its recent dynamical history. A holistic understanding of the MW requires a modelling framework capable of capturing both local and global effects across this hierarchy of perturbations.

Chapter 2

The Angular Momentum Sprial of the Milky Way Disc in GAIA

Foreword

The work that is presented in this chapter was set into motion by a series of curiosities during my PhD. It began first with running trial simulations of the LMC and MW while learning to use the simulation software `exp`. In the first simulation, when looking at movies of the disc during the LMC's passage, I noticed a significant tilting of the disc when the LMC was at pericentre. While not a surprising result, as it is known now that the MW disc is tilted, I was curious whether the a tilted disc has a unique signature in the angular momentum of stars inside the disc. It seemed like a fruitful endeavour at the time. Disc stars have their z angular momentum conserved if they live in an axis-symmetric potential, so if they are in a tilted configuration, their angular momenta may precess or nutate about the disc's z axis. Angular momentum seemed a natural space to study disequilibrium in the disc!

After a brief segue into adopting tilted disc models from literature and measuring their parameters in my simulations (to some success) I moved to angular momentum space. In angular momentum, before the onset of tilting, the angular momentum of disc stars looked like 'blob' in L_x, L_y. Any stars with a non-zero value of L_x, L_y has its angular momentum vector misaligned with the MW z axis. Naively I expected the vector to precess (or form a circle) in L_x, L_y as the star

went around in its orbit. In the absence of tilting, epicyclic motions of stars in the disc will produce incoherent motions in L_x, L_y, and inspection revealed that they simply look like 'blob'. After the LMC passed and the disc reached it's maximal tilt, the whole distribution of L_x, L_y shifted its mean away from zero and began to produce snail-like features. This piqued my interest and I wondered if MW disc star data showed this.

During this investigative work, I presented at our weekly 'Dynamics Tea' meeting movies of the angular momenta of disc stars experiencing a tilt. We spent the better part of an hour trying to explain dynamically why this snail-like feature was the result of a global tilt. During this same meeting, I also presented the angular momentum distribution of 11 million stars in GAIA in L_x, L_y. We (perhaps luckily) did not see the same feature as the one in the simulation. But we did see a clear spiral pattern! This was not so surprising, as a the phase-space spiral had already been discovered in GAIA data. But we had a completely new view of the the disequilibrium feature.

After this point, I set out to develop models that could produce a spiral in angular momentum. Our first ever spiral model, not included in the thesis, was a nested ring model of the disc. Where the precession of each individual ring with different radii would produce a spiral in L_x, L_y. This model, when overlaid on the data spiral could find the ridge of the spiral in the data, but with a crux - the precession of the annuli was opposite in sense to precession of stars! This insight steered us to revisit the orbits of individual stars and the evolution of their angular momenta along their orbits, which eventually led to the making of this chapter.

2.1 Introduction

Equilibrium models of the Milky Way (MW) have long been used as the interpretive base for increasingly large datasets of the MW stars. However, recent data from the *Gaia* mission (Gaia Collaboration et al., 2016, 2023) have revealed the dynamical disequilibrium of the MW disc in both the vertical (Antoja et al., 2018; Hunt et al., 2022; Alinder et al., 2023; Antoja et al., 2023) and radial (Antoja et al., 2022; Cao et al., 2024; Hunt et al., 2024) projections of six-dimensional phase space (e.g. in $z - v_z$, $R - v_r$ and $R - v_\phi$). The aforementioned projections are a non-exhaustive list of representations of disequilibrium patterns observed.

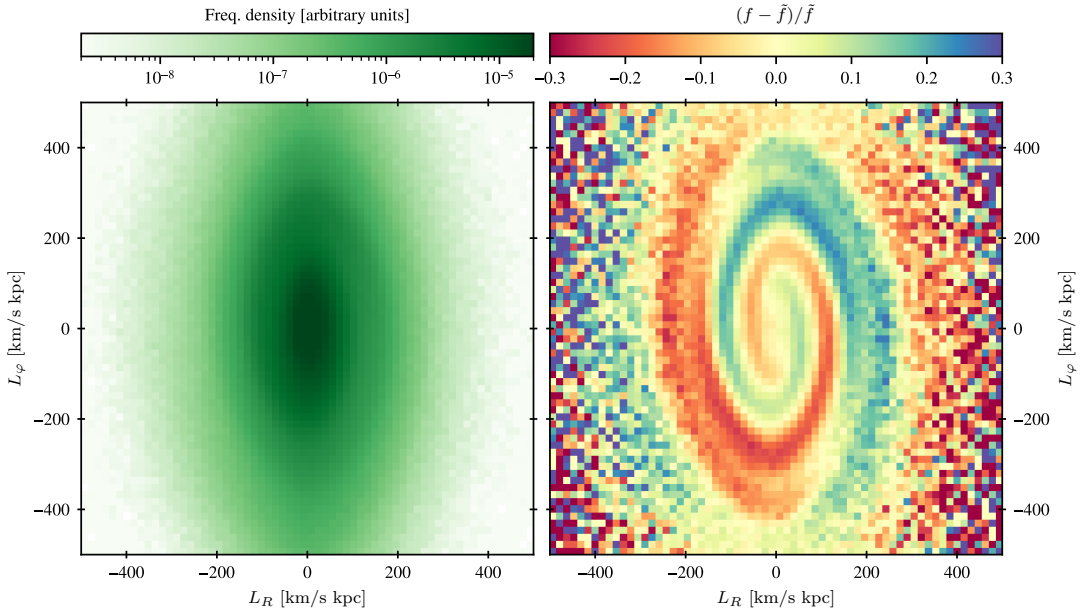

Figure 2.1: The *Gaia* AM spiral in cylindrical coordinates. The left panel show the raw data histogram, while the right panels show residuals against a symmetric model. A spiral-shaped over-/under-density is clearly visible, at around the 20% level.

Perhaps the most striking feature of the data is the spiral pattern observed in the vertical coordinates $z - v_z$. In this phase-space projection, the data show a spiral pattern owing to incomplete phase mixing in the Galactic disc. The presence of the feature provides us with a unique opportunity to study disequilibrium processes in real-time and is proving to be a valuable source of information about the Galactic potential, perturbative events and the dynamical evolution of the MW (Widmark et al., 2022a; Li & Widrow, 2021; Widmark et al., 2022b; Darragh-Ford et al., 2023; Guo et al., 2024).

The origin of the phase spiral has been linked to perturbations to the disc. However, there is no consensus on the nature of the perturbation. One hypothesis is that the passage of the Sgr dwarf galaxy through the disc plane seeds the perturbation, where the tidal forces generate vertical and radial oscillations in the disc (Binney & Schönrich, 2018; Laporte et al., 2019). Other proposed formation mechanisms include vertical oscillations triggered by bar buckling (Khoperskov et al., 2019), moving groups such as streams (Michtchenko et al., 2019) or other small-scale perturbations (Tremaine et al., 2023), and long-lived perturbations in the MW dark matter halo (Grand et al., 2023).

One space often not considered when looking at the kinematic signatures of disequilibrium in the MW disc is angular momentum (AM). In axisymmetric equilibrium disc models, the AM component perpendicular to the plane, L_z, is a conserved quantity. Meanwhile, for perfectly planar orbits, $L_x, L_y = 0$. However, the majority of disc stars exhibit some oscillation perpendicular to the plane; such stars trace oscillatory routes through $L_x - L_y$ space. When the epicycles of individual stars in the disc are not correlated, the resulting projection of $L_x - L_y$ is simply a 'blob' centred on zero. Why is it worth studying the distribution of MW stars in AM? There are several key advantages. First, choosing only two of the three components of AM already combines the full six-dimensional phase space information of the stars. This is advantageous when modelling the disequilibrium feature as it incorporates both radial and vertical terms. AM could incorporate features observed in projections of pairs of phase space coordinates. Also, AM can be measured directly from observational data without integrating orbits in an assumed potential, in contrast to other integrals such as the actions. Finally, as we shall see in Section 2.4, the trajectories of individual stars in AM (particularly in cylindrical coordinates) take simple forms, allowing straightforward modelling of kinematic signatures such as the spiral.

In this paper we present a novel outlook on the phase space spiral observed in the *Gaia* data through the AM lens. In Section 2.3 we show the cylindrical AM spiral in the *Gaia* data in the local volume. Section 2.4 lays the framework for interpreting the spiral, through consideration of the orbits of individual stars, then presents the spiral model used in the remainder of the work. The results of our modelling is discussed in Section 2.5, where we address the insights gained through modelling in this space, and the limitations. Finally, we provide some concluding remarks in Section 2.6.

2.2 The Gaia RVS sample

To build the parent sample, we query the *Gaia* DR3 (Gaia Collaboration et al., 2023) catalogue, accepting stars that have radial velocity measurements, a reduced weighted unit error of `ruwe`<1.4 and a relative parallax precision of $\varpi/\sigma_\varpi > 5$. Appendix A.1 gives our ADQL query. To transform the ICRS coordinates of the *Gaia* stars to the Cartesian Galactocentric frame, we adopt a right-handed coordinate system with the Sun positioned at $\vec{r}_{\odot\rightarrow MW} = (-8.3, 0.0, 0.02)$ kpc (GRAVITY Collaboration et al., 2021; Bennett & Bovy,

2018b), with velocity $\vec{v}_{\odot\to MW} = (11.1, 244.24, 7.24)$ km s^{-1} (Schönrich et al., 2010a; Eilers et al., 2019a). Finally, the angular momenta of stars, used in subsequent sections, are computed using the positions and velocities of stars in the Galactocentric frame. The total number of stars returned from the query is 26,747,826 stars. In this work, we use only stars confined to the annular sector defined by the radial condition of $|R - 8.3 \text{ kpc}| < 1.0$ kpc and azimuthal condition of $|\varphi - \pi| < 1.0/8.3$ where (R, φ) are the cylindrical galactocentric coordinates. The total number of stars after applying the cut is 11,827,676 stars, this is the main sample of stars used in all subsequent figures. Stars within this region have a mean AM uncertainty in each Cartesian direction of ≈ 30 km s^{-1}kpc.[1]

2.3 The angular momentum spiral

Figure 2.1 exhibits the main result of this Article: the clear spiral structure visible in the distribution of *Gaia* stars in AM space. In the figure we display the cylindrical coordinate system L_R, L_φ where the quantities are given (in terms of cylindrical velocities v_R, v_φ, v_z) by

$$\begin{aligned} L_R &\equiv -z v_\varphi; \\ L_\varphi &\equiv z v_R - R v_z. \end{aligned} \tag{2.1}$$

A full derivation of the cylindrical AM can is provided in Appendix A.3. The left panel shows the raw histogram of stars in our sample. Even before any processing of the images, there is a clear spiral structure visible.

In the right panel, we pick out this spiral signal using a basic yet effective procedure: we construct a 'symmetrised' histogram $\tilde{f}$ by taking the average of the original histogram f and its 180-degree rotation. The right panel then shows the fractional residuals of the original histogram versus this symmetrised histogram, i.e., $f/\tilde{f} - 1$. This procedure is designed to extract any odd-parity signal in the histogram, but is not perfect: there might well be even-parity structure that is washed away, and it is highly sensitive to the position of the zero point (in other words, sensitive to the choice of mid-plane). These caveats notwithstanding, the method appears to successfully extract the spiral structure

[1]Computed via Monte Carlo error propagation of the uncertainties on distance, proper motion and radial velocity as reported from the *Gaia* table. Note that proper motion correlations were accounted for during the propagation.

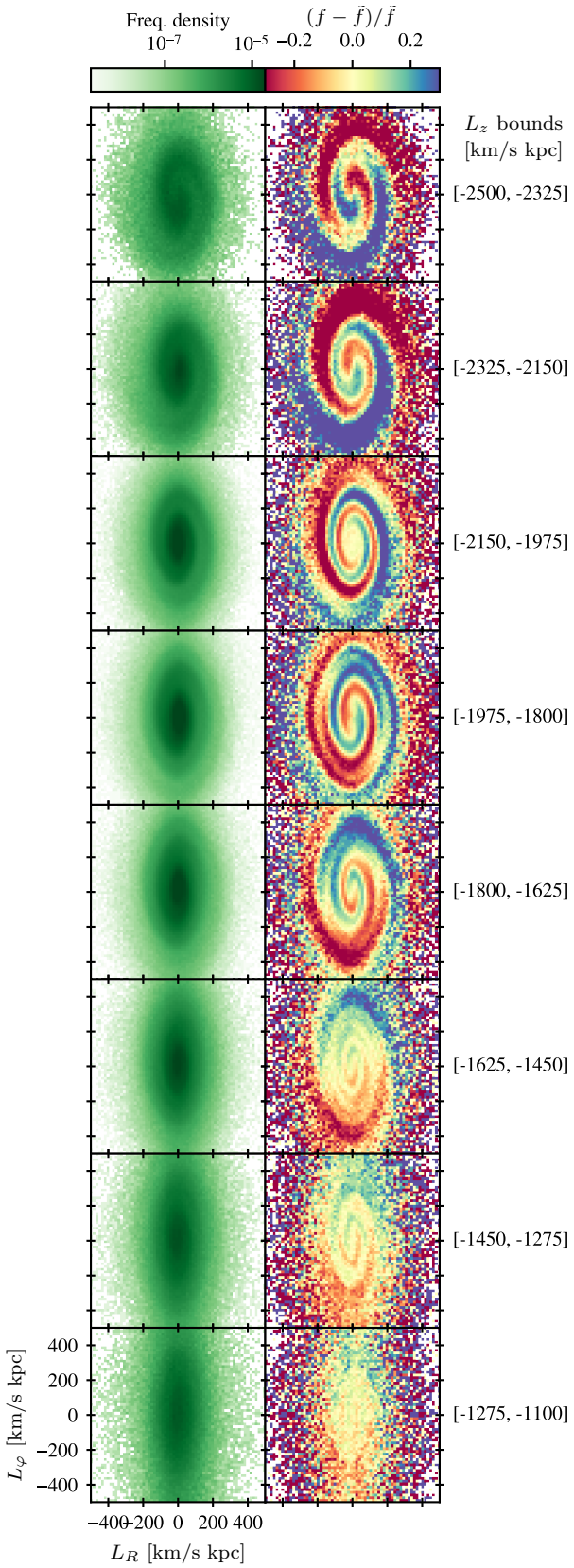

Figure 2.2: The $L_R - L_\varphi$ spiral split across L_z bins, as labelled. *Left:* raw histograms. *Right:* fractional residuals against symmetrised distributions. The phase, winding, and prominence of the spiral change appreciably with L_z.

from the stellar distribution: the residuals clearly show spiral-shaped over/under-densities at around a $\sim 20\%$ level.

We also show, through simple arguments, that the AM spiral shown in Figure 2.1 relates to the $z - v_z$ spiral through simplifying assumptions about the local volume. To show the mapping of the $z - v_z$ spiral to $L_x - L_y$, starting from the definitions of AM $\vec{L} = \vec{r} \times \vec{v}$, considering only L_x, L_y and solving for z, v_z the following relations between AM and phase space coordinates are found

$$\begin{aligned} z &= \frac{-xL_x - yL_y}{L_z}; \\ v_z &= \frac{-v_x L_x - v_y L_y}{L_z}. \end{aligned} \tag{2.2}$$

We can further simplify the relations by assuming that, locally, $v_y \gg v_x$, and $x \gg y$ and $L_z \approx x v_y$. Substitution of these relations into Equations 2.2 yields the local mapping between the phase space spiral and the AM spiral

$$\begin{aligned} z_{\text{local}} &\approx -\frac{L_x}{v_y}; \\ v_{\text{z,local}} &\approx -\frac{L_y}{x}. \end{aligned} \tag{2.3}$$

The resulting relations for $L_x - L_y$ map to $L_R - L_\varphi$ through $L_x \approx -L_R$ and $L_y \approx -L_\varphi$.[2]

From these considerations, it is clear that *locally* a spiral in $L_R - L_\varphi$ will map to a $z - vz$ spiral. However, this mapping is evident only when making an assumption about the motions in the local volume. Furthermore, this approximation can be applied at various locations on the disc and is valid only if coordinate axes are rotated such that the new frame of reference has its x-axis aligned with the galactic centre.

Figure 2.2 shows the $L_R - L_\varphi$ spiral after segregating our stellar sample into a series of bins in vertical AM L_z. The spiral structure is discernible in all but the last L_z bin, albeit with differing morphologies. Progressing from largest (most negative) to the smallest (least negative) L_z, the phase of the spiral changes and its winding tightens.

Whether the disappearance of the spiral in the final L_z bin is real or instead

[2]The definition of the coordinate system implies that at the solar location all stars have $x \approx -R$, $y \approx 0$.

due to the paucity or imprecision of the data is unclear. Some asymmetry is discernible in the residuals, but this can be made to disappear by changing the assumed position of the galactic mid-plane.

2.4 Interpreting the spiral

In this section, we try to arrive at a dynamical interpretation of the AM spiral described in the previous section. First, in Sec. 2.4.1, we consider the path of a typical disc star through AM space, and thus show how differential rotation in this space gives rise to the spiral. Then, in Sec 2.4.2 we illustrate how a stars path in AM changes when moving away from the assumption of nearly circular orbits. Finnaly, in Sec. 2.4.3, we write down a generative model that can give a good first approximation to the observed spiral.

2.4.1 A star's path through angular momentum space

To understand the source of the observed spiral in AM space, we must first understand how typical disc stars on nearly circular orbits move in this space. Taking a single such star with vertical AM L_z, we can write down its trajectory in the meridional plane as

$$\begin{aligned} R &= R_g\,(1 + \epsilon \sin(\Omega_R t))\,; \\ z &= z_0 \sin(\Omega_z t), \end{aligned} \tag{2.4}$$

where R_g is the guiding-centre radius of the star, z_0 is the amplitude of the star's vertical (i.e., perpendicular to the plane) oscillation, ϵ is the eccentricity of the in-plane orbit, and Ω_z, Ω_R are the respective frequencies of the vertical and radial oscillations. We have assumed that both oscillations have zero initial phase. Including non-zero phases in the sinusoids would lead to no qualitative change in our subsequent results, only phase shifts. These expressions also assume a harmonic and separable potential, but as we shall see, they give a good approximation to the motion in a more realistic potential.

The guiding-centre radius R_g is a function of L_z alone, given implicitly by $L_z = -v_{\rm circ}(R_g)R_g$, where $v_{\rm circ}(R_g)$ is the MW circular velocity curve evaluated at $R = R_g$. The negative sign here corresponds to a clockwise (left-handed) rotation

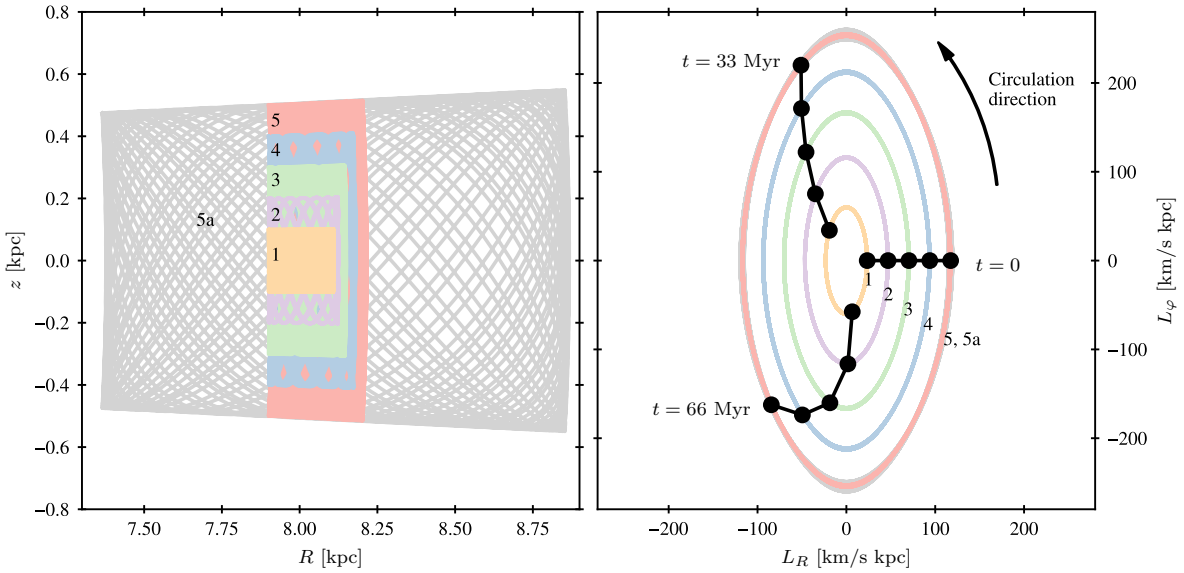

Figure 2.3: Disc orbits in AM space. *Left:* the trajectories in the meridional plane of 6 stars, labelled '1', '2', '3', '4', '5' (various colours), and '5a' (grey). All stars have the same vertical AM L_z but differ in their vertical energies with the exception of '5a', which has the same vertical energy as '5', but with a much larger radial oscillation. *Right:* the corresponding $L_R - L_\varphi$ trajectories of the same stars (coloured ellipses). Also shown in this panel are isochrones at $t = 0$, 33 Myr, 66 Myr (black, spotted lines). The differential circulation of stars in this space gives rise to the observed spiral structure.

around the Galactic centre. Meanwhile, the vertical frequency Ω_z is a function of the vertical amplitude z_0: $\Omega_z \approx 2\pi/P(z)$, with $P(z)$ the vertical periodgiven by

$$P = 4\int_0^{z_0} \frac{dz}{\sqrt{2[\Phi(R_g, z_0) - \Phi(R_g, z)]}}. \tag{2.5}$$

In other words, stars with large vertical amplitudes have slower vertical frequencies in a typical Galactic potential. The vertical period is derived from energy conservation in the vertical direction. For a star oscillating between $z = 0$ and $z = z_0$, the energy is $E_z = \Phi(R_g, z_0)$. Separating variables in $\dot{z}^2 = 2[\Phi(R_g, z_0) - \Phi(R_g, z)]$ and integrating over one quarter-period (from $z = 0$ to z_0) yields the expression above (Binney & Tremaine, 2008). The full period is four times this integral by symmetry.

Derivatives of Equation (2.4) along with the fact that $L_z = Rv_\varphi$, lead to expressions for the star's velocities in cylindrical coordinates,

$$\begin{aligned} v_R &= \epsilon R_g \Omega_R \cos(\Omega_R t); \\ v_z &= z_0 \Omega_z \cos(\Omega_z t); \\ v_\varphi &= -\frac{R_g \Omega_\varphi}{1 + \epsilon \sin(\Omega_R t)}. \end{aligned} \tag{2.6}$$

Here, Ω_φ is the angular frequency of the MW rotation *at the guiding-centre radius*, i.e., $\Omega_\varphi \equiv v_{\rm circ}(R_g)/R_g$.

Finally, Eqs. 2.4 and 2.6 can be combined to give expressions for the cylindrical angular momenta,

$$\begin{aligned} L_R &\equiv -zv_\varphi \\ &= \frac{\Omega_\varphi}{\Omega_z} \frac{1}{1 + \epsilon \mathrm{s}_R(t)} L_0 \mathrm{s}_z(t); \\ L_\varphi &\equiv zv_R - Rv_z \\ &= -L_0 \mathrm{c}_z(t) + \epsilon \left(\frac{\Omega_R}{\Omega_z} \mathrm{s}_z(t)\mathrm{c}_R(t) - \mathrm{c}_z(t)\mathrm{s}_R(t) \right), \end{aligned} \tag{2.7}$$

where we have abbreviated $\mathrm{s}_X(t) \equiv \sin(\Omega_X t)$, $\mathrm{c}_X(t) \equiv \cos(\Omega_X t)$, and $L_0 \equiv R_g z_0 \Omega_z$. For stars on nearly circular orbits, such that $\epsilon \ll 1$,

$$\begin{aligned} L_R &\approx \frac{\Omega_\varphi}{\Omega_z} L_0 \sin(\Omega_z t); \\ L_\varphi &\approx -L_0 \cos(\Omega_z t). \end{aligned} \tag{2.8}$$

Thus, in the space of L_R and L_φ, a star on a nearly circular orbit circulates in an elliptical shape with frequency Ω_z. The semi-major axis of the ellipse is L_0 and the major/minor axis ratio is Ω_z/Ω_φ.[3] Empirically, Ω_z decreases with z_0 more slowly than linear, so that L_0 increases with z_0. In other words, stars with larger vertical oscillations trace out larger ellipses and they do so with lower frequencies. This differential rotation is the process that gives rise to the observed spiral.

These various processes are depicted in Figure 2.3. The left-hand panel of the figure shows the trajectories in the meridional plane of 6 stars, labelled '1', '2', '3', '4', '5', and '5a'. All stars have the same vertical AM L_z, corresponding to a guiding centre radius $R_g = 8$ kpc. However, the stars differ in their vertical energies: star '1' has the smallest vertical energy (smallest oscillation amplitude perpendicular to the plane), while star '5' has the largest. Star '5a' has the same vertical energy as star '5', but with a larger amplitude radial oscillation. The orbits were integrated using the `gala` python package (Price-Whelan, 2017) using the `MilkyWayPotential2022` potential.

The right-hand panel of Fig. 2.3 shows the corresponding trajectories in $L_R - L_\varphi$. The stars trace out clear ellipses in this space, as predicted by Eq. 2.8, with the ellipse radius increasing monotonically with vertical energy. Comparing stars '5' and '5a', the vastly differing radial oscillation amplitudes leave little imprint in this space: the ellipse corresponding to '5a' is somewhat blurred compared to that of '5' at the vertical extremes (i.e., when $L_R = 0$ and $|L_\varphi|$ is maximal). Thus, even stars with non-negligible eccentricities give approximately elliptical traces in $L_R - L_\varphi$.

In this calculation, all stars start at their vertical maxima; this corresponds to the black spotted line labelled '$t = 0$' in the right-hand panel of Fig. 2.3. The lines labelled '$t = 33$ Myr' and '$t = 66$ Myr' can be understood as later isochrones: they indicate the positions of the stars at later instants of time, as labelled (note that star '5a' is not included in this spotted line, for visual clarity). As time goes on, the isochrones grow increasingly curved because the stars with larger vertical energies oscillate more slowly. This illustrates the principle outlined above: the differential circulation in L_R, L_φ gives rise to the observed spiral.

[3] It is nearly always the case that $\Omega_z > \Omega_\varphi$. However, this can be reversed for stars with sufficiently large vertical amplitudes. In such cases, L_0 is instead the *semi-minor* axis of the ellipse, and the major/minor axis ratio is Ω_φ/Ω_z.

2.4.2 Radial orbits in angular momentum

To follow up on the previous subsection, it is important to consider how the evolution of stars precedes in the case where the orbits are more eccentric. We show how increasingly eccentric orbits deviate from their elliptical paths in AM, testing the assumption of nearly circular orbits made in Section 2.4.3. To illustrate the variation in $L_R - L_\varphi$ space, we conduct simple orbit integration in gala in the `MilkyWayPotential` model. Five stars are initialised with $\vec{x} = [-7.9, 0.0, 0.5]$ kpc and $\vec{v} = [v_x, v_y, 0.0]$. To assign the velocities, the first star has no radial motion (i.e. $\vec{v} = [0.0, v_c(R = 7.9), 0.0]$) and each successive star takes a fraction of the y velocity such that the magnitude is the same for all stars. The fraction of the v_y that is assigned to v_x are $(0.05, 0.1, 0.2, 0.3, 0.5)$. Resulting in eccentricities of $\epsilon = (0.01, 0.23, 0.33, 0.41, 0.48)$. Figure 2.4 shows the projections of the orbits in the meridional plane and face-on, along with the resulting AM paths the stars follow, with the dashed line showing the ellipse defined by our model in equation 2.8. The Figure illustrates how stars with increasingly radial orbits deviate from the elliptical path in AM. For moderate eccentricities $\epsilon = (0.01, 0.23)$ the modelled ellipse remains in good agreement with the orbit integrated lines, and within observational uncertainties. However, for greater eccentricities, the ellipse defined by the model overestimates the values of L_R, L_φ. However, these simple orbit integrations show that even for very eccentric orbits the stars still trace out ellipses. It also provides also a good indication as to why the spiral persists long after perturbation. As stars mix radially (and vertically), eccentric orbits still follow almost elliptical paths. Thus, allowing a spiral in AM to persist even under radial mixing.

2.4.3 A generative model for the spiral

In this section we describe a simple model for the AM spiral. Rather than L_R, L_φ, modelling is easier in the space L_R, L'_φ, where $L'_\varphi \equiv (\Omega_\varphi/\Omega_z)L'_\varphi$. In this space, stellar orbits trace out circles rather than ellipses, so prior to the perturbation we can assume a rotationally symmetric equilibrium distribution. We assume a 2D Gaussian with standard deviation σ_L.

In this simplistic first treatment, we assume the perturbation has acted to rigidly tilt the Galactic disc midplane by an angle $\theta_{\rm tilt}$ about a line-of-nodes at azimuth $\varphi_{\rm tilt}$. Thus, at azimuth φ and radius R, the height of the Galactic midplane (with

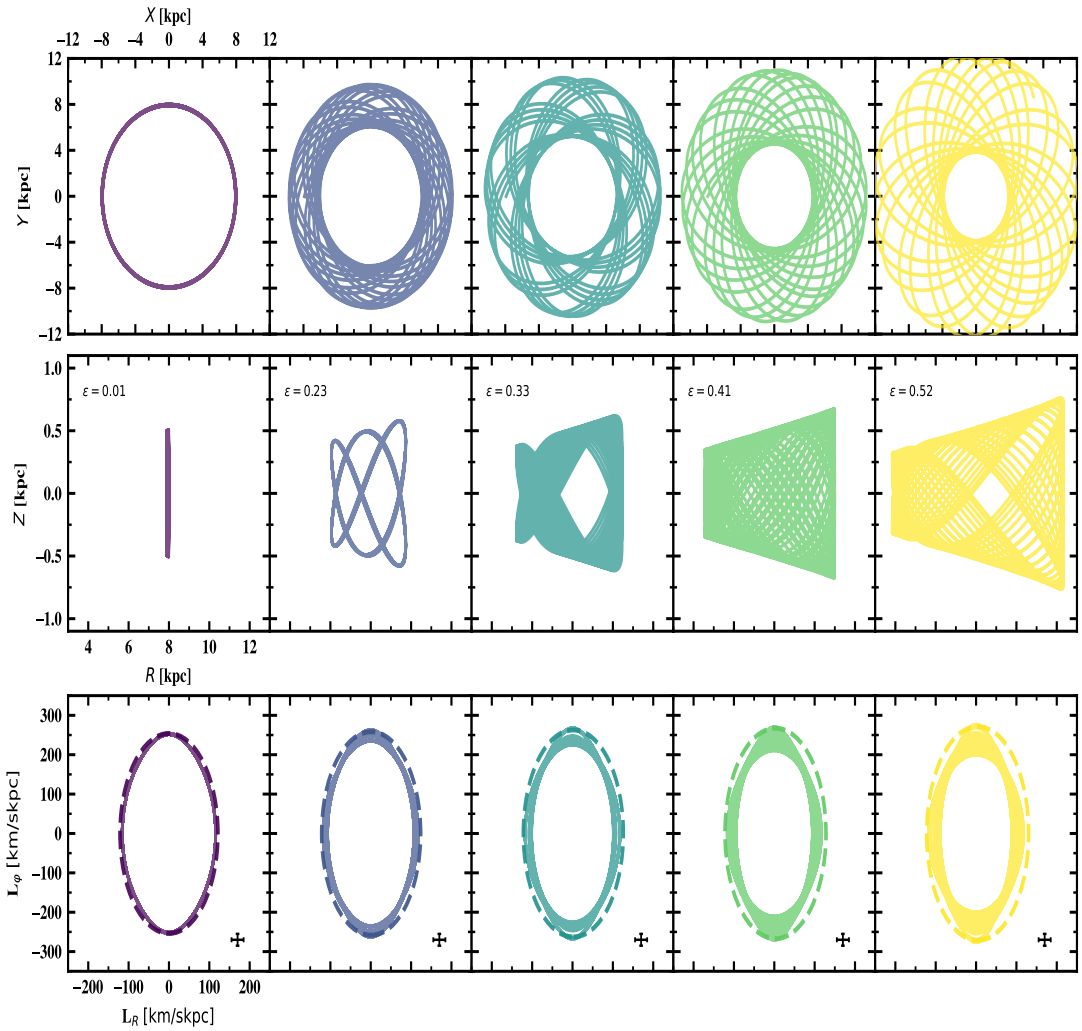

Figure 2.4: The $x - y$, $R - z$ and $L_R - L_\varphi$ tracks of five stars. Each column moving from left to right shows stars with increasing eccentricity in spatial and AM projections. In the bottom row, the solid lines show the angular momentum track while the dashed line show the approximation of the track using Equation 2.8. The orbits were integrated using Gala in the `MilkyWayPotential`, from which the vertical and azimuthal frequencies were calculated using Equations2.5 and $\Omega_\varphi \equiv v_{\rm circ}(R_g)/R_g$. In the bottom left of the $L_R - L_\varphi$ panels, the typical size of the observational uncertainties in AM are shown as error bars.

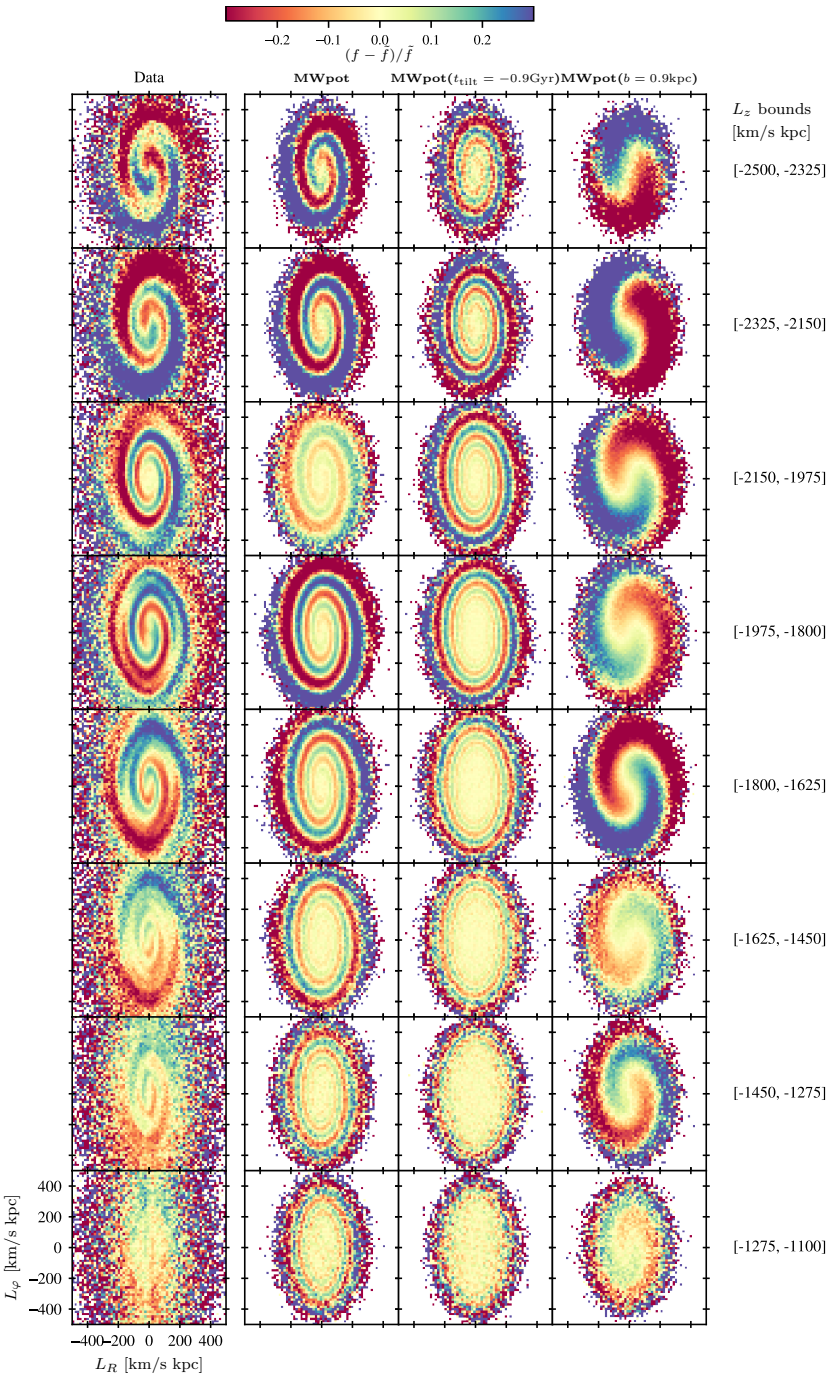

Figure 2.5: The AM residuals in $L_R - L_\varphi$ binned in L_z. *First column:* The *Gaia* data. *Second column:* A realisation of the MWpot model defined in 2.4.3, sampled at the location of the data. *Third column:* A realisation of the MWpot model with $t_{\rm tilt} = -0.9$ Gyr, the larger time shows a more wound spiral in all bins in comparison to the first model with $t_{\rm tilt} = -0.45$ Gyr. *Fourth column:* A realisation of the MWpot model with the same timing as the first column, but with the scale height of the disc increased to $b = 0.9$kpc, this model with a larger scale height shows a much less wound spiral.

respect to the unperturbed height) is

$$\bar{z}(R,\varphi) = R\sin(\theta_{\rm tilt})\left[\cos(\varphi_{\rm tilt})\sin(\varphi) - \sin(\varphi_{\rm tilt})\cos(\varphi)\right] \ . \tag{2.9}$$

Assuming all stars are on circular orbits at $R = R_g$ (with R_g itself a function of L_z), the change in L_R for a given star is $\delta L_R = -\bar{z}v_\varphi$ and there is no change in L_φ. We further assume that this perturbation applies instantaneously at time $t_{\rm tilt}$. We take $t = 0$ for the present day, so that $t_{\rm tilt}$ is negative.

Our model thus has a parameter set θ comprising 4 free parameters: $\theta = \{\sigma_L, \theta_{\rm tilt}, \varphi_{\rm tilt}, t_{\rm tilt}\}$. For an individual star with observed L_z, φ, the likelihood of its observed L_R^0, $L_\varphi'^0$ (the 0 superscripts here indicating the observed values at the present day) is

$$\begin{aligned}\ln l(\theta) &\equiv \ln p(L_R^0, L_\varphi'^0 | L_z, \varphi, \theta) \\ &= -\frac{1}{2\sigma_L^2}\left((L_R^{t_{\rm tilt}} - \mu_L)^2 + L_\varphi'^{t_{\rm tilt}\,2}\right) - \ln(2\pi\sigma_L^2),\end{aligned} \tag{2.10}$$

where

$$\begin{aligned}L_R^0 &= L_R^{t_{\rm tilt}}\cos(\Omega_z t_{\rm tilt}) + L_\varphi'^{t_{\rm tilt}}\sin(\Omega_z t_{\rm tilt}); \\ L_\varphi'^0 &= -L_R^{t_{\rm tilt}}\sin(\Omega_z t_{\rm tilt}) + L_\varphi'^{t_{\rm tilt}}\cos(\Omega_z t_{\rm tilt}),\end{aligned} \tag{2.11}$$

and

$$\mu_L = \bar{z} R_g \Omega_\varphi. \tag{2.12}$$

In other words, the present-day distribution of angular momenta is given by a (differential) rotation (Eq. 2.11) of the initial distribution, assumed Gaussian. The rotation is differential because Ω_z is itself a function of $L_R^2 + L_\varphi'^2$.

In this work, we do not perform a detailed optimisation of this likelihood function in order to fit the observed data. Instead, we simply endeavour to explore how the model responds to its various input parameters by generating a series of model realisations. In each case, we generate a population of stars with L_z and φ values matching those of the *Gaia* stars in our observed sample, but with L_R and L_φ randomly drawn from the likelihood function. In order to generate realisations of the models, we first set the model parameters θ and choose a MW potential. Given the observed values of L_z, φ for each star, we compute R_g and Ω_φ. Using

these quantities, we can calculate the initial L_R displacement for each star, μ_L. Given μ_L and σ_L (the latter being an input model parameter), we can generate sample values for $L'^{t_{\rm tilt}}_{\varphi}$ and $L^{t_{\rm tilt}}_{R}$ from the initial Gaussian distribution. Each generated 'star' can then be associated with a vertical frequency Ω_z, which for a given potential varies monotonically with $(L'^{t_{\rm tilt}}_{\varphi})^2 + (L^{t_{\rm tilt}}_{R})^2$. This Ω_z is then used to evolve each star to the present day via Equation 2.11.

Figure 2.5 shows three example realisations of the model. We have taken the L_z and φ values of the observed stars from the data and for any given star, we compute the values of Ω_z, Ω_φ using the *Gala* (Price-Whelan, 2017) package for a given potential. To illustrate the effect of the parameters of the chosen potential from which the frequencies are computed, we compute the model in two potentials. The first being the `MilkyWayPotential` (MWpot in the Figure), which is a 4-component potential model comprised of a nucleus (Hernquist sphere with $M_{\rm nucl} = 1.71\times10^9 M_\odot$, $c = 0.07$kpc), a bulge (Hernquist sphere with $M_{\rm bulge} = 5\times10^9 M_\odot$, $c = 1.0$kpc), disc (Miyamoto-Nagai with with $M_{\rm disc} = 6.8\times10^{10} M_\odot$, $a = 3.0$kpc and $b = 0.28$kpc) and a halo (NFW with $M_{\rm halo} = 5.4\times10^{11} M_\odot$, $r_s = 15.62$kpc). The second potential is identical to the first with the exception of the scale height of the disc being increased to $b = 0.9$ kpc.

For the aforementioned examples, we adopt a model parameter set with $t_{\rm tilt} = -0.45$, $\varphi_{\rm tilt} = -\pi/4$, $\theta_{\rm tilt} = \tan^{-1}(9/800)$ (giving a maximal tilt of 90 pc at $R = 8$ kpc), $\sigma_L = 80\,{\rm km\,s^{-1}kpc}$. We also show in Figure 2.5 a model realisation with the first potential, but with a changed value of $t_{\rm tilt}$ from -0.45 Gyr to -0.9 Gyr.

The figure shows the distribution of sampled angular momenta, segregated into the same L_z bins as in Fig. 2.2. By eye, the MWpot model (second column in Figure 2.5 appears to give a good match to the observed spiral, with the spiral morphology approximately correct in most L_z bins. It is worth emphasising that this is simply an approximate, 'chi-by-eye' fit, and not the result of a more rigorous optimisation, which we reserve for future work. As such, the parameter choice should not be over-interpreted.

In the third column of Figure 2.5, we show the AM distribution when changing $t_{\rm tilt}$. A 450 Myr difference in the timing shows a spiral with many more wraps than the when $t_{\rm tilt} = -0.45$ Gyr. In many lower L_z bins, the spiral feature at the centre is not resolvable, and in the smallest L_z bin, the spiral feature disappears almost completely.

Furthermore, when varying the scale height of the disc in the second potential

(fourth column in Figure 2.5, the resulting spiral (with the same set of perturbation parameters as the second column) shows a very different morphology. The spiral has many fewer wraps compared with the fiducial potential. In the largest L_z bins ($L_z < -2150\mathrm{km\,s^{-1}kpc}$) the spiral feature has not yet formed. When the scale height of the disc is large, vertical frequency varies slowly with vertical energy, and so the gradient of the differential rotation is shallow and the spiral is slow to form. This is one example of the effect of the choice of MW potential on the morphology of the spiral.

2.5 Discussion

2.5.1 The global tilt model

Our model presented in Section 2.4.3 describes the creation and time evolution of a spiral in AM resulting from a bulk tilting of the disc. While Figure 2.5 is a simple by-eye fit to the observed data (See Figure 2.2), it remarkably produces many of the salient features we observe in the data in most L_z bins. In the second column of Fig. 2.5 the density along the spiral varies smoothly, and does not show any gaps in the relative density along the spiral, or asymmetric features. In the data however, in the bins with $L_z > -1975\mathrm{km\,s^{-1}kpc}$, the outer wraps in the region of $L_\varphi < 0$ are much more under dense than the model predicts. Furthermore, the model predicts that the spiral becomes more wound with decreasing (less negative) L_z, this is also observed in the data up to $L_z = -1625\mathrm{km\,s^{-1}kpc}$.

An additional factor to consider when comparing the model to the data is the effect of the choice of zero point (the height of the galactic mid-plane) on the AM density we recover in the data. Small adjustments to the zero point (of order < 100pc) can modify the asymmetry in the AM density, leading to a closer match to the model in some L_z bins, and a worse match in others. This suggests that a single mid-plane height at any given L_z (or guiding radius) is too simplistic to describe the data.

The parameters of the MilkyWayPotential model spiral, which we stress should are only by-eye estimates, place the time of the tilting of the disc at $t_{\mathrm{tilt}} = -0.4$ Gyr, which is consistent with studies (Antoja et al., 2018; Laporte et al., 2019; Li & Widrow, 2021; Widmark et al., 2022a; Frankel et al., 2023; Frankel et al., 2024) for the time of spiral formation. When matching the model to the

data, we find also that using a time of $t_{\rm tilt} \simeq 1$ Gyr produces a spiral that is too wound in every L_z bin.

Not only do the perturbation parameters affect the morphology of the spiral, but also the choice of MW potential parameters. This is illustrated clearly in Figure 2.5, where increasing the scale height of the disc, while keeping the likelihood parameters fixed produces a spiral that is much less wound. The particular choice of potential affects the constraints that can be placed on $t_{\rm tilt}$ through our modelling. In this potential, the significantly increased vertical scale height of the disc leads to the slower winding of the spiral, due to the slower change in vertical frequency with vertical energy (see Equation 2.5). A less-wound spiral can also be produced by choosing a smaller $t_{\rm tilt}$, demonstrating that the scale height and time since perturbation are likely strongly covariant.

The remaining model parameters also affect the spiral produced by the model. For $\theta_{\rm tilt}$, adopting larger values (e.g. $\theta_{\rm tilt} > 2°$) results in an increased relative density in regions that are over-dense, and a decrease in regions that are under-dense. This causes a spiral that appears much 'sharper', with few regions of relative density close to zero. The parameter σ_L controls the spread in relative density of the space. A larger value leads to a blurring between the over/under-dense regions in AM. Finally, $\varphi_{\rm tilt}$ is tied to the spatial evolution of the spiral and whether, in a given L_z bin a spiral will be observed at the solar location.

2.5.2 The timing, time evolution, and different perturbation scenarios

In Figure 2.5, we show the present-day snapshot ($t = 0$) of AM spiral. However, this figure does not fully encapsulate the temporal or spatial evolution of the spiral in AM space. We explore these ideas in this section.

As a function of time, the spiral winds up due to the differential oscillation of stars in AM space. This winding effect can be seen in Figure 2.5: the spiral with the earlier perturbation time (third column) is more tightly wound than the spiral with the later perturbation time (second column). In a given L_z bin, the rate of this winding depends, to first order, on the vertical steepness of the MW potential at the guiding-centre radius corresponding to that L_z.

Under this model with a global tilt perturbation, the spiral also shows spatial

evolution, due to the spatial variation in the initial perturbation. Stars that were spatially situated along the line-of-nodes at the time of the perturbation did not experience a significant perturbation, while stars at azimuths perpendicular to the line-of-nodes did. At subsequent times, this spatial variation in perturbation amplitude translates to a spatial variation in spiral amplitude. However, because of the (differential) rotation of the Galactic disc, the locus of points with the largest (smallest) spiral amplitudes changes from a line perpendicular (parallel) to the line-of-nodes into a *spatial* spiral in x, y. For an observer at a given position, this manifests as a sinusoidal variation in phase spiral amplitude as a function of L_z, because stars falling in different L_z bins have different guiding centre radii, and were thus (on average) at different azimuths at the time of the perturbation. This effect is also seen in our alternative model in which the perturbation is modelled as a more localised velocity kick (Appendix A.2).

Studies on the tilting of the galactic disc due to previous mergers (e.g. Gaia Sausage/Enceladus) have shown that the degree of tilting depends on a multitude of parameters including the mass of the satellite, the initial inclination w.r.t to the disc at infall, the circularity and whether the merger is prograde and retrograde. For mergers with massive satellites (with $M_{\rm sat} = 10^{11} M_{\odot}$), the tilting rate of the disc can be as high as $\sim 8°$/Gyr but is drastically smaller for satellites with mass of $M_{\rm sat} = 10^{10.5} M_{\odot}$, where the tilting rate decreases to $< 2°$/Gyr (Dodge et al., 2022). Our modelling of the spiral suggests that only small $\theta_{\rm tilt} < 2°$[4] tilts are needed to produce and AM spiral with similar amplitude to the data. Additionally, the timing of the spiral found point to a relatively recent merger, where evidence suggests that the Sgr dwarf may be the main perturber that seeded the AM spiral we observe (Antoja et al., 2018; Laporte et al., 2019; Hunt et al., 2021). Our model parameters agree more with a light satellite passage than a massive merger scenario. Although we note that our timing results are also dependent on the choice of potential, and ideally both the timing and potential would be fit simultaneously.

Hunt et al. (2022) detected multiple arms in the $z - v_z$ phase spiral and suggest multiple perturbations form the multiple arms detected. In their Figure 2, the two-armed spiral is detected in the region of $R_g < 7$kpc, assuming a flat rotation curve, this corresponds to a $L_z >= -1500 \mathrm{km\,s^{-1}kpc}$. In our Figure 2.2 we do not observe multiple arms in AM. However, It is important to note here that our method of background removal, $(f - \tilde{f})/\tilde{f}$, would erase two-armed spiral features.

[4]For our MWpot model, the tilting is instantaneous with a tilt angle of $\theta_{\rm tilt} \simeq 1.2°$.

Nevertheless, two armed spirals could be generated in AM through the application of multiple perturbations.

In Figure 2.5, the variation of the relative density along the spirals generated by the model vary smoothly along the ridge of spiral. The data however (in the first column) show features such as fracturing in the arms, most strikingly in the range $-1975 < L_z < -1625$ kms^{-1}kpc. In the framework of our AM model, one could generate fractures in the spiral arms by having a subset of the stars in the sample have systematically more radial orbits, such that their elliptical paths in AM are systematically offset from stars on more circular orbits (the difference in AM path for circular and more radial orbits is illustrated in Figure 2.4).

2.5.3 Limitations of the model

There are limitations to the model we present in this work. Mainly they are (i) the model requires the assumption of the MW potential, choices of the parameters here will affect predictions made in AM. This limitation may also be advantageous, as the MW potential parameters could be fit to the data. (ii) The assumption of a global tilt is likely too simple, as both simulations (e.g. Huang & Carlberg, 1997; Dodge et al., 2022) and data on the MW warp (e.g. Jónsson & McMillan, 2024) find that discs in galaxies respond to infalling satellites through bending modes (Earp et al., 2017). A more sophisticated tilt perturbation model would include a spatially varying warp. (iii) The model assumes that the perturbation has no self gravity,[5] and the vertical frequencies are computed before the onset of perturbation to the disc.

Additionally, an implicit assumption of our model is that the vertical energy of stars is conserved along their orbits, which requires a separable and static potential. This assumption simplifies the dynamics as the vertical frequencies before and after perturbation remain the same, and a time-varying potential is not required. This assumption does not generally hold in more realistic galactic discs. For instance, Solway et al. (2012) demonstrated that vertical energy is not conserved during disc evolution, even under relatively weak perturbations such as spiral arms. A more robust quantity like the vertical action is conserved in low-perturbation regimes, as found by Vera-Ciro & D'Onghia (2016). In contrast, stronger perturbations, such as those induced by the Galactic bar, degrade both

[5] A common assumption; but see discussions regarding self gravity in e.g. Darling & Widrow (2019); Banik et al. (2022).

vertical energy and action conservation due to significant vertical heating.

However, since we assume that the spiral perturbation occurred relatively recently (within the last < 1 Gyr) and we consider a volume of the disc outside the bar region, this assumption remains reasonable.

2.6 Conclusion

In this paper, we have presented a novel view of the phase spiral in AM space. We show in Section 2.3 the AM spiral observed in *Gaia* data in the solar neighbourhood in cylindrical coordinates. We show also that the AM spiral relates to directly to the $z - v_z$ spiral when making assumptions about the local volume, and that a spiral in AM can map to $z - v_z$. In Section 2.4.1 we describe fully the path of stars in AM, relating the path in cylindrical AM to the vertical and azimuthal orbital frequencies of stars. In Section 2.4.3 we present a simple model of the spiral in AM through modelling orbits in this space where the perturbation is due to a bulk tilting of the disc. Also in Section 2.4.3 we demonstrate the ability of the model to recover the general shape, winding and amplitude of the observed spiral in the data across multiple L_z bins, and the affect of timing and potential on the predicted spiral. In Appendix A.2, we present an additional model of a kick-based perturbation in the framework of the orbit-based model presented in Section 2.4.3, to show the effect of perturbation choice. The main conclusions are:

1. AM is a novel space in which the phase space spiral can be clearly observed. There are two main advantages of this space over $z - v_z$. Firstly, the radial and vertical oscillations are coupled (all six dimensions of phase space are considered). Secondly, under reasonable assumptions, a simple analytic model, based on the path of a star in AM along it's orbit, produces an AM spiral that is able to reproduce the winding and amplitude of the AM spiral in the data. The model also paves the way for a likelihood-based fitting of the AM spiral.

2. By representing the path of a star through AM, we find that the mechanism of spiral formation is due to the differential rotation of stars in AM space.

3. Through our modelling approach, we find that the AM spiral predicted by modelling a tilt perturbation can reproduce the winding and amplitude

of the observed spiral in *Gaia* data, and could be used to constrain MW potential parameters.

4. Our model (c.f. Figure 2.5) shows that the timing of the spiral and vertical profile of the disc are strongly covariant parameters. This dependence, while generally established, has been shown explicitly in our work.

5. The method presented in Section 2.4.3 can be used to generate many spiral models under, 1. different types of perturbations (e.g. different interaction geometries between satellite and disc) 2. different MW potentials.

The sample of stars with measurable radial velocities is expected to increase in *Gaia* DR4, sharpening our view of the AM spiral, and emphasising the need for further theoretical development. Future development could also consider additional orbital information, such as metallicity, to try and precisely locate a perturbation time (e.g. Frankel et al., 2024). The model presented in this work is a step towards unifying the different projections of the local disequilibrium in the MW, and is a promising avenue to try and constrain not only the cause of the perturbation, but also the dynamical structure of the MW.

Chapter 3

The radial variation of the LMC-induced reflex motion of the Milky Way disc observed in the stellar halo

Foreword

When the first measurement of reflex motion was made in Petersen & Peñarrubia (2021b), the parameters of the reflex motion model were comprised of a velocity dipole (direction and amdplitude of disc motion) and the mean velocities in the outer halo after accounting for reflex - bulk motions. The parameters of the dipole were well understood, it is the speed and direction of disc motion. However, when it came to the bulk motions, their work did not explore these parameters in detail. Additionally, their measurement of reflex motion was a single measurement against halo stars with distances of $r > 40$ kpc, but in order to make a quantitative comparison against MW-LMC simulations, the radial variation in the reflex motion model parameters needed to be recorded. Motivated by these two points i) Understanding the subtleties of the bulk motions in the halo (the internal response of the halo to the infall of the LMC) ii) Measuring the radially varying signal in reflex motion and comparing against simulations, we set out to measure the radial variation of reflex motion in the MW. In hindsight, this paper seemed almost a natural extension to the detection paper of Petersen

& Peñarrubia (2021b).

3.1 Introduction

The presence of the Large Magellanic Cloud (LMC) in the Milky Way (MW) halo complicates attempts to model the MW. Recent mass estimates of the LMC that include an extended LMC dark matter (DM) halo challenge equilibrium models of MW. Studies show that the LMC is in a first in-fall scenario[1] (as found early on by Besla et al., 2010) with a mass of $(1-3)\times 10^{11} M_{\odot}$ (Besla et al., 2012; Peñarrubia et al., 2016; Erkal et al., 2019a). The current evidence for a heavy LMC calls for the development of non-equilibrium MW models, as observations are already sensitive to the time-dependence observed in recent models (Rozier et al., 2022) and simulations (Garavito-Camargo et al., 2019a, 2021; Donaldson et al., 2022; Lilleengen et al., 2023).

A recent example of a time-dependent MW halo model with observational impact is Koposov et al. (2023b), where the MW halo and disc were modelled as rigid bodies and allowed to move relative to the LMC. This time-evolving potential was used to fit the Orphan (OC) stream kinematic data. Their result showed that the when allowing the MW to react to the infall of the LMC, the resulting time-dependent potential is able to better match the OC stream velocity track on the sky (and a model without the LMC could not). Building on this work, a fully self-consistent modelling of the MW-LMC system was performed by Lilleengen et al. (2023), where the time-evolving potentials of the MW and LMC were used to generate mock OC-like streams. In their OC-like streams, they found that the effects of time-dependent deformation in the MW and LMC DM halos on the stream were larger than observational errors.

Gómez et al. (2015b) first showed that the presence of the LMC will cause the displacement of the MW disc from its equilibrium location at the barycentre of the total MW[2]. This displacement should be detectable as a dipole in velocity, when measured using halo stars with large dynamical timescales (Petersen & Peñarrubia, 2020a, PP20 hereafter). Petersen & Peñarrubia (2021a, PP21 hereafter) detected the LMC-induced displacement of the MW disc by measuring

[1] Recent modelling of the MW-LMC system have found plausible second-passage scenarios (Vasiliev, 2024); however, as we shall see below, the results in this work remain unchanged.

[2] For recent dark matter halo models of the MW, the barycentre is controlled by the dark matter, which outweighs the stellar disc by roughly a factor of 20.

a signal in the observed galactic velocities of halo stars[3], where the disc travel velocity was found to be $v_{\rm travel} = 32^{+4}_{-4}$ km s^{-1}, using a Galactocentric velocity dipole model, and using only the stars with large dynamical timescales by selecting stars at $r_{\rm galactocentric} > 40$ kpc. In addition to the travel velocity, the direction of the disc motion (apex direction) was also recovered from the same model. The location of the apex was found to point along the previous trajectory of the LMC with $(\ell, {\rm b})_{\rm apex} = (56°, -34°)$. Their result hints at the possibility that the there is valuable information of the trajectory of the LMC in the the velocity and direction of disc motion. One of the implications of the work in PP21 is that studies of the MW stellar halo should take into account the reflex motion of the disc, as neglecting this will likely introduce biases in the kinematics of the halo stars (see, e.g. Erkal et al., 2020; Deason et al., 2021).

Following the work of PP21, this paper investigates the dependence of the reflex motion signature on Galactocentric distance, motivated by the findings of PP20, who demonstrated that the LMC-induced dipole signal should vary with Galactocentric distance. I use the same velocity dipole model as in PP21 to characterise how the measured reflex motion varies with Galactocentric radius. At the radii used in PP21 ($r_{\rm galactocentric} > 40$ kpc), the orbital timescale of stars is $\gtrsim$1 Gyr, which leaves little time for the outer halo stars to react to the infalling LMC. In contrast, the inner halo will likely be responding to the LMC differentially with distance, including the limit where the innermost part of the halo will be following the disc potential, and exhibit no reflex motion signal. In the transition region between the inner most and outer halo, the reflex motion signature will be a complex function of the mass ratio of the LMC to MW, the orbital history, and the deformations of the MW and LMC.

In Section 3.2, I describe the stellar halo data introduced in PP21, and collect a range of models for the MW-LMC interaction. The comparison between models shows that different model assumptions produce different dipole signals. Therefore, the observational measurements can be used to further constrain MW–LMC models in future studies. Section 3.3 outlines the reflex motion model used and the fitting parameters, and describes the corresponding measurements made in the simulations. Our results are in Section 3.4. We present the measured the reflex motion at various distance bins between 20 kpc and 50+ kpc, and the direction of disc motion along with the modelled halo mean spherical velocities. The results show the variation of the directions and magnitude of disc motion.

[3]Corroborated with line-of-sight velocity analysis in Erkal et al. (2021a).

The results are compared to the various LMC-MW simulations described in Section 3.2. Section 3.5 discusses the observed radial dependence of the reflex motion parameters, and explores the possible dynamical justifications for the observed signal in the inner and outer halo. We describe the response of the disc when measured against stars at the large, intermediate and small distances. The limitations of the dipole model are assessed through various tests performed using mock catalogues generated from the simulations presented (see also the Appendices). Additional limitations of the sky coverage and tracer selection are discussed in this section. We conclude in Section 3.6.

3.2 Data and Models

3.2.1 Data

In this section, I briefly summarise the catalogue creation. I use the sample of K Giants and blue horizontal branch (BHB) stars assembled in PP21. K Giants and BHBs, known to be good halo tracers, were identified using SDSS/SEGUE photometric and spectroscopic data(Yanny et al., 2009). The positions and distances (and their uncertainties) are not modified beyond what is present in the SDSS/SEGUE data. A colour-cleaning technique was applied to the BHB sample to identify Blue Stragglers with the prescription of Lancaster et al. (2019). The BHB and K Giant catalogues were cross-matched with GAIA DR3[4], accepting stars with a reduced unit weighted error of `ruwe`<1.4. The observed proper motions were converted to galactocentric coordinates with no loss of precision.

Sagittarius is the largest known substructure in the galactic halo and has members identified beyond galactocentric $r > 20$ kpc. Members are present by eye when inspecting the parent sample. I performed the following cleaning of Sagittarius from the sample. I remove Sagittarius stream members from the sample by defining an angular momentum sphere of radius of 3000 kms^{-1}kpc around the location of the Sagittarius dwarf at $\vec{L}_{\rm sgr}$=(+605, -4515, -1267)km s^{-1} kpc (Peñarrubia & Petersen, 2021). Stars in the plane of Sagittarius defined by Majewski et al. (2003) with $B_{\rm sgr} < 20^{\circ}$ that also fall in the sphere in angular momentum are tagged as Sagittarius members. Tests against the high-probability

[4]In PP21 Gaia DR2 was used, however, the catalogue was updated for this work.

Sagittarius membership catalogue defined in Peñarrubia & Petersen (2021)[5] suggest that no more than 10% of the population remaining after the naive angular momentum cut are Sagittarius members.

In summary, the resulting dataset used in this work is identical to the individual stellar object samples of PP21 with the following differences: I use updated Gaia DR3 data and include stars from $r > 20$ kpc. The final dataset has the following number of stars: $N_{\text{K giant}} = 2830$, $N_{\text{BHB}} = 1445$. Finally, the data was binned in bins of 10 kpc between 20-50 kpc, halo stars with $r > 50$ kpc were grouped in the same bin with a median distance in the bin of $\simeq 59$ kpc. Further binning beyond this radius leaves too few stars to fit. The final dataset consists of $N = 4275$ (K Giants + BHBs), with $N = [2457, 1016, 446, 340]$ with bin centres of $r_{\text{galactocentric}} = [25, 35, 45, 50+]$ kpc. In Appendix B.1, I test the effect of the SDSS sky coverage on our results. In Appendix B.2, I test the effect of fitting K Giants and BHBs separately.

3.2.2 Models

To connect the data to the dynamics of the MW-LMC interaction, I use a collection of published literature models. Broadly, there are two classes of simulations: idealised models that are highly efficient at probing dynamical principles, and self-consistent simulations that seek to capture the complete dynamics of the MW-LMC system. In Table 3.1 I summarise the relevant parameters of the models.

Idealised models

PP20 presented a suite of simulations featuring three different mass ratios (10%, 20%, and 30% of the MW mass) of Plummer softened point mass LMCs introduced to a fiducial MW model. The LMC models were softened to match the stellar rotation curve of the LMC constraint from van der Marel & Kallivayalil (2014) while reaching the overall LMC target mass. These idealised models were run with EXP (Petersen et al., 2022a), a flexible basis-function expansion code. Only the 10% model was analysed in PP20, demonstrating that even at low mass ratios, the LMC is able to induce significant displacement of the MW barycentre

[5]The catalogue is available at `https://github.com/michael-petersen/SgrL`.

Table 3.1: Summary of MW-LMC models studied in this work.

Simulation	Self-Consistent?	$M_{\mathrm{LMC},0}/M_{\mathrm{MW}}$	MW halo profile	MW scale radius (kpc)	LMC halo profile	LMC $(\ell, b)_{r\to\infty}$
GC19	✓	0.115	Hernquist	16.7[a]	Hernquist	$\ell \simeq 90°, b > 0°$
E19 responsive	✓	0.158	NFW	18.5	Hernquist	$\ell \simeq 90°, b < 0°$
PP20 10%	✗	0.1	NFW	14.1	Plummer	$\ell \simeq 90°, b > 0°$
PP20 20%	✗	0.2	NFW	14.1	Plummer	$\ell \simeq 90°, b > 0°$
E20	✗	0.15	NFW[b]	16.0	Hernquist	$\ell \simeq 90°, b \approx 0°$
D22	✓	0.238	NFW	15.0	NFW	$\ell \simeq 90°, b < 0°$
L23	✓	0.158	NFW	12.8	Hernquist	$\ell \simeq 90°, b < 0°$
V24	✓	0.273[c]	NFW	16.5	NFW	$\ell \simeq 0°, b < 0°$[d]

The three different types of models are Hernquist (Hernquist, 1990), NFW (Navarro et al., 1997), and Plummer (Plummer, 1911b).

[a]The Hernquist scale radius is not the same measurement as the NFW scale radius. While GC19 reports 40.82 kpc as the Hernquist scale length, the
comparative measurement, where $\mathrm{d}\log\rho/\mathrm{d}r = -2$, is given here.

[b]This MW halo is the same as that in `galpy`'s `MWPotential2014` (Bovy, 2015).

[c]At the time of the most recent pericentre, the mass is approximately half of the infall mass (cf. the ODE solution in Section 3.1 of V24).

[d]As the V24 are second-passage models, the location of the LMC as $r \to \infty$ is probably not the parameter controlling the location of the peak reflex signal,
but I defer this investigation to future work.

– resulting in observable reflex motion signals. Crucially, that paper also showed that the LMC-induced dipole signal varies with galactocentric distance. The models were later analysed in more detail in PP21, demonstrating a trend in reflex motion strength with increasing LMC mass ratio (and validating the model technique; see also Appendix B.3).

To quantify the biases when measuring the overall MW mass from the LMC-induced distortion, Erkal et al. (2020, E20 hereafter) analysed a stellar halo in a non-deforming MW DM halo potential as the LMC was brought in along a trajectory found by rewinding the LMC from present-day observables with a prescription to mimic dynamical friction. This relatively simple model captures the bulk motion of the MW disc relative to the stellar halo. However, the signal is likely underestimated owing to the non-responsive nature of the MW DM halo.

The idealised models capture the response of the MW stellar halo, but should not be expected to either capture the true trajectory of the LMC or the deformation, dynamical friction, and mass loss of the LMC nor necessarily the response of the MW potential. However, these models are generally less computationally expensive to run, which enables larger numbers of particles and the ability to explore more models rapidly. An appropriate compromise for measuring reflex motion properties appear to be models that feature a deforming MW (as in, e.g., PP20), even with a fixed LMC.

Self-consistent models

Garavito-Camargo et al. (2019a, GC19 hereafter) presented the first of the modern MW-LMC simulation suites. Their work explored the dynamical response of the MW DM halo to the passage of the LMC, finding that the response could be separated into two categories, the 'local wake' (a manifestation of dynamical friction trailing the LMC) and the 'collective wake' (a resonantly driven response that can span the entire DM halo). In addition to those deformation effects, GC19 predicted a north/south reflex signature in line of sight velocities owing to the displacement of the MW disc. While the measurements below are in principle sensitive to the local and collective wakes, I expect the dominant signal to owe to the reflex signature — an assumption I verify when calculating the all-sky reflex motion signatures resulting from the displacement of the MW disc with respect to the MW DM halo barycentre (Section 3.4). In this work, I analyse the 'fiducial' model, their Model 7 (see Table 1 in Garavito-Camargo et al., 2021). This model

features a radially biased MW halo and lightly rotating halo, which other works have suggested impacts the observed dynamical response (Rozier et al., 2022).

Donaldson et al. (2022, D22 hereafter) presented a higher resolution version of the mass model used in Petersen et al. (2022b) for the purposes of investigating the DM distribution in the solar neighbourhood. These models were used to characterise the effect of deformation in both the MW and LMC at the solar neighborhood, and in particular compared local diagnostics when the MW or LMC was not responsive. In passing, D22 reported a reflex motion signal of 51 $\mathrm{km\,s^{-1}}$, which is effectively a mean value for all halo particles (with the omniscience provided by the simulation).

Lilleengen et al. (2023, L23 hereafter) presented an updated self-consistent version of the best-fit spherical model proposed in Erkal et al. (2019a, E19 hereafter)[6]. This model features a modestly less concentrated MW halo than the originally fit E19 model, using $r_\mathrm{s} = 18.5$ kpc instead of $r_\mathrm{s} = 12.8$ kpc. In practice, this results in a modestly different LMC trajectory, but the response features are similar, including the reflex amplitude and direction of disc travel. For completeness, I have also produced a new version of the exact model parameters found for a reflexive spherical MW+LMC model in E19 (listed as 'responsive' in Table 3.1). Both models were run with EXP, with simulation parameters describe in L23. The differences in the reflex amplitude can be attributed to the concentration of the halo, but this appears to be a subdominant effect to the ratio of the LMC to MW mass.

L23 quantified the deformation of the MW DM halo in their Figure 1, finding that the dipole is the strongest feature, but the quadrupole (which is not accounted for in our model) is also a non-negligible contributor. Future work can explore the extension of the dipole model to encompass this signal.

Vasiliev (2024, V24 hereafter) ran a suite of models designed to probe the possibility of an LMC pericentre several Gyr before the most recent pericentre. As a representative model, I choose to compare to the model combining $\mathcal{L}3$ and $\mathcal{M}11$[7], resulting in an initial mass ratio of $M_\mathrm{LMC}/M_\mathrm{MW} = 0.273$. However, the LMC model loses approximately half the infall mass on the earlier pericentric passage, which makes the most recent pericentre better approximated by a smaller mass ratio when comparing to single-passage models. To make a more

[6]See the 'sph. rMW+LMC' parameters in their Table A1.

[7]I check here that the other models produce similar reflex motion signatures, so they are not included in my analysis.

fair comparison with first-infall models, I approximate the infall mass ratio as $M_{\rm LMC}/M_{\rm MW} = 0.138$, consistent with the value used for the ODE orbit approximation in Section 3.1 of V24.

Compared to idealised models, these self-consistent models are significantly more computationally intensive to run, a fact borne out by the reduced MW particle numbers in each run, making discreteness noise apparent in the curves of Figures 3.1 and 3.2, which I would expect to be smooth in the mean field limit. However, despite their lower resolution, the self-consistent models are crucial for resolving the full dynamical response of the MW and LMC owing to their interaction. One particular limitation of the current generation of MW-LMC models, both idealised and self-consistent, is a lack of cosmological context. In particular, all the models I analyse in this work begin with spherically symmetric MW and LMC halos. The next generation of models should explore, at a minimum, the implications of triaxial halos for the reflex motion signal.

3.3 Methods

In this section I describe the model parameters and fitting procedure used to measure the reflex motion. I employ the method used in PP21 here on the binned stars defined in Section 3.2.1. The analysis was performed using the six-dimensional phase space information of stars in our sample, where the data contains (for each star) galactic coordinates (ℓ, b), distance (D), proper motions $(\mu_\ell, \mu_\mathrm{b}$ and the correlation $\rho_{\mu_\ell \mu_\mathrm{b}})$ and line-of-sight velocities $(v_{\rm los})$.

As in PP21, for each fit, the reflex motion model contains nine free parameters. The first three parameters describe the reflex motion induced by the LMC: the magnitude of disc motion $v_{\rm travel}$ and apex directions $\ell_{\rm apex}$, $b_{\rm apex}$, which combine to make the three-dimensional vector describing the disc motion, $\vec{v}_{\rm travel}$. Further, the model accounts for any non-zero mean motion in the halo velocity through the bulk (mean) motion parameters $\langle v_r \rangle$, $\langle v_\theta \rangle$, and $\langle v_\phi \rangle$.

In the Galactocentric coordinate system, the system is rotated such that the z-axis is aligned with the disc motion and points to $\ell_{\rm apex}$, $b_{\rm apex}$. To rotate the coordinate system, the following Euler rotation matrix was used to make the

transformation[8]

$$(\phi, \theta, \psi)_{\rm rot} = \left(\ell_{\rm apex}, \pi/2 - b_{\rm apex}, 0\right), \tag{3.1}$$

where ϕ, θ, ψ are the Euler rotation angles. In this frame the Cartesian representation of $\vec{v}_{\rm travel}$ is simply $(0, 0, -v_{\rm travel})$ i.e. the reversed reflex motion of the MW disc w.r.t to the stellar halo. Conversions between heliocentric Cartesian and Galactocentric Cartesian were performed by adopting a right-handed Cartesian coordinate system with the Sun positioned at $\vec{r}_{\odot \rightarrow MW} = (-8.3, 0.0, 0.02)$ kpc (GRAVITY Collaboration et al., 2019; Bennett & Bovy, 2018a), with velocity $\vec{v}_{\odot \rightarrow MW} = (11.1, 244.24, 7.24)$ $\mathrm{km\,s^{-1}}$ (Schönrich et al., 2010b; Eilers et al., 2019b). To find the average velocity vector of the halo using the six parameters defined above, the reflex motion model is represented by the sum of the dipole and bulk motion parameters,

$$\langle \vec{v} \rangle = \langle \vec{v}_{\rm travel} \rangle + \langle v_r \rangle + \langle v_\phi \rangle + \langle v_\theta \rangle - \vec{v}_{\odot \rightarrow MW} \ , \tag{3.2}$$

where $\langle \vec{v} \rangle$ is the mean velocity vector of the halo in the galactocentric frame. To transform $\langle \vec{v} \rangle$ to observed velocities, I project the velocities to galactic coordinates using the unit vectors aligned with line-of-sight and (ℓ, b) galactic coordinates (equations 3 and 4 in PP21).

In order to fit the data to the model, I obtain the posteriors on the model parameters by adopting a Gaussian likelihood. The likelihood is the product of two normal probability functions. The first is a 1D distribution for the line-of-sight velocity and the second is a 2D distribution for the proper motions containing also the covariance between the proper motions in the covariance matrix (equations 5, 6 and 8 in PP21). The final three model parameters are the hyperparamaters $\sigma_{\rm h,los}, \sigma_{\rm h,\ell}$ and $\sigma_{\rm h,b}$. The hyperparameters are added in quadrature to the variances of the observed data and are used to minimise the covariance between the rest of the model parameters.

In summary, the nine free parameters are the magnitude of disc motion $v_{\rm travel}$, the apex directions $\ell_{\rm apex}, b_{\rm apex}$, and the mean spherical velocities of stars $\langle v_r \rangle, \langle v_\theta \rangle, \langle v_\phi \rangle$ and the hyperparameters for each of the observed galactic velocities $\sigma_{\rm h,los}, \sigma_{\rm h,\ell}$ and $\sigma_{\rm h,b}$.

[8] I use the *xyz* convention for the rotation matrix.

3.3.1 Inference

The fitting was performed using a nested sampling technique, which samples the posterior through computation of the evidence, via the Multinest (Feroz & Hobson, 2008) package in Python (Buchner et al., 2014). Multinest returns posterior samples and error estimates of the evidence. All priors are flat, with exception of the intrinsic scatter parameters which have inverse/Jeffreys priors. For a complete description of the likelihood used here, the reader is referred to the Methods section in PP21.

3.3.2 Measuring the Dipole Model Parameters from Simulations

I define here the procedure that was used to calculate the values of the reflex motion model parameters directly from the Cartesian 6D phase space information of the LMC-MW simulations. I do this in order to test the Bayesian inference code as well as to gain understanding of the physical meaning of the model parameters. Notice that since the mean velocity of halo particles is a combination of both the bulk motion of halo stars and the reflex motion of the MW disc, these parameters can be decoupled only by fitting them simultaneously. However, using only the 6D phase space information of stars from the simulation *without fitting*, it is not possible to fully decouple the bulk velocities ($\langle v_{\mathrm{r},\phi,\theta} \rangle$) from the travel velocity as the reflex motion signal will project onto the measured velocity of halo stars. Nonetheless, tests of fitting the simulation have shown that at all radii, the travel velocity dominates in $\langle \vec{v} \rangle$ in Equation (3.2). Therefore, in order to compute the apex directions and v_{travel}, I simply compute the mean velocity of stars in each Cartesian direction using the halo stars within a given shell and transform to galactic coordinates. This is the definition of v_{travel} calculated *from the simulations*.

For the bulk halo velocities, I follow a similar procedure, however, the reflex motion must be accounted for. For any halo star in the disc frame with $r_{\mathrm{min}} < r < r_{\mathrm{max}}$, where $\mathrm{r_{min}}$ and $\mathrm{r_{max}}$ are the inner and outer radii of any given shell, I compute the mean velocity in each Cartesian direction of stars in that shell (the reflex) and then subtract the value from the velocity of each individual star. In this definition of an inertial frame the new velocity is given by $v_i' = v_i - \langle v_i \rangle$ where $i = [x, y, z]$. Then I computed the spherical velocities of those stars and compute

the mean spherical velocities of the halo in that shell. The bulk motions of the halo are defined in this frame that minimised aliasing of the reflex signal onto the spherical halo velocities.

In all the results of the reflex motion obtained from simulations, it is important to note that the response of the halo is continuous with radius, and that calculating averages from shells may not be accurately representing the true underlying continuous distribution. With that said, the resolution of the simulation will almost always affect the choice of shell width, as more stars will lead to the ability to calculate the reflex and bulk motion parameters without running into discreteness noise. As I are presenting simulations with different particle numbers and techniques (and therefore resolution), I chose a bin width of 6 kpc, which is close to the bin width of 10 kpc in the data. I explore the effects of binning on the results in Appendix B.4.

3.4 Results

The PP21 result showed that the MW disc was not at rest with respect to the outer halo. This first measurement of reflex motion found that the disc travel velocity was $\sim$ 30 $\mathrm{km\,s^{-1}}$ in a sample of halo tracers with distances of $r > 40$ kpc[9]. Building on this work, I find that a single measurement of the reflex motion does not provide sufficient constraining power when comparing to self consistent LMC-MW models – see the red data points in Figures 3.1 and 3.2, which are the measurements from PP21. I find the parameters of the dipole model described in Section 3.3 change when measuring the signal using stars at varying galactocentric radii. Furthermore, reflex motion measured directly from idealised and self-consistent LMC-MW simulations (see Section 3.2.2) are shown alongside the data results to contrast existing models against observations.

In this Section, I report the measurements of the reflex motion dipole in Section 3.4.1, the measurements of bulk velocities in Section 3.4.2, and compare the results with simulations in Section 3.4.3.

[9]The stellar measurements were made using the same sample of K giants and BHBs as in this work; the satellite galaxy sample used in PP21 is not large enough to be divided into bins, as was done here. I therefore do not use this sample. Similarly, the MW globular clusters are largely located at the centre of the MW, where the reflex motion signal is expected to be small.

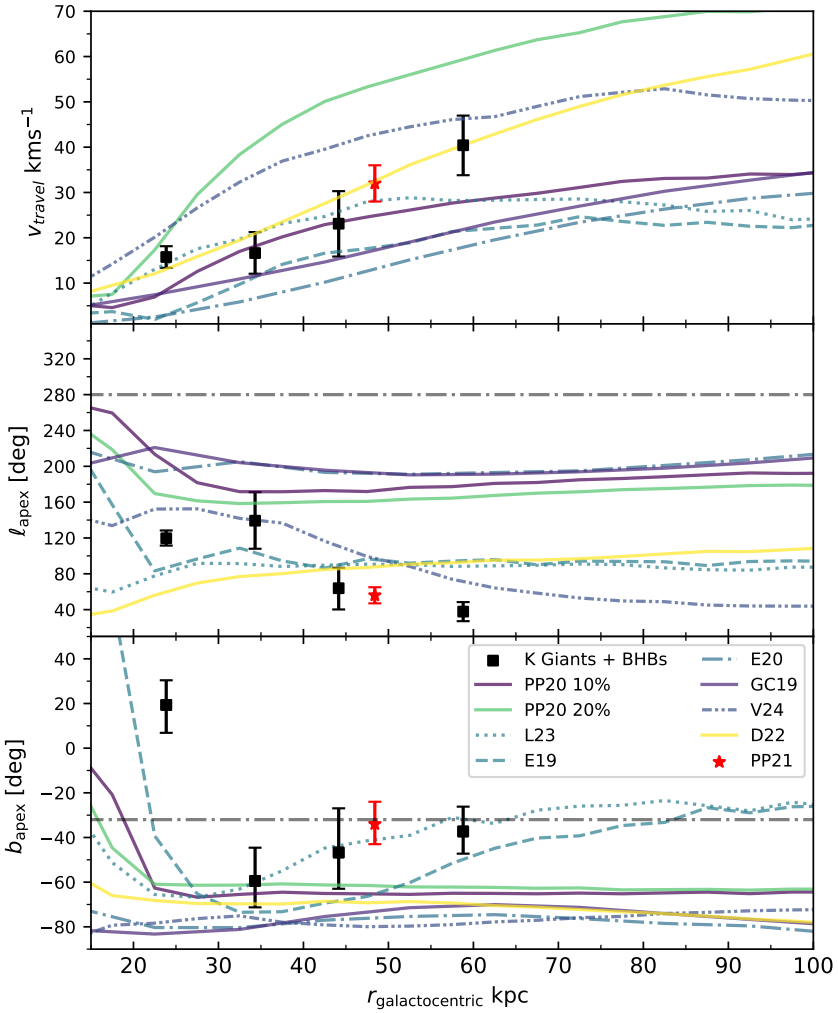

Figure 3.1: The measured values for the travel velocity and apex directions versus the median galactocentric distance of stars in each bin. Top panel: fitted travel velocity in each bin with uncertainties given as the standard deviation of the posterior chains of the parameters. Middle panel: Measured $\ell_{\rm apex}$ values for stars in each bin, note that I have restricted the apex longitude to be between 25° and 340°. Bottom panel: Measured $b_{\rm apex}$ values for stars in each bin, where the range of latitude angles are limited to −90° and 50°. In each panel, I plot corresponding measurements from the set of simulations (see text for details in calculating the simulation curves). Colours of model curves correspond to the ratio of initial LMC mass to MW mass, with darker colours closer to 10% and lighter colours closer to 25%. The red point is the measured value for the parameters from PP21 using stars with r>40 kpc. The grey dash-dotted line shows the present day position of the LMC. Error bars indicate the 1σ width of the posterior distribution for each parameter. See Table 4.1 for simulation names and mass ratios and Table 3.2 for the measured values and their uncertainties.

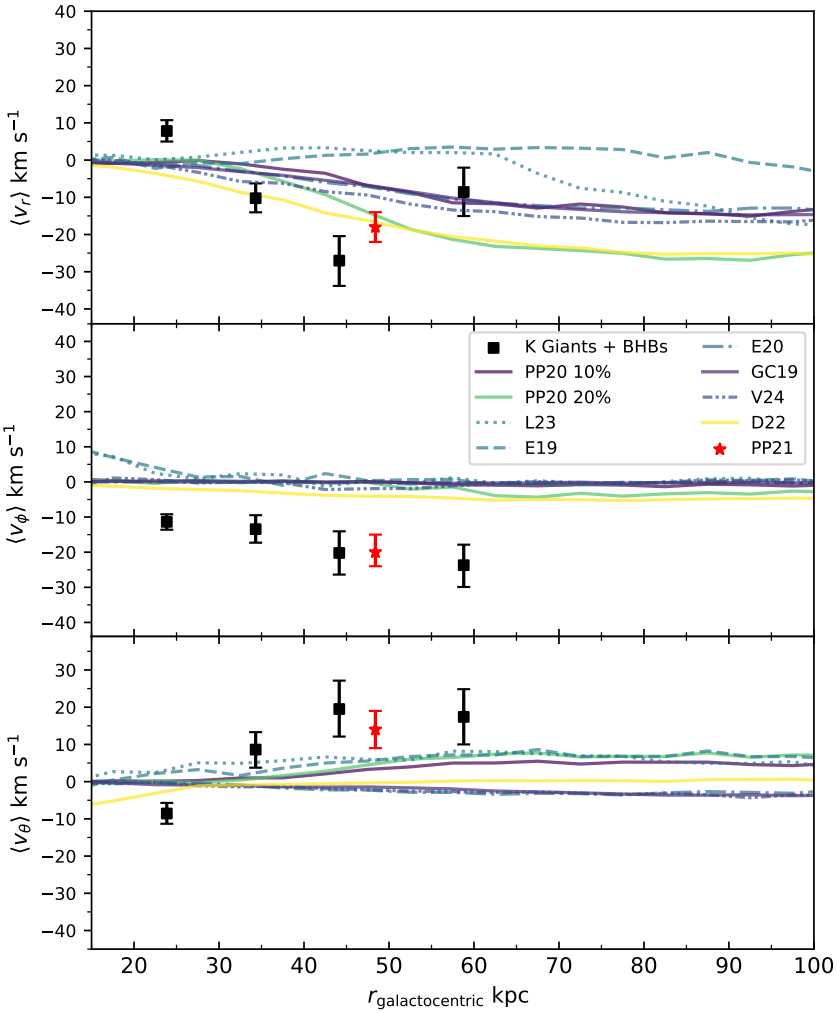

Figure 3.2: The measured halo bulk motion parameters as a function of galactocentric radius. Top panel: Mean halo motion in the radial direction. Middle panel: Mean halo motion in the azimuthal direction. Bottom Panel: mean halo motion in the polar direction. In each panel, I plot corresponding measurements from the set of simulations, which have been reflex corrected. The red point is the measured value for the parameters from PP21 using stars with r>40 kpc. Error bars indicate the 1σ width of the posterior distribution for each parameter. See Table 4.1 for simulation names and mass ratios and Table 3.2 for the measured values and their uncertainties.

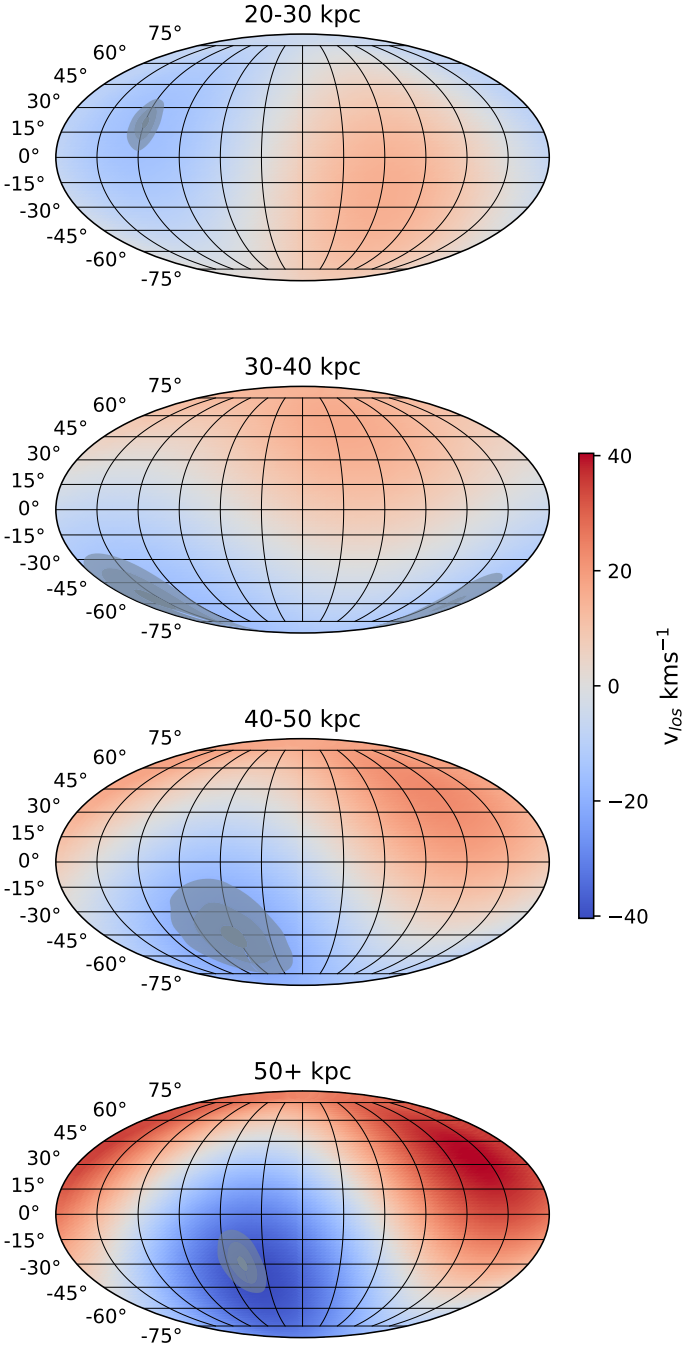

Figure 3.3: The on-sky line-of-sight velocity amplitude resulting from the dipole component of our reflex motion model, shown in Mollweide projection. Different panels correspond to different distances, from smallest radii (top) to largest radii (bottom). The amplitude of the signal increases with distance, and the apex location (with 67%, 90% and 95% confidence ellipses shown in grey) moves across the sky (cf. Figure 3.1) – not tracing the orbit of the LMC, but rather the historical motion of the MW disc.

Table 3.2: Summary of the dipole model fit results. All uncertainties on the values of the fitted parameters are the 1σ widths of the posterior distribution.

Description of Parameter	parameters	Units	20-30 kpc	30-40 kpc	40-50 kpc	50+ kpc
Disc barycentric velocity	$v_{\rm travel}$	$\mathrm{km\,s^{-1}}$	16^{+2}_{-2}	17^{+5}_{-5}	23^{+7}_{-7}	40^{+7}_{-7}
Apex longitude	$\ell_{\rm apex}$	deg	120^{+9}_{-8}	139^{+32}_{-31}	64^{+23}_{-24}	38^{+11}_{-11}
Apex latitude	$b_{\rm apex}$	deg	19^{+11}_{-12}	-59^{+15}_{-12}	-47^{+20}_{-16}	-37^{+11}_{-10}
Mean halo radial velocity	$\langle v_r \rangle$	$\mathrm{km\,s^{-1}}$	8^{+3}_{-3}	-10^{+4}_{-4}	-27^{+7}_{-7}	-9^{+7}_{-6}
Meal halo azimuthal velocity	$\langle v_\phi \rangle$	$\mathrm{km\,s^{-1}}$	-11^{+2}_{-2}	-13^{+4}_{-4}	-20^{+6}_{-6}	-24^{+6}_{-6}
Mean halo polar velocity	$\langle v_\theta \rangle$	$\mathrm{km\,s^{-1}}$	-9^{+3}_{-3}	9^{+5}_{-5}	20^{+8}_{-7}	17^{+7}_{-7}
Line-of-sight velocity hyperparameter	$\sigma_{\rm h,los}$	$\mathrm{km\,s^{-1}}$	103^{+2}_{-2}	98^{+2}_{-2}	100^{+4}_{-4}	87^{+4}_{-4}
Galactic longitude velocity hyperparameter	$\sigma_{\rm h,\ell}$	$\mathrm{km\,s^{-1}}$	76^{+1}_{-1}	78^{+2}_{-2}	85^{+4}_{-4}	70^{+5}_{-4}
Galactic latitude velocity hyperparameter	$\sigma_{\rm h,b}$	$\mathrm{km\,s^{-1}}$	61^{+1}_{-1}	83^{+3}_{-2}	96^{+4}_{-4}	74^{+5}_{-5}
Median distance of stars		kpc	23.85	34.31	44.14	58.80
Number of stars			2461	1026	446	340

3.4.1 Radial Variation of the Travel Velocity

The likelihood defined in Section 3.3 is a powerful way to decouple the kinematic response of the MW disc and internal motion of the halo stars, without imposing a physical model for the MW-LMC system. The radial variation of $\vec{v}_{\rm travel}$ shows *in what direction* and *how fast* the disc is travelling, relative to an ensemble of halo stars – here, shells of halo stars. I present here the measured magnitude and direction of disc motion. Comparison against theoretical models suggests that response of the MW disc with radius is dependant on the MW and LMC mass profiles. Importantly, the direction of disc motion will also depend strongly on the infall trajectory of the LMC.

Our likelihood analysis indicates that that the reflex motion amplitude, $v_{\rm travel}$, generally increases with galactocentric radius in the data. The top panel Figure 3.1 shows the resulting measurements from the stellar halo sample as black points. I find also that the measured on-sky direction of disc motion changes with radius. The lower two panels of Figure 3.1 show the on-sky location of the apex in Galactic coordinates (ℓ, b). I find that $\ell_{\rm apex}$ is in the opposite half of the sky from the present-day location of the LMC at 20-30 kpc then *becomes closer* in angular separation to the present-day LMC location in the more distant bins[10]. The apex longitude, $\ell_{\rm apex}$, continues to slowly decrease, scanning across the sky, to a minimum value of $\sim 40^\circ$ in the final bin containing only stars with r> 50 kpc. As expected from the number of stars in each bin, the uncertainties on the fitted $\ell_{\rm apex}$ parameters are smallest in the 20-30 kpc bin with a 1σ uncertainty of about 10°. In the following bin at 30-40 kpc, I find that the errors are roughly 4 times larger, much larger than expected when considering the distance errors and the number of stars are not too small in that bin, complicating robust inference of how much the $\ell_{\rm apex}$ location may really be changing.

The apex latitude $b_{\rm apex}$ is, surprisingly, measured to be in the Northern galactic hemisphere in the closest bin, then points toward the Galactic South in the subsequent bins. However, the location is always measured to be $b_{\rm apex} > -60^\circ$, suggesting that rigid models treating the reflex motion as purely downward at a fixed direction are too simplistic to capture the observed behaviour. The uncertainty in the fitted $b_{\rm apex}$ values does not vary greatly between the bins with 1σ widths of approximately 10°. The small change in the uncertainties on

[10]Note that in Figure 3.1, the points seem be further away in distance, however considering the wrapping of the angular coordinate, the points approach the present day position of the LMC in terms of on-sky separation – highlighting the need for fits at different radii.

the fitted values is likely due to the dependence of the apex latitude fit on the sky coverage of the sample[11].

In summary, all three $\vec{v}_{\rm travel}$ parameters change with radius: $v_{\rm travel}$ increases gradually with radius, and the apex angles approach the present-day location of the LMC with increasing distance, encoding information about the trajectory of the LMC.

3.4.2 Radial Variation of the Bulk Motion parameters

In addition to the dipole model, I measure the 'bulk motion' of the stellar halo, fit as three spherical velocity components with an all-sky mean value: the mean radial velocity $\langle v_r \rangle$, the mean azimuthal velocity $\langle v_\phi \rangle$ (cylindrical rotation), and the mean polar velocity $\langle v_\theta \rangle$. The mean velocities describe the velocity signal of the halo *distinct from* the reflex dipole. In addition to describing the response to the LMC infall, the mean velocities also describe any pre-existing ordered motion within the shells after removing the reflex dipole. Perturbations such as a heavy LMC infall will affect not only the disc, but also the internal kinematics of the halo stars. The mean velocities in the halo could also encode any intrinsic rotation that the halo could have had prior to the infall of the LMC. The crucial step in our work when measuring the bulk motions through the likelihood approach is that the reflex motion of the disc is robustly accounted for when measuring the mean motion parameters.

The mean radial velocity $\langle v_r \rangle$ of the bulk halo motion show statistically-significant non-zero amplitude in the data, which varies with radius. In the innermost bin, I measure $\langle v_r \rangle = +8$ km s^{-1} with the positive sign meaning that the halo is expanding. Moving outward, v_r decreases to a minimum value (but maximum amplitude) of $v_r = -27$ km s^{-1} in the distance bin of 40-50 kpc, i.e. the halo is contracting at present. In the farthest bin, the result is consistent with no radial motion within the 1σ posterior width of the fitted value. The uncertainties on the fitted bulk motions increase by about 1km s^{-1} at each successive bin, and they are the largest in the last bin, as would be expected for a decreasing number of stars in each successive bin.

For the mean azimuthal velocity $\langle v_\phi \rangle$, I find a consistent rotation trend with increasing galactocentric radius between 20-50+ kpc, with maximum amplitude

[11] In Appendix B.1, I explicitly test the effect of sky coverage.

of $v_\phi = -24^{+6}_{-6}$ km s^{-1} at the 50+ kpc bin. This rotation signal was measured to be statistically significant and prograde (in the same sense as the disc rotation) at all radii. Finally, the bulk polar motion in the shells of halo stars is largely consistent with zero velocity.

Using the bulk motion parameters of the dipole model, the results from the data show that the MW halo is experiencing compression, whose effect is greatest on halo stars between 40-50 kpc. The data also show evidence of mild cylindrical rotation with a prograde direction at all radii.

3.4.3 Dipole Model Parameters in Simulations

The eight MW-LMC simulations collected for this work largely show the same results: a strong dipole signal, with a well-defined on-sky apex, and minimal bulk (mean) velocity signals caused by the LMC infall. Further, the models exhibit similar trends with radius. At 100 kpc, the models have largely reached the 'impulsive' regime where the dipole signal becomes distance invariant (cf. PP20). The similarity of the model predictions poses a challenge for distinguishing between models using current-generation reflex motion measurements, this will be studied in a follow-up contribution.

For $v_{\rm travel}$, in the intermediate bins (30-50kpc) the PP20, GC19, E19, D22 and L23 models are consistent with the magnitude of $v_{\rm travel}$ within 1σ, but do not show the same agreement in the 20-30 and final 50+ kpc bin. All live MW-LMC simulations show a flattening of $v_{\rm travel}$, however, the radius at which the profile begins to flatten is not consistent between the simulations. Furthermore, the slopes of $v_{\rm travel}(r)$ vary between the simulations with E20 showing an almost linear increase between 20-100 kpc while others show a profile that increases more rapidly and then flattens out at large radii. This difference in profile likely corresponds to the model choices (e.g. profile, mass, etc.) made for the LMC and MW in those simulations. Additionally, the PP20 models for the LMC show a clear difference in $v_{\rm travel}$ with mass, where the assumed LMC-MW mass ratio increases the magnitude $v_{\rm travel}$ at any fixed radius, but also sets where the profile flattens. The difference, in the form of an apparently exaggerated signal, in the idealised models from PP20 relative to the self-consistent models suggests that the response of the LMC to the Galactic tidal field may be crucial to appropriately modelling the reflex motion.

For $\ell_{\rm apex}$, there is a large variation between the simulations. In the inner halo at r<40 kpc, the behavior of the live and simple PP20 simulations is not consistent, suggesting that further detailed modeling is required.

In terms of the present-day location of the LMC, the D22, V24, L23 and E19 are approximately 180° away from the LMC, while the E20 and PP20 models are closer to the present-day location of the LMC at approximately 90° away. All first-passage models do not show significant variation with radius at distances beyond 30 kpc, but all have an abrupt change in the $\ell_{\rm apex}$ profile at small distances. I notice two apparent families of behaviour of $\ell_{\rm apex}$ in the models, where the longitude points at two different quadrants of the sky in the simulations. If the LMC is indeed on a second passage, as modeled in V24, the earlier infall of the LMC may 'pre-process' the halo in ways that our dipole model does not fully capture.

For the apex latitude, I find that GC19, E20 and V24 show almost no variation in $b_{\rm apex}$ as a function of radius – pointing largely at the Galactic South pole. However, E19 and L23 both show similar profiles in $b_{\rm apex}$, where in the inner halo the apex latitude becomes more negative (or decreases from positive to negative), then increases slowly with increasing radius, up to about 90 kpc where the profile begins to flatten. Given the present-day latitude of the LMC of $b = -32°$, almost all models do not point at that location, but are offset in $b_{\rm apex}$ consistently where $b_{\rm apex}$ remains constant at large (r> 40kpc) distances, except for the E19 and L23.

None of the simulations are in agreement with the data results in all six parameters simultaneously. There are some live models models that agree well with the data in $\vec{v}_{\rm travel}$ such as the D22 and L23. The largest discrepancy is seen in the bulk motion parameters, where the data show strong contraction in the halo between 20 and 50 kpc. Furthermore, the data show that there is a nonzero rotation signal in the bulk motion of the halo shells at all radii. Of the collected simulations, only GC19 includes any ordered motion in the stellar halo pre-LMC infall (in the form of modest nonzero halo spin), but does not match the observed values. Whether this mismatch of bulk motion parameters can tell us something about the ordered motion in the pre-LMC infall MW halo is a subject for future study. Another issue identified is that the 'downward' models (GC19; E20; V24) – where the LMC-induced reflex is approximated by a constant motion in the $-z$ direction relative to the MW disc – are apparently inconsistent with the apex locations I find in the data. As the apex points to the part of the halo that appears to be moving away from us most quickly at a given radius, our findings

support the idea that a disc motion does not point close to the galactic south pole. The live simulations presented here are able account for the magnitude of disc motion $v_{\rm travel}$ well at most radii.

3.5 Discussion

As shown in Section 3.3.2, ignoring the reflex motion dipole response induced by the LMC does not properly describe the net velocities in the stellar halo and may introduce bias in the measured bulk stellar halo velocities. This bias can affect measured properties of the MW halo (E20). The radial variation of the travel velocity of the disc provides an avenue to constrain the mass ratio of the LMC-MW interaction. In the scenario of the disc barycentre dislodging from the (previously) shared disc + halo barycentre, the radial reflex motion signature will depend on the profiles of the MW and LMC, as well as on the trajectory of the LMC[12]. The measurements made in this work put forward a way to test whether models are able to capture (in the same parameter space) the effect of the LMC's infall on the MW.

Recent studies have shown that the LMC on first infall may affect the trajectories of stellar streams (e.g. Koposov et al., 2023b), and thus bias the constraints on the Galactic potential derived from models that adopt a static MW halo. In this context, it is worth noting that measuring the DM profile of the MW using the Sagittarius stream has previously yielded contradictory results, e.g. (Law & Majewski, 2010b) find an oblate halo potential, where (Fardal et al., 2018; Johnston et al., 2005) find a prolate one. In contrast, (Bovy et al., 2016) find a spherical shape by modelling GD-1. While Koposov et al. (2023b) have improved the method by allowing the MW disc and halo to move as rigid bodies when modelling the effect of the LMC's infall on the OC stream, E19 found that the OC stream's track could still be fit using either of the three aforementioned shapes with equal quality.

As the LMC loses mass in the tidal field of the MW, attempting to measure the post-infall stellar halo properties of the MW will be greatly affected by the reflex motion of the disc. I show in Section 3.4 that the magnitude of disc velocity relative to the halo is non-zero even in the 20-30 kpc stars. Based on our analysis of a suite of different MW-LMC simulations, I propose that using simulations

[12]The trajectory itself also depends primarily on the mass profile of the MW.

alongside model-agnostic dipole measurements (varying with radius) may be a robust method to test assumptions about the *pre-infall* profile of the MW and LMC. Note that as the method shown in Section 3.3 describes the mean velocity of the MW stellar halo as the sum of reflex and bulk motion, the model-data comparison can be made using the stellar halo as a whole, rather than only observing the effects on streams.

3.5.1 The Inertial Frame and the Adiabatic and Impulsive Regimes

The reflex motion signature ($\vec{v}_{\rm travel}$) is best probed using halo tracers with large apocentres and long dynamical times (PP20), which have not yet responded to the LMC's infall. However, halo tracers at those distances will also be affected by the apparent reflex motion of the disc when observed from the disc frame. The likelihood approach used in PP21 and here decouples the velocity induced by the motion of the disc and the intrinsic motion of the halo through the modelling of the mean halo velocity as a sum of reflex and bulk motion. Measuring the reflex motion at smaller distances (where the orbital times of stars is $\lesssim$1 Gyr, at distances $\lesssim$40 kpc) shows that the magnitude of the travel velocity is smaller than at the most distant bin owing to the ability of the inner halo to respond differentially with radius to the gravitational pull of the LMC.

Deep in the MW potential well, the orbital times are sufficiently short compared to the LMC perturbation such that there is no differential effect with radius the perturbed orbits can mix in phase-space and any differential effect with radius is washed out. This is the *adiabatic regime*, where the magnitude of disc motion is minimal. In the adiabatic regime, the inner halo potential is dominated by the disc, and the deep potential at this region means that there is effectively no LMC deformation. If the assumption of the inertial galactocentric frame is made at an earlier time (before the LMC's infall), then reflex motion measured today using the most distant halo stars reflects the motion of the disc centre w.r.t. a pseudoinertial frame[13]. At very large distances, the large orbital times delays their response to the LMC such that their barycentre is likely still that of the pre-infall barycentre of the MW disc + halo system. Outside of some large radius,

[13]'Pseudoinertial' here means accepting the frame of a shell of halo stars at very large distances (e.g. $100 < r < 200$ kpc) as nearly matching the pre-infall inertial frame. I will refer to this below as the 'inertial' frame.

the reflex motion signal may be approximated as an instantaneous kick. Using the outermost stars in the halo (at r> 50 kpc) the motion of the disc appears to be impulsive (the *impulsive regime*), and the travel velocity measured using stars in the inertial frame will be maximal. The transition from an adiabatic regime to an impulsive regime will indeed depend on the mass profiles of the MW and LMC, and this dependence arises from how the differential response of the MW halo varies with radius. The reflex motion measurements used in this work provides an avenue for testing the differential response of the halo and how it depends on the orbital period of individual halo stars.

The various idealised LMC-MW simulations shown in Figures 3.1 and 3.2 (see also Table 4.1 for details), show that the current observational constraints are not distant enough to have reached an impulsive regime. Apex angles and mean spherical velocities in particular do not show evidence for radial convergence. Also, the reflex motion parameters measured directly from the simulations do not agree with the data. Each model shown in this work uses different assumptions about the profile of the LMC and the MW, although the majority adopts an NFW profile for the DM halo of the MW (GC19, being the exception). The effect of the various assumptions can be readily seen and lead to different predictions for $v_{\rm travel}$ and the apex angles. Interestingly, while models like E19 use the OC stream to constrain the profiles of the LMC and MW, the resulting reflex motion parameters do not reproduce the reflex motion of the MW disc. These results call for a future theoretical efforts to fit stream motion-track and the reflex motion of the disc simultaneously.

3.5.2 Halo Compression and Rotation

Our analysis of the motion of halo stars gives evidence for the first time that the halo may be contracting over a wide distance range. This is likely induced by the dynamical response of the Galaxy to the LMC's infall.This effect is relatively straightforward to understand. The LMC's mass deepens the potential of the MW, and the response of MW halo tracers is a net inward motion as a result of the added mass. Both simulations and data show this effect. This is particularly visible in simulations that model the LMC as a static Plummer potential in PP20, where there is no mass loss from the satellite (see Appendix B.3). A clear compression signal with $\langle v_r \rangle < 0$ can be seen. The amount of mass bound to the LMC at the present-day correlates with the amount of net inward motion

that halo stars experience, and matching $\langle v_r \rangle$ may be crucial for constraining the present-day LMC mass.

Furthermore, a surprising result from the data is the observed halo rotation in the bulk motion parameters, which is non-zero at most radii at the $3-4\sigma$ level. None of the live models had significant measured rotation. Future models may need to include prescriptions for intrinsic rotation in the halo to test whether this can produce the observed signal.

3.5.3 Limitations of the Dipole Model

The dipole model used here to model the mean velocity of the halo as a sum of reflex and bulk motions at various radii is just the first-order expansion beyond the monopole, which studies have predicted or found higher-order signals (Cunningham et al., 2020; Conroy et al., 2021b; Lilleengen et al., 2023). The dipole model could be straightforwardly be extended to quadrupole deformations such as those proposed by (Garavito-Camargo et al., 2019a), and observed by Conroy et al. (2021b). The quadrupole expansion can be defined in a similar manner to the dipole model used here. Higher-order expansions will be necessary for future data releases that will increase the total number of stars in the sample. Additionally, this type of modelling of the velocity field may be a model-agnostic way of approaching substructure in the data (Cunningham et al., 2020).

Future modelling efforts may want to avoid binning. I do not include a prescription for the radial dependence of the parameters in the likelihood. Including this would introduce more fitting parameters, but it would be worth exploring as the number of distant halo stars with known 6D phase-space information increases and the astrometric uncertainties improve. Given the limitations of current data sets, I opted for binning the stars in radial shells. Some non-parametric approaches include the use of splines or other smoothing regressions. A more complex mean halo velocity model (e.g. equation 3.2) that includes a quadrupole term and radial term will increase the number of parameters significantly, which would require more data than what was used in our work. However, I also show that the trends observed in the data are not significantly affected by the choice of bins (see Appendix B.4). The affect of the binning procedure is akin to averaging the assumed continuous distribution in radius of the parameters.

With the current generation of MW-LMC models we are starting to explore the effect of the mass profiles on the reflex motion signature. Future work could probe the amount and nature of the DM particles (GC19), as well as modelling the mass profile and shape of the MW and LMC simultaneously in order to match the observed radial variation of the reflex motion parameters. Here I also use sub-sampling of the DM halo to make tracers of the Galactic potential. Given that the stellar halo is thought to be made of debris from accreted satellites, hierarchical models are needed to determine whether or not a clumpy distribution of halo stars in the integral-of-motion space could affect the reflex motion measured in this work.

Finally, there is without doubt a need to correct for the motion of the disc when studying the kinematic structure of the MW halo. The apparent velocity induced by the motion of the MW disc will affect observations of the velocities of halo stars, most significantly beyond 40 kpc. In particular, more nuanced measurements of the stellar halo ordered motions and anisotropy will be assisted by reflex corrections (e.g. Deason et al., 2017; Bird et al., 2019, 2021; Deason et al., 2021). Figure 3.3 illustrates this by showing the reflex motion signature projected in galactic coordinates in the line-of-sight velocity component. The most significant amount of reflex occurs near the apex and anti-apex locations on the sky in the line-of-sight velocity.

3.6 Conclusions

Using the sample of halo stars, I measured the dipole signal from the motion of halo stars w.r.t the disc. I compare the signal to a suite of LMC-MW models presented here which indicate the origin of the dipole owes to the LMC infall. Following-up on PP21, I compute the reflex motion parameters as a function of Galactocentric distance. Studying the radial dependence of the reflex motion signal enables more detailed comparison to models of the MW-LMC interaction.

The main results are as follows:

1. The measured travel velocity of the disc increases with distance. This agrees with simulations, which predict that the reflex dipole grows with distance and becomes constant at large radii. two distinct behaviours are found. The first is where the response of the halo is adiabatic, reducing significantly the

imprint of the dipole. The second is where the magnitude of disc motion is maximal which is the impulsive regime. Current data suggests that the transition occurs over a wide range of radii, centred at $r \simeq 40$kpc.

2. Information on the previous trajectory of the LMC is encoded in the direction of the reflex motion. I found that at the largest distance, the apex location points to a location on the sky that is roughly aligned with the previous trajectory of the LMC as found in PP21.

3. I find that both the data and simulations show that there is a net inward motion of the halo stars at $r > 30$ kpc (i.e. compression), which may be due to the deposition of the LMC's bound mass to the inner regions of the MW DM halo. Tests using idealised models show that magnitude of the radial component of the halo bulk motion increases depending on the assumed mass of the LMC.

4. By analysing idealised self-consistent models available in the literature (See Table 4.1), I developed a technique to measure the reflex motion parameters ($\vec{v}_{\rm travel}$ and bulk motions) directly from simulations. Using this technique, I compared the reflex motion present in the simulations to the data and arrive at the following conclusions(Figures 3.1 and 3.2). First, in both idealised and self-consistent models, a heavier LMC leads to a larger magnitude of disc motion at all radii. Secondly, none of the simulations reproduce the observed rotation in the halo measured in $\langle v_\phi \rangle$, which suggests that the stellar halo may have had a slight prograde rotation prior to the LMC infall. Third, the profiles of $\vec{v}_{\rm travel}$ with distance vary least in the magnitude and most in the apex locations. These results call for future simulations that model the reflex motion and the bulk velocities of the stellar halo simultaneously.

5. I explored the affect of the data on the fitted parameters by using the idealised simulations to test sky coverage effects, binning choice effects and the signal measured for K giants and BHBs independently. I found that using the SDSS footprint is sufficient for the fit to recover the reflex motion parameters computed directly from simulations. I also found that varying the bin locations does not change the trends observed in the data. I found that the fitting results for K giants and BHBs are consistent at most radii, with exception to the 30-40 kpc bin in the apex latitude.

6. While self-consistent live n-body models are expensive, they are required to

fully model the LMC-MW system and in particular to obtain realistic reflex motion signals. Idealised models must have a responsive MW DM halo at the very least, but can still be useful for discovering dynamical mechanisms.

7. I showed the all-sky line of sight velocity imprint from reflex motion (Figure 3.3), and show that there is a need to correct for the reflex motion of the disc at various radii.

With new large samples of halo stars becoming available in the coming years (e.g. Conroy et al., 2019; Cooper et al., 2023; Kollmeier et al., 2017), more precise measurements of the reflex motion parameters will be available. In tandem, the methodology for measuring the parameters may be improved by first transitioning to a bin-free likelihood, and second including higher-order deformations of the halo. Additionally, future models of the MW-LMC interaction will be beneficial for comparison to the data. As the data improve, future developments may lead to advancements in modelling schemes capable of effectively searching the parameter space of models and orbital histories. Efficient codes for simulating the MW-LMC interaction, such as EXP (Petersen et al., 2022a), are a promising avenue, with the efficiency to produce high fidelity models.

Chapter 4

Dynamical response of the Milky Way to the LMC infall

4.1 Introduction

The presence of the LMC in the MW halo has prompted much research into the dynamical response of the MW halo to the infall of the LMC. Over the past decade, numerical simulations of the LMC's infall have found that the MW disc's barycentre is displaced from the halo barycentre (Gómez et al., 2015a; Petersen & Peñarrubia, 2020b). This displacement occurs in cases where the LMC's mass is $>\sim 10\%$ of the MW's mass. Coupling the aforementioned findings and recent independent measurements place the mass of the LMC at $1.0 - 2.5 \times 10^{11}$ $M_\odot$ (Peñarrubia et al., 2015; Erkal et al., 2019b; Vasiliev et al., 2020; Shipp et al., 2021; Correa Magnus & Vasiliev, 2021; Koposov et al., 2023a; Vasiliev, 2023a). Many signatures of this displacement have been detected in the kinematics of the MW halo stars. Erkal et al. (2021b) find a north-south asymmetry, while Petersen & Peñarrubia (2021b, PP21 hereafter) model the velocity field of the MW halo as a dipole, where the orientation of the dipole points along the past trajectory of the LMC. This disc-displacement induced asymmetry in the outer halo was also measured in recent DESI data (Byström et al., 2024). This displacement leads to a apparent velocity dipole that is observed in the outer halo stars of the MW (Petersen & Peñarrubia, 2021b; Yaaqib et al., 2024b; Byström et al., 2024; Chandra et al., 2024). The detection of this signal calls forth a need for non-equilibrium models of the MW that account dynamical response of the MW

halo the LMC. Lilleengen et al. (2022) show through self-consistent models of the MW-LMC interaction that the LMC induces a strong density dipole in the MW halo that has grown in strength over the last ~ 500 Myr.

To date, few direct links between the reflex motion and the parameters of the pre-infall MW halo (or LMC halo) are known. Only a small fraction of the possible combinations between MW and LMC mass profiles prior to infall have been explored. In PP21, it was demonstrated clearly the relationship between the magnitude of reflex motion and the assumed mass of the LMC (See the Supplementary Data section in PP21). In their experiment, by keeping the LMC on a fixed trajectory and varying the mass, the resulting effect was that the travel velocity of the disc has increased in proportion to the LMC's mass. Hence, their work showed that the reflex speed has strong dependence on the LMC's assumed mass. In an extension to the work in PP21, Yaaqib et al. (2024b, YPP24 hereafter) measured the reflex motion as a function of galactocentric distance in the data and also in a host of literature simulations (See their Table 3.1 for a summary of the simulations analysed). In our work, they show the utility of using the radial variation of reflex motion to compare with reflex parameters computed directly from simulations. While a single measurement of reflex motion against the outer halo shows the dislodging of the MW disc from it's previously shared barycentre with the outer MW halo, it does not provide much constraining power for the profile of the MW. Measuring the radial variation can provide constraints on MW-LMC simulations as different pre-infall mass profiles of the MW will have unique responses to the infall of the LMC, leading to a different reflex motion signature.

The goal of this work is to address how the (observable) reflex motion parameters vary in response to changes in the initial density distribution of the MW DM halo. The reflex motion parameters (magnitude and apex location) as a function of galactocentric distance computed for many simulations in literature varied significantly between the simulations, owing to the differing assumptions about both the MW and LMC pre-infall parameters such as the LMC-MW mass ratio and the scale radii used. Also, simulations in literature used different initial conditions of the LMC, resulting in different trajectories. Since the direction of disc motion w.r.t to the outer halo points at a location along the past trajectory of the LMC, the choice of the LMC initial position and velocity also affects the resulting reflex motion signature. The wide array of choices made for the MW and LMC undoubtedly result in a range of apex locations, magnitudes of the disc

velocity and bulk motions (the collective response of the halo after accounting for reflex). To motivate this paper, we aim to explore the response of the MW stellar halo to the LMC's infall and analyse the resulting reflex motion as a consequence of changes to the initial DM halo profile. To this extent, in this paper we present and analyse a suite of controlled n-body simulations constructed with MW DM halo profiles with a truncation in the density profile. As will be shown in later sections, our simulations cover a wide range of MW-LMC mass profiles (and therefore mass ratios) that help address this.

This paper is structured as follows; in section 4.2 we show the details of the density model used, and summarise the simulation parameters used. In section 4.2.2 we present extended details on the construction of the models in the basis function expansion framework, and discuss the initial condition generation methodology. We also summarise the methodology used to calculate the reflex motion parameters in 4.2.3. In section 4.3 we present the measurements of the reflex motion parameters in all simulations. Section 4.4 discusses the results in the context of the collective response of the halo kinematics. Finally in section 4.5 we conclude the main results and insights of this work.

4.2 Methods

4.2.1 Truncated halo models

To study the MW halo response while varying the profile of the MW, we utilise a modified NFW profile. The truncated NFW profile $\rho(r)$ consists of a piecewise density distribution with a NFW profile up to some radius $r_{\rm b}$, beyond which the profile is power-law truncated as $r^{-\beta}$. The profile is spherically symmetric and due to the inclusion of the outer profile, is finite in mass for values of $\beta > 3$.

$$\rho(r) = \rho_0 \begin{cases} \frac{1}{(\frac{r}{r_s})(1+\frac{r}{r_s})^2}, & r < r_b; \\ \frac{1}{(\frac{r_{\rm b}}{r_s})(1+\frac{r_b}{r_s})^2}(\frac{r}{r_{\rm b}})^{-\beta}, & r > r_{\rm b}. \end{cases} \tag{4.1}$$

Where the prefactor in the $r > r_{\rm b}$ region of the profile is the normalisation to the density such that the density is continuous across the break radius. The prefactor was computed by requiring that the density at the break radius are equal in the

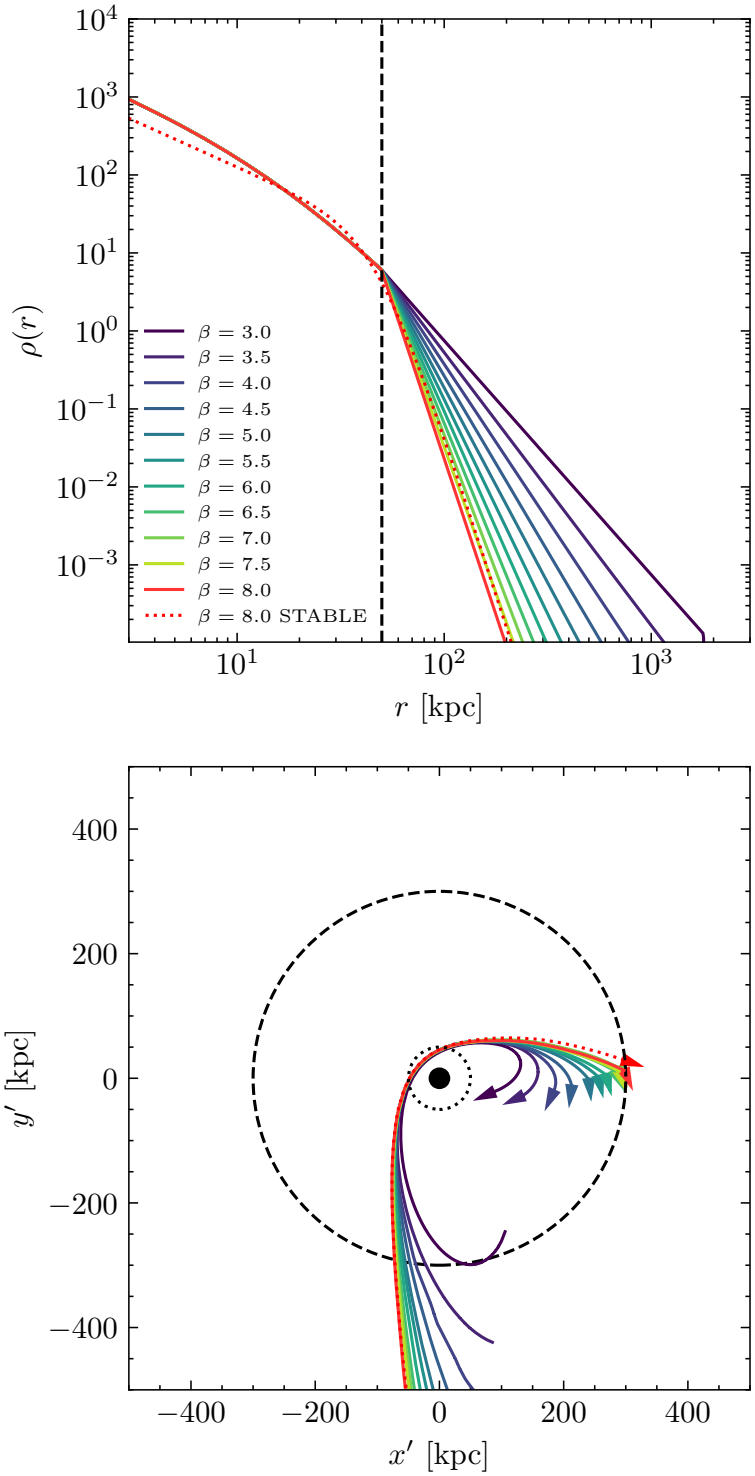

Figure 4.1: *Top Panel:* The truncated NFW profiles of the MW haloes used in this work. The density reported in the figure is in dimensionless units. The most truncated halo has an outer halo of $\beta = 8$ and the no truncation NFW continues across the break with $\beta = 3$. *Bottom Panel:* The trajectories of the softened Plummer sphere LMC haloes from EXP simulations in the orbital plane of the LMC. The black point marks the centre of the MW disc. The black dotted line marks the truncation radius of 50 kpc, and the dashed line marks 300 kpc, which is the virial radius of the $\beta = 3$ model.

Table 4.1: Summary of MW models used in this work.

Simulation Unit	$M_{\rm MW}$ $\times 10^{12} M_\odot$	$M_{\rm LMC}/M_{\rm MW}$	Outer Slope β	$\vec{x}_{\rm LMC\to MW}$ kpc	$\vec{v}_{\rm LMC\to MW}$ kms^{-1}
CU0	1.624	0.095	3.0	$[11.3, 251.0, 108.7]$	$[11.8, 72.7, -23.3]$
CU1	0.952	0.162	3.5	$[34.4, 431.5, 91.2]$	$[3.9, -13.8, -34.8]$
CU2	0.721	0.215	4.0	$[48.2, 526.4, 71.3]$	$[-0.6, -53.2, -34.3]$
CU3	0.604	0.257	4.5	$[58.3, 589.4, 52.0]$	$[-3.8, -73.6, -29.9]$
CU4	0.544	0.285	5.0	$[66.2, 634.8, 34.0]$	$[-5.8, -88.6, -26.4]$
CU5	0.511	0.303	5.5	$[70.6, 660.9, 24.8]$	$[-7.1, -96.9, -24.3]$
CU6	0.487	0.318	6.0	$[75.1, 684.8, 13.3]$	$[-8.3, -104.2, -22.1]$
CU7	0.469	0.330	6.5	$[79.1, 704.7, 2.2]$	$[-9.3, -110.2, -19.9]$
CU8	0.457	0.339	7.0	$[81.5, 717.5, -4.1]$	$[-9.0, -114.0, -18.5]$
CU9	0.448	0.346	7.5	$[83.3, 727.4, -8.9]$	$[-10.4, -116.9, -17.5]$
CU10	0.439	0.353	8.0	$[85.9, 738.9, -16.7]$	$[-11.1, -120.3, -15.9]$
CU10S	0.445	0.337	8.2[a]	$[85.3, 736.5, -15.1]$	$[-10.9, -119.4, -16.2]$

[a]The outer slope of the stable ABG model is slightly larger as we use non-integer values of β when matching the model to the CU10 truncated NFW model.

two regions. The top panel of Figure 4.1 shows the 11 models we use in this work. The models span a range of outer slopes of $3.0 < \beta < 8.0$ with a break radius of $r = 50$ kpc. For models with $\beta = [3.0, 3.5]$ an error function truncation was applied at $r = 600$ kpc to ensure the models are compatible with the simulation software inputs. As can be seen from the figure, all the models share the same density profile interior to the break radius. This behaviour was set by construction to limit our experiment to changes in the outer slope only. The mass interior to the break radius was set to $M = 0.4 \times 10^{12}$ $M_\odot$ for all models, consistent with observations of the MW (McMillan, 2016; Bland-Hawthorn & Gerhard, 2016). The differences in mass arise solely from the outer slope variation. Table 4.1 lists the profile parameters used for all 12 simulations.

While the model is continuous in density, there remains a discontinuity at $r = r_b$ in the derivative. This feature in the profile could lead to the formation of instabilities in the models, when evolved in isolation. In order to facilitate the interpretation of results in later sections in the presence of an instability, we include an additional simulation of the $\beta = 8.0$. The stable simulation is an (α, β, γ) (ABG) profile (Zhao, 1996) with parameters $(3.6, 8.2, 1.2)$ with a scale radius of $r_s = 48$ kpc. The ABG profile is defined as

$$\rho(r) = \rho_0 \left(\frac{r}{r_s}\right)^{-\gamma} \left[1 + \left(\frac{r}{r_s}\right)^{\alpha}\right]^{\frac{\gamma-\beta}{\alpha}} . \tag{4.2}$$

The ABG profile was constructed by simple optimisation of the ABG profile parameters such that they match the $\beta = 8.0$ model. This ABG model also contains the same interior to the break radius as the aforementioned models. This model is a taken to be a stable counterpart of the truncated model, where the stability was checked using Equations 5,6 in Dattathri et al. (2025). The density profile of this model is shown as the dotted line in Figure 4.1. The figure shows small deviations between the ABG and truncated NFW models in the interior regions ($r < 10$ kpc).

4.2.2 Numerical methods

In this section we outline briefly the numerical methods used to generate particles in each simulation and the method of finding the initial conditions of the LMC-MW using reverse-time integration. We also summarise the reflex motion

parameters used throughout the paper.

Simulation initialisations

All simulations and MW disc, halo and LMC halo are modelled using the basis function expansion (BFE) code EXP (Petersen & Weinberg, 2025).[1] For each MW halo model, the model consists of an exponential disc and a truncated NFW halo initially. The disc initialisations are identical in all simulations consisting of 10^6 particles and modelled as an exponential disc. All remaining disc initialisation parameters are kept as the default parameters of the `gendisk` tool provided with EXP. For the MW halos there are 10^7 particles and for a given value of β we tabulate the density, potential and enclosed mass of each model and use `gendisk` for particle initialisation. All the EXP parameters that were used are summarised in Table 4.2.[2]

Satellite initial conditions

The initial conditions of the LMC-MW system are found using the reverse time integration method used in (Vasiliev, 2023b; Vasiliev et al., 2020). The technique evolves the centre of mass motion of the MW-LMC system in an inertial frame via integration of a 12 dimensional system of ordinary differential equations that evolve the phase space of the MW and LMC. During the initial condition finding, the MW and LMC are modelled using rigid non-deforming potentials. For the purposes of our work here, we do not require exact matching between the observed LMC coordinates and simulated ones; therefore this approximate trajectory-finding method provides an efficient and robust initialisation. The present-day snapshot, presented in the remainder of this work, is the one which matches the present-day position and velocity of the LMC measured in Kallivayalil et al. (2013). The snapshot chosen is one in which the (equally weighted) difference in position and velocity between simulation and observation is minimised.

[1] https://github.com/exp-code

[2] Note that only the modified parameters are listed, the remaining parameters use the default parameters present in the software.

Table 4.2: Summary of EXP parameters used in this work.

Parameter	Value	Notes
$N_{\rm halo}$	10^7	-
$N_{\rm disc}$	10^6	-
$M_{\rm LMC}$	1.55×10^{11} $M_\odot$	-
$(l_{\rm max}, n_{\rm max})_{\rm halo}$	(6,20)	Same for all models
$(m_{\rm max}, n_{\rm max})_{\rm disc}$	(4,10)	Same for all models
$t_{\rm rewind}$	4.1 Gyr	-

4.2.3 Reflex motion parameters

'Reflex motion' is defined as the motion of the MW disc w.r.t. to a given shell in the halo.[3] The parameters of the reflex motion are as defined using the dipole model originally presented in PP21. The motion of the disc is defined by the $\vec{v}_{\rm travel}$ which has magnitude $v_{\rm travel}$ and directions $\ell_{\rm apex}, b_{\rm apex}$ defined in the galactic coordinate system. In addition to reflex, the bulk motions are defined as the mean motions in a given shell of the halo *after accounting for reflex motion*. Accounting for reflex motion is critical to separate the measurement of the internal kinematics in the MW halo, and the velocity dipole signal from the motion of the disc. When not accounting for reflex, the dipole signal aliases into the mean motions of the halo. The effects are most significant on the polar and radial velocities.

Since the disc motion is pointed (in general) towards the $b = -90°$ galactic pole, the mean velocity in a given halo shell at larger radii appear to be moving towards the galactic north pole (resulting in negative v_θ). In the mean radial motion, the amount of motion is underestimated when leaving reflex unaccounted for. Where the bulk motion parameters are the mean spherical velocities $(\langle v_r \rangle, \langle v_\phi \rangle, \langle v_\theta \rangle)$ (radial, azimuthal and polar respectively). For observations, these parameters must be fit for in a likelihood based approach (See e.g. PP21, YPP24). However, in simulations they are straightforwardly approximately calculated[4] using the 6D phase space information of halo stars. We refer the interested reader to the measurement technique described in Section 3.3 of YPP24.

[3] Each shell is chosen to be centred on the disc barycentre.

[4] We note here that this is an approximation as ideally the reflex motion model of PP21; YPP24 would need to be fit to fully account for the coupling between the dipole terms and bulk motion terms. Regardless the approximation agreed well with the fitting method as tested in YPP24.

4.3 Results

Figure 4.2 shows the reflex motion at present-day measured in the frame of the disc for all the MW haloes with an increasingly sharper truncation in the outer slope (see Table 4.1). We find that increasing the outer slope of the halo does not change the magnitude of the reflex motion with distance (top panel). Despite the wide range of MW-LMC ratios probed in these simulations ($M_{\rm LMC}/M_{\rm MW} \sim 0.095 - 0.34$) the amplitude of the dipole varies only by about 5 kms^{-1}, with no clear trend with outer slope.

In the apex directions however, a clear trend is observed with increasing outer slope.

In $\ell_{\rm apex}$ all models show a flattening in the function at distances beyond 80 kpc, reaching a value of $\sim 75°$, pointing to the past location of the LMC at $t - t_{\rm peri} = -400$ Myr (See Figure 4.5 for the past trajectory of the LMC in galactic coordinates). At intermediate distances, we recover a trend with increasing outer slope in the models. The apex longitude remains relatively unchanged for models with shallow outer slopes ($4.0 < \beta < 5.0$) remaining at a value of $\sim 75°$ at all radii. However, steeper outer slopes show a dip between $25-50$ kpc, to a minimum value of 20° for the $\beta = 7.5$ model. After which the models assume a rapid rise to $\sim 75°$ by 60 kpc, remaining flat at larger distances and all within 10° degrees. The $\beta = 3.0$ model shows a distinct behaviour in $\ell_{\rm apex}$. It does not contain the dip in $\ell_{\rm apex}$ characteristic of models with higher values of β. It begins at a minimal value of $-5°$ at 20 kpc, then rises rapidly to be in agreement with other models at large radii to a value of $\sim 75°$.

The stable $\beta = 8.0$ ABG model is in good agreement with the truncated NFW counterpart in $v_{\rm travel}$ and $b_{\rm apex}$.

In $b_{\rm apex}$ we find that for models with moderate to large truncations ($\beta > 4.5$), the apex direction with distances goes from being negative between $20 - 40$ kpc then positive between $40 - 60$ kpc around the truncation radius of the haloes before converging to approximately the same value at large radii for the models. At the largest radii, all simulations have similar values of $b_{\rm apex} \simeq -35°$, which is the approximate location of the LMC 400 Myr ago. At intermediate distances (~ 50 kpc), for the simulations with outer slopes between $\beta = 7-8$ values of $b_{\rm apex}$ change from $-40°$ at 20 kpc to $+40°$ at 50 kpc, reaching a peak value of $\sim 50°$.

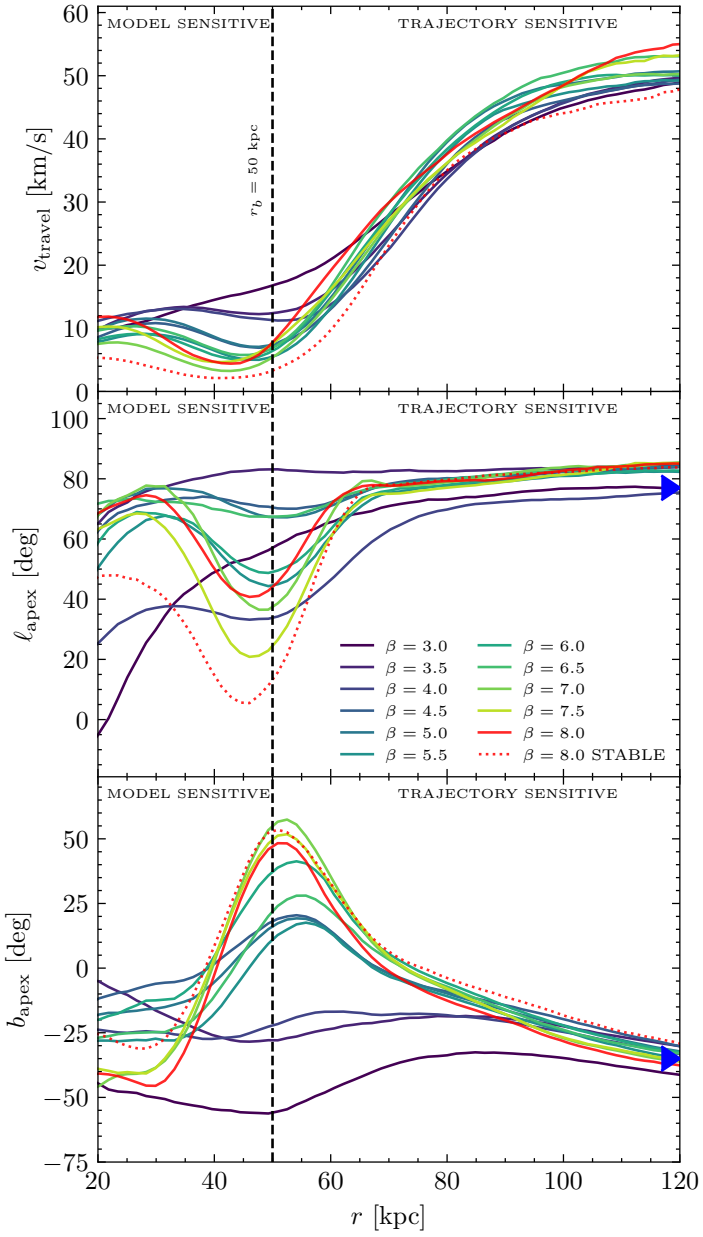

Figure 4.2: Magnitude and direction of the LMC-induced velocity dipole owing to the motion of the disc w.r.t to the outer halo. The reflex motion is calculated for all 11 truncated-NFW models and one stable ABG model used in this work. The inner regions of the halo are where the reflex is sensitive to the model choice (between $0-70$ kpc). While the outer regions are sensitive to the trajectory of the LMC (between $70-120$ kpc) respectively. The blue arrows on the right show the galactic coordinates $l_{\rm LMC}, b_{\rm LMC}$ at $t - t_{\rm peri} = -400$ Myr. The apex locations at large distances are consistent with the past location of the LMC. *Top panel*: In the amplitude of disc motion, no significant differences arise when varying the outer slope; the same trend with galactocentric radius is observed for all models despite the changing (total) mass ratio. The $v_{\rm travel}$ increase remains small within ~ 50 kpc, but then increases almost linearly between $50-100$ before flattening at distances greater than 100 kpc. *Middle panel*: The angle $\ell_{\rm apex}$ as a function of galactocentric radius. *Bottom panel*: The angle $b_{\rm apex}$ as a function of galactocentric radius.

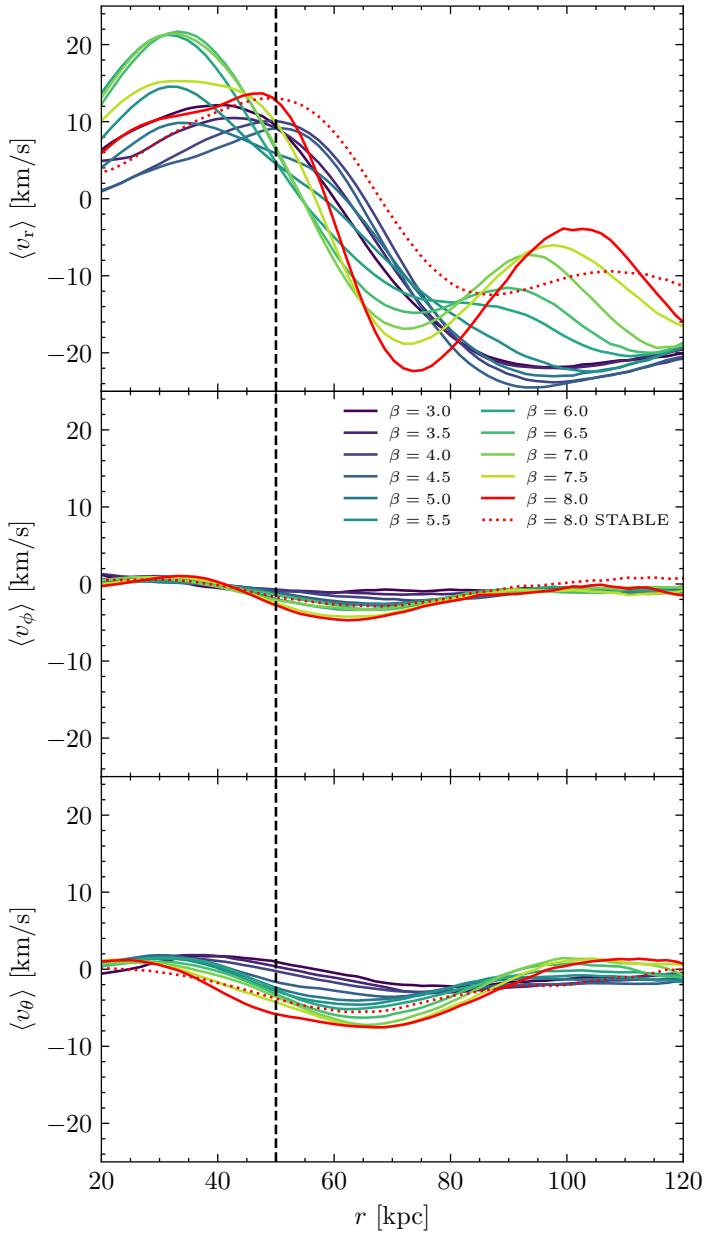

Figure 4.3: The reflex-corrected bulk motions in the MW haloes for each simulation at present day.
Top Panel: The mean radial velocity in shells of width 3kpc between 20 and 120 kpc. All models show a compression signal between $\sim 50 - 100$ kpc. Models with sharper truncations show rebounding radial velocities at larger radii.
Middle Panel: The mean azimuthal velocity of halo stars in all simulations. No significant trends are found with varying β, other than a mildly increasing rotation signal with decreasing outer slope.
Bottom Panel: The mean polar velocity in each shell.

For all models, the peaks occur at roughly the same radius, but with maximum value of $b_{\rm apex}$ decreasing with shallower truncations. The models $\beta = 3.0, 3.5, 4.0$ show little variation of apex latitude with distance.

In the bulk motions we see clear trends in the compression signal $\langle v_r \rangle$ with distance in Figure 4.3. The values of the bulk motions have been corrected for the reflex motion. Reflex motion corrections are needed to account for the aliasing of the velocity dipole signature arising from the motion of the disc, into the mean motions in the halo (discussed further in Section 4.4). In all the models, the onset of compression occurs at$\sim$ 50 kpc with the largest compression values of about -20 kms^{-1}. For the NFW-like truncated model ($\beta = 3.0$) the $\langle v_r \rangle$ shows a very shallow rise to $\sim$ 10kms^{-1} between $20 - 50$ kpc then a steep fall (compression) at larger distances. Despite the lack of truncation for this model, the distance where compression begins is consistent with models with sharper truncations. Hinting that compression starts at the approximate present-day location of the LMC, rather than being tied to the break radius.

All models show a cyclic variation in $\langle v_r \rangle$. The oscillatory behaviour of $\langle v_r \rangle$ with distance is linked to the natural instability of the models (see Section 4.4). More truncated haloes with β between $(5, 8)$ show a bigger rebound of the compression between $80 - 100$ kpc, after reaching their minimal values between $60 - 80$ kpc. Generally models with shallower truncations reach their minimum value of $\langle v_r \rangle$ at larger distances. Interior to the break radius, we find that as the steepness of the outer slope increases, more expansion is experienced by the inner halo, with the trend holding for all values of β except the steepest two models. Finally, we find very small amplitude trends in the bulk rotation and polar motion of the halo stars. In $\langle v_\phi \rangle$ a very mild rotation signal is recovered with the amplitude of the rotation peaking around 60 kpc for all models, whose value increases with the steepness of the outer slope. For the model with $\beta = -8.0$, the measure value of $\langle v_\phi \rangle$ was ~ 5 km s^{-1}.

4.3.1 Basis function expansion coefficient amplitudes

In this section we present the relative amplitude the basis function expansion coefficients used to compute the potential and density of the simulation. The coefficients encode the variations in density and potential, and can be used to diagnose the response of the MW to the LMC – or natural instabilities.

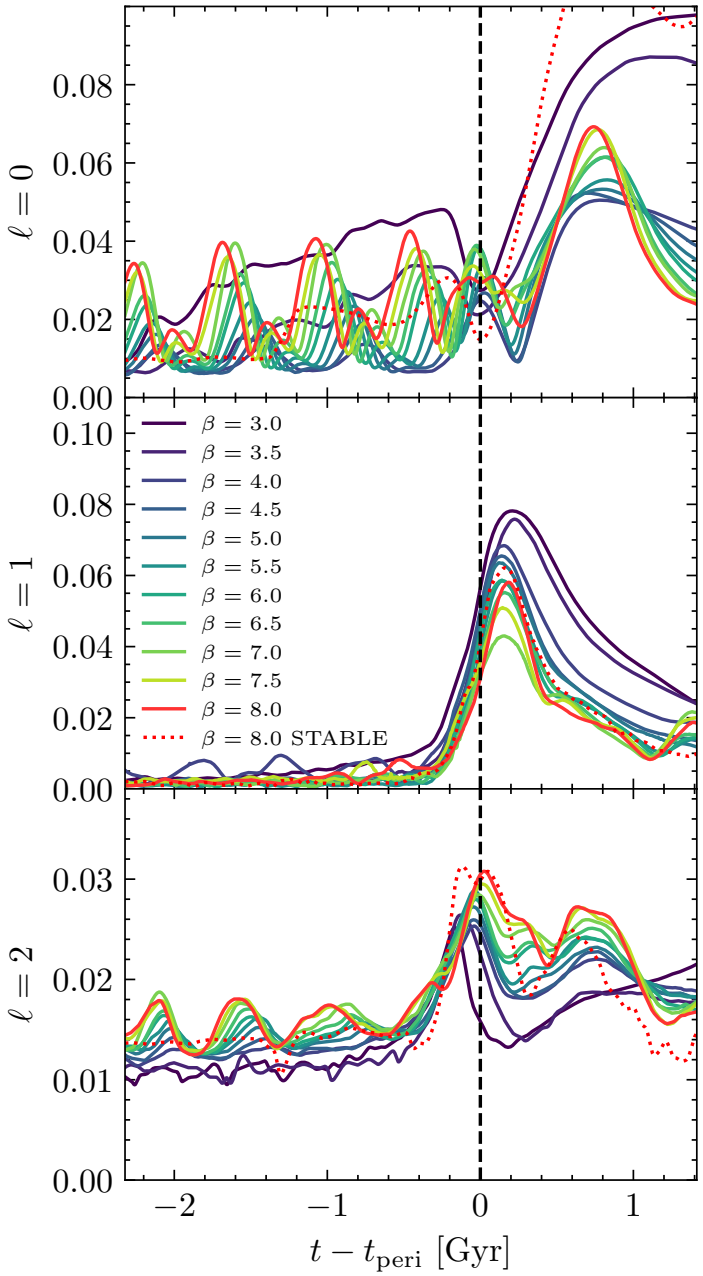

Figure 4.4: The relative amplitude in each of the MW halo basis functions as a function of time for each simulation. The vertical dashed line is set to the present-day time of simulations. The dotted red line shows the relative amplitudes of the stable ABG model of the $\beta = 8.0$ truncated NFW model.
Top Panel: The relative amplitude in the monopole of the basis function expansion coefficients. Oscillations in the monopole amplitude indicate the presence of an instability in the truncated NFW models.
Middle Panel: The relative amplitude in the dipole. The dipole shows little evolution until close to present-day, as the LMC reaches it's pericentre the dipole amplitude increases for all models.
Bottom Panel: The relative amplitude in the quadrupole. Models with truncations $\beta > 4.0$ show mild oscillations prior to the infall of the LMC. Close to present-day the quadrupole amplitude increases for all models.

Figure 4.4 shows the relative amplitude in each of the monopole, dipole and quadrupole for each of the simulations. Interesting trends can be observed for all models. In the case of the monopole, models with truncations of $\beta > 4.0$ show clear oscillations much before the pericentric passage of the LMC. These oscillations are indicative of a radial instability mode and has a period of $\sim$ 0.6 Gyr. The amplitude of the radial oscillations also increases with increasing β. The NFW-like models $\beta = 3.0$ and $\beta = 3.5$ do not show oscillations, rather, the strength in the monopole increases almost linearly for both. At present day, all models have almost equal power in $l = 0$, suggesting the amplitude at present day is tied to the passage of the LMC. Oscillations in the relative amplitude of the monopole and an increasing amplitude with time are key indicators of instability. The stable ABG $\beta = 8.0$ model does not contain an instability: its evolution in $l = 0$ follows that of more stable $\beta = 3.0, 3.5$ models.

For the dipole, there is a clear trend with β that we note here. At present day, as β increases (more truncated) the dipole strength decreases. The peak amplitude in $l = 1$ also follows this trend, where the largest dipole power measured was in $\beta = 3.0$ and the smallest was in $\beta = 7.0$. Furthermore, for the quadrupole, we find an inverse relationship. As β increases, the quadrupolar term also increases in power at present day. We note also that periodic oscillations in $l = 2$ were found for models with truncations in the past ($(t - t_{\rm peri}) < 1$ Gyr), whose amplitude also increase with increasing β. Although these oscillations are smaller in amplitude compared to the monopole. The stable ABG $\beta = 8.0$ shows little evolution in both $l = 1, 2$ prior to passage of the LMC.

4.4 Discussion

Reflex motion is defined as the motion of the disc w.r.t the outer MW halo, where the outer halo in this case is assumed to exist in an inertial frame (Petersen & Peñarrubia, 2020b). The (near-)inertial frame referred to here is due to the very long dynamical timescales of stars in the outer halo. This assumption works well when the dynamical time of stars in the halo are much larger than the infall time of the LMC. In the inner halo of the MW however, the dynamical times are short enough that the assumption of an inertial frame from which a dipole signal is expected does not hold, as the short dynamical timescales of halo stars will also have their own response. When measuring reflex motion with respect to the outermost halo ($r > 50$ kpc), the information in the apex informs the motion

of the disc due to the infall of the LMC in a psuedo-inertial frame. In the inner halo however, the response of the halo itself governs the change in apex location and magnitude with distance. In the following section, we discuss the physical response revealed by measuring the reflex motion signature in the inner halo of the MW.

4.4.1 Reflex Motion of the MW disc

The top panel of Figure 4.2 shows the magnitude of the disc velocity as a function of distance. Surprisingly, it shows little variation across the models, despite a wide coverage of MW-LMC mass ratios $0.09 < M_{\rm LMC}/M_{\rm MW} < 0.34$. While previous works have shown that the reflex signature is sensitive to the mass ratio with fixed MW mass (see, e.g., Garavito-Camargo et al. 2019b, PP21, YPP24), our simulations show that the MW's mass does not change the amplitude of reflex motion significantly. This suggests that it is more difficult to determine the MW-LMC mass ratio compared to the mass of the LMC only from the reflex motion. It also indicates that the LMC's mass is the main contributor to the magnitude of velocity dipole

The middle and lower panels of Figure 4.2 show the variation in the apex directions with the different MW haloes. Here we notice a surprisingly large variation between the models, especially in $b_{\rm apex}$. At large distances of $r >$ 100 kpc the dipole direction is consistent among the models, and points to a location along the past trajectory of the LMC,[5] as previously found by PP21 and YPP24.

Figure 4.5 shows the location of the LMC in galactic longitude and latitude with time. When compared against the apex locations at large radii (at present day), all models point at a past location of the LMC, no model points towards the present day location. From Figure 4.5, at $t - t_{\rm peri} = -350$ Myr the LMC location was $\ell_{\rm LMC,past} \approx 75°, b_{\rm LMC,past} \approx -40°$ for all models.[6] This is fully consistent with the convergent values of the apex locations at large radii in Figure 4.2. The pointing of the apex locations is consistent with the interpretation of the apex

[5]Within ~ 300 kpc all models have very similar trajectories (c.f. Figure 4.1, at even smaller radii the difference in trajectories diminishes further. Since the disc's response to the LMC is strongest close to the pericentre, big differences in the apex directions at large radii are not expected.

[6]A variation in $b_{\rm LMC,t=-350}$ of ~ 5° is present owing to the slightly different trajectories of each simulation.

location at large distances presented in PP21; YPP24.

From a dynamical standpoint, the location of the apex measured at present points at a past location of the LMC (e.g. where the LMC was $\approx 300 - 500$Myr ago, of order mean dynamical timescale of the MW disc) because the displacement of the MW disc is not instantaneous, rather it happens over timescales related to the average dynamical timescales of disc stars (or the inner halo in general). Measurements of apex locations that place the direction of disc motion pointed towards the present-day location of the LMC cannot be explained by our simulations.

Furthermore, variations in the directions in the inner halo are governed by the dynamical response of the halo to the LMC's infall, which in turn affects the relative motion between the inner halo and disc. Generally, as β increases, the direction of $b_{\rm apex}$ with radius goes from being negative at $r < 40$ kpc, then increases to a maximal value that is positive near the truncation radius where the peak value in $b_{\rm apex}$ increases with increasing β, then becomes negative again in the outer halo. This behaviour can be attributed to how the motion of the barycentres of the MW disc and halo move in each model.

For the most NFW-like models, the inner halo's barycentre is supported by the mass beyond the truncation radius, which impedes the barycentric motion in the inner halo induced by the LMC. In this scenario, the reflex motion signal is driven mostly by the barycentric motion of the MW disc, which leads to little change in the apex locations.

However, when truncating the halo, the barycentre of the inner halo can be moved more easily by the LMC. The motion of the inner halo in this regime is now significant, and crucially misaligned with the barycentric motion of the disc, owing to the difference in orbital timescales between halo and disc stars. This motion results in a abrupt change in measured reflex motion, this is seen in the apex directions in Figure 4.2.

4.4.2 Bulk motion of the stellar halo

As done in PP21 and YPP24, we measure the *reflex corrected* bulk motions in spherical shells about the disc barycentre at present-day in the simulations (See Figure 4.3). We emphasise the importance of this correction, noting that if the

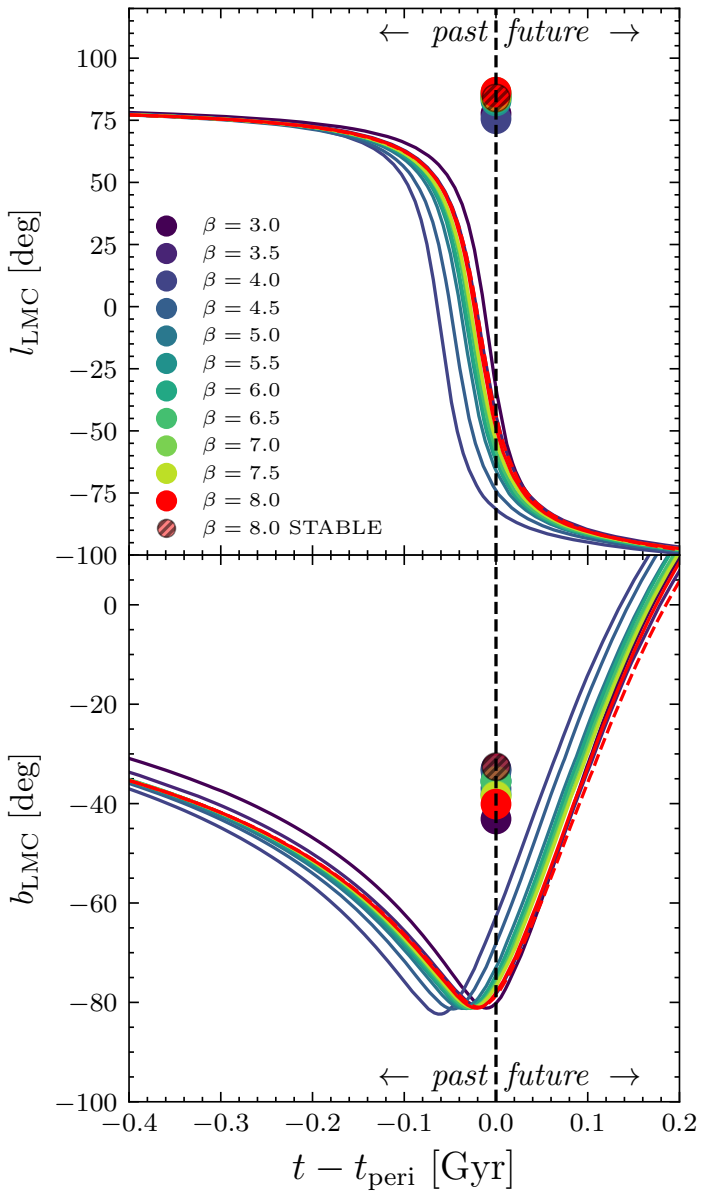

Figure 4.5: This Figure shows the past trajectory of the LMC in galactic coordinates (l, b) (lines) and the apex locations $(\ell_{\rm apex}, b_{\rm apex})$ calculated at present day against all stars with $r > 100$ kpc (points). This Figure illustrates our findings that the present-day apex points at the past location of the LMC. The present-day apex is consistent with the location of the LMC at $t - t_{\rm peri} \approx -350$ Myr.

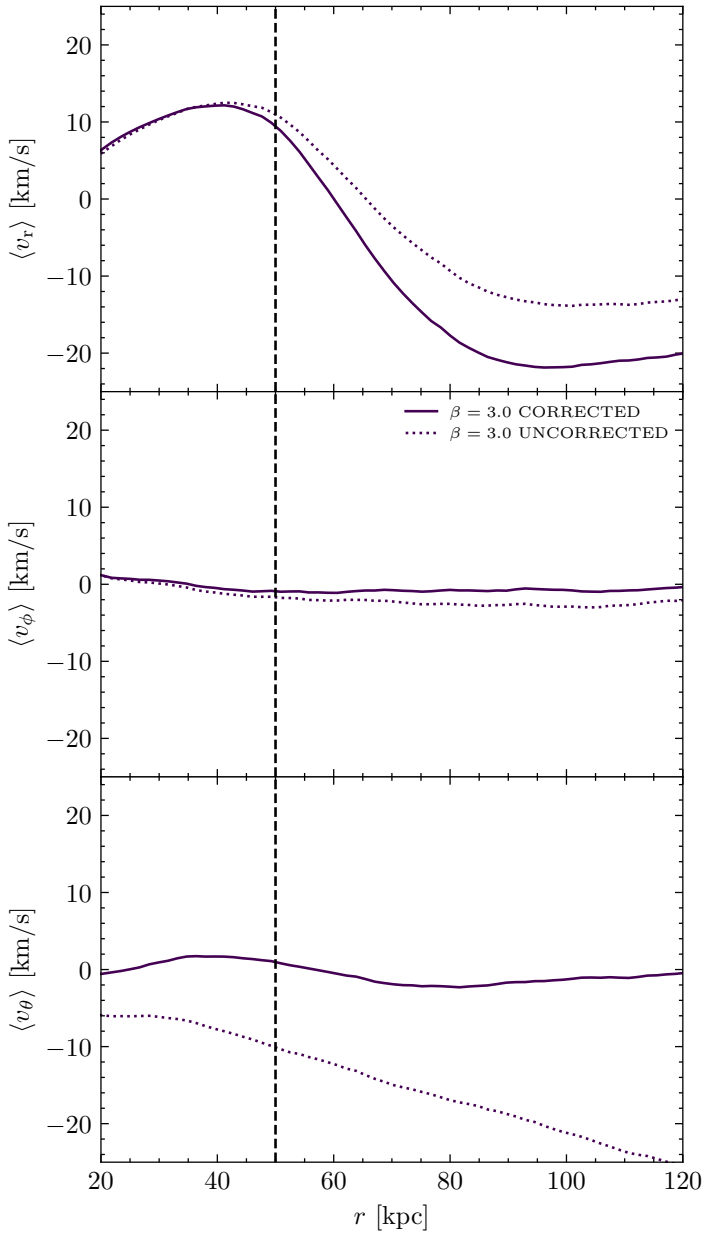

Figure 4.6: This Figure shows the same information as figure 4.3, but highlighting the difference in the bulk motions when reflex motion is left unaccounted for in the $\beta = 3.0$ model. The dotted line shows the uncorrected bulk motion signal, while the solid line shows the reflex correction signature.

reflex is not accounted for, the velocity dipole signal is imprinted also in the bulk motions.

To highlight this issue, Figure 4.6 shows the resulting bulk motions of the $\beta = 3.0$ models in the case of accounting and not accounting for the reflex motion of the MW disc. In the case where reflex motion is unaccounted for, the velocity dipole signature imprints strongly on $\langle v_\theta \rangle$, causing the polar velocity to be an decreasing function of distance. Furthermore, it affects also the compression velocity by decreasing the magnitude of the signal at large radii. The biases in $\langle v_r \rangle$ and $\langle v_\phi \rangle$ arise because the disc (our observing frame) is displaced from the halo barycentre by a few kpc due to reflex motion. When averaging halo star velocities over spherical shells in the disc frame, we sample the halo's density distribution asymmetrically. This non-uniform sampling produces biased bulk motions. Note that the dipole itself averages to zero when centred on the halo barycentre (i.e. when the shells are of uniform density). Correcting for reflex motion aids in eliminating this geometric bias. Also, accounting for reflex motion results in an easier interpretation of the signals - they are the kinematic response in the halo to the infall of the LMC. In YPP24, the variation in the bulk motion was attributed to the presence of the bound mass of the LMC at present day, the amount of compression in the radial velocity increased with increasing LMC mass (see Figure 3.2).

In the top panel of Figure 4.3, we present the bulk motion signatures measured in each of the models shown in table 4.1. For all models, the compression signature is clear – beyond the break radius, the mean velocity in a given halo shell decreases with distance. However, a striking feature in our analysis shows that not only is the compression velocity present, but sinusoidal variations in $\langle v_r \rangle$ are also found. This variation occurs as truncating the MW halo induces a radial instability of breathing mode type in the halo. This is corroborated by the amplitude of $l = 0$ in the basis functions for the models with modest to steep truncations in Figure 4.4. Weinberg (2023) find that a truncation to the density profile between $1-2$ viral radii causes an inflection in the distribution function (a range of E where $df/dE > 0$) that seeds an $l = 1$ instability in the halo (See also Dattathri et al. 2025). Importantly, we find that when accounting for reflex motion, signatures of instability in the halo could be detected in the bulk motions. The in the outer halo, the compression velocities rebound after reaching their minima. The rebounding $\langle v_r \rangle$ shows larger peaks with increasing β as the amplitude of the pre-existing breathing mode is larger for more truncated haloes. Furthermore,

to verify that the oscillations in $\langle v_r \rangle$ are due to instability, we show in Figure 4.3 a stable ABG model that approximates the $\beta = 8.0$ truncated model. The bulk radial motion for this model shows almost no oscillations in $\langle v_r \rangle$, it almost constant after reaching it's minimum value. The stable ABG model also shows a stable evolution in the amplitudes of the basis functions in Figure 4.4.

In the bulk rotations ($\langle v_\phi \rangle$) of the haloes, we measure a weak signal. While this signal is small, the radius at which $\langle v_\phi \rangle$ reaches its maximum amplitude is close to the present-day position of the LMC – hinting that this is likely a local effect induced by the LMC. In PP21 and YPP24, a prograde rotation signal of the order 40 kms^{-1} was detected in the data. In those works, the rotation was attributed to primordial rotation, as the bulk motions they measure for a multitude of literature models do not have significant rotation. We arrive here at the same conclusions. Despite multiple detections of bulk rotation in the halo (Iorio & Belokurov, 2021), the LMC-MW interaction in simulations does not induce any significant bulk rotation in the MW halo.

Finally, in the bottom panel of Figure 4.3 we see a systematic trend in the polar motions of stars in the halo. All models have a mildly decreasing trend of $\langle v_\theta \rangle$ between $\sim$ 20 kpc and $\sim$ 60 kpc that gradually returns to zero beyond $\sim$ 60 kpc. The steeper the outer halo, bigger the amplitude of v_θ found. Negative polar motion indicates that stars on average have mild motion towards the north pole of the MW. Additionally, local effects[7] could amplify the measured polar velocity signal. The breadth of the $\langle v_\theta \rangle$ signal in radius suggests that it could be a combination of local and global responses to the LMC.

4.4.3 Interpreting the reflex signals

We can connect the choices made for the halo profile with resulting reflex motion measured. In Figure 4.2 in the apex directions, there are two clear regimes. In the outer halo, at distances > 100 kpc all the simulations point at a location along the past trajectory of the LMC. As discussed in PP21 and YPP24, this is due to the long dynamical timescales of stars in the outer halo, where the infall of the LMC proceeds much faster than the stars are able to respond. However, at intermediate distances, clear trends can be seen in b_{apex} and ℓ_{apex}. In all

[7]Local effects here refers to the fact that stars within close proximity to the LMC (e.g. within the tidal radius) will be responding to the presence of the satellite at close proximity, rather than participating in the collective response of the MW halo.

the simulations we run, the profiles interior to 50 kpc are identical, therefore what drives these variations at intermediate radii are the differences in the profile beyond the break radius. For the NFW halo ($\beta = 3.0$) much of the mass exists in the outskirts. In this case, the inner halo can be supported gravitationally by the mass exterior to it. Therefore, during the infall of the LMC close to pericentre, the inner halo is resistant to displacement from it's original barycentre. In the reflex motion signature, for the $\beta = 3.0, 3.5$ models, we see this effect arising as smooth and small variations (respectively) in the apex directions with distance across intermediate and large distances.

In the case where the mass in the outskirts is removed, then the inner halo becomes more susceptible to displacement from the LMC, although the larger dynamical timescales (relative to disc stars) means that the motion of the halo will be misaligned with the motion of the disc. These two effects lead to measuring large variations at intermediate distances. To further delve deeper into the interplay between observed reflex and the halo, we notice that for the NFW halo($\beta = 3.0$), the dipole strength is the largest while the quadrupole strength is the smallest. Also, the NFW (and $\beta = 3.5$) models have little variation in the apex directions. while the $\beta = 8.0$ has the opposite - small dipole and largest quadrupole at present day and a large variation in the apex direction at intermediate distances. This hints that the amount of variation in the apex locations at intermediate distances are driven by the strength of the dipole and quadrupolar deformations.

More truncated haloes experience larger quadrupolar deformations, and are more susceptible to the influence of the LMC owing to the lack of material outwith the break radius. To further investigate this, we utilise EXP to perform additional simulations of the truncated NFW $\beta = 8.0$ model, where the deformation types are restricted to having only a monopole, a monopole and dipole and a monopole, dipole and quadrupole. Figure C.1 shows that for a MW halo that can only deform with $l = 0$, the apex locations at intermediate radii are relatively unchanged. When allowing $l = 1$, $\ell_{\rm apex}$ shows a dip at ~ 50 kpc and a steep rise in $b_{\rm apex}$. Further allowing the quadrupole term to contribute to the basis, $\ell_{\rm apex}$ varies more significantly at 50 kpc. This simple test shows that the variation in $b_{\rm apex}$ is driven by the presence of *both* a monopole and a dipole, while the presence of the quadrupole enhances only the apex longitude.

4.5 Conclusions

In this work, we presented a suite of MW-LMC simulations varying the outer slope of the MW halos between $3.0 < \beta < 8.0$. We self-consistently simulated the infall of the LMC and extracted for each simulation the reflex motion parameters $v_{\rm travel}, \ell_{\rm apex}, b_{\rm apex}, \langle v_r \rangle, \langle v_\phi \rangle, \langle v_\theta \rangle$ as a function of distance at present day. We also show the deformations experienced in each simulation through the amplitude of basis function coefficients as a function of time for the monopole, dipole and quadrupolar deformations. We summarise our findings as follows:

1. At fixed LMC mass, the amplitude of reflex motion $v_{\rm travel}$ does not vary significantly for a wide range of MW-LMC mass ratios of $0.1 < M_{\rm LMC}/M_{\rm MW} < 0.35$. Our results imply that $v_{\rm travel}$ depends on the assumed mass of the LMC, rather than the mass ratio of the MW-LMC system. This result cautions against our ability to constrain the MW-LMC mass ratio through the detection of the velocity dipole.

2. The direction of the velocity dipole at intermediate radii between $30-60$ kpc can vary based on the *outer* MW halo profile. Our results show that (a) steeper truncations to the outer MW halo produce more strongly varying apex directions (b) the apex locations when measured against the outer halo is not sensitive to the outer MW halo profile, but to the trajectory of LMC. We interpret this result as the inner halos of more steeply truncated models are less supported by the mass in the outskirts. Therefore without mass in the outskirts, the inner halo responds more strongly to the LMC's infall, although not with the same timescales as the disc. This leads to a stronger misalignment between the motion of the disc and inner halo, and therefore a larger variation in the apex locations.

3. We show also explicitly that large deviations in the apex locations at intermediate radii are caused by the dipolar and quadrupolar deformations to the halo, through simulations that restrict the type of deformations allowed in the halo (See Appendix C.1).

4. In the compression velocity of the halo, we show that all MW models show a clear compression signal, but the maximal compression experienced by the models is strongest for the shallow truncations and weakest for more truncated halos.

5. We discover a radial (breathing mode) instability in truncated MW halos that forms as a result of the model truncation. We find that the amplitude of the oscillations increases with increasing outer slope. We find that this instability presents in the compression velocity $\langle v_r \rangle$ as oscillations that vary with distance.

We conclude with the following remarks. The reflex motion signature holds information on the outer profile of the MW through the response of the inner halo itself to the presence (or absence) of an extended halo. While no empirical relation between the outer halo slope and reflex motion parameters was uncovered, our experiment shed light on the dynamical relations between the inner halo, outer halo and MW disc to the infall of the LMC.

Furthermore, through analysis of the basis function expansion coefficients in time, we show that in order to measure a $\vec{v}_{\rm travel}$ that varies in direction at intermediate radii, the MW halo must deform with at least $l = 1$, and in order to measure compression in $\langle v_r \rangle$ an $l = 0$ deformation is needed. Both the apex directions and compression have been measured to be radially varying in the literature.

Future work could see a more complex reflex motion model that accounts for cyclic variations in the compression velocity, to test whether a radial instability exists in the MW halo. Additionally, further testing with a different family of models (e.g. using stable ABG models varying only the transition α) could provide important insights about the pre-LMC infall shape of the MW halo.

Chapter 5

Conclusion

In this thesis, I explored the effects of satellites on different scales in the MW. In Chapter 2, I presented a new method to describe the formation and evolution of the phase spiral in angular momentum. By modelling path of stars in cylindrical AM, I presented a likelihood-based approach to model the phase spiral. I showed through the model that a 'chi-by-eye' fit to the data can recover the winding and amplitude we observe in the data. I presented the insights gained from this modelling approach - the vertical potential of the MW is covariant with the timing of the perturbation, as the profile vertical potential will either speed up or slow down the winding of the spiral. I show also that modelling the spiral in AM, the radial and vertical oscillations are coupled. Finally, the likelihood model for the spiral can be adapted to many types of perturbations - I showed case of a tilting perturbation and also a kick perturbation.

In Chapter 3, I measured the radial variation of the reflex motion of the MW disc caused by the infall of the LMC in the data. I found that in the travel velocity of the disc there are two regimes i) The adiabatic regime, where the response of the halo is adiabatic, resulting in small relative motion between the LMC and MW inner halo ii) The impulsive regime, where the disc travel is maximal when measuring against the outermost halo stars. In the latter case the motion of the disc appears impulsive to outer halo stars owing to the very large dynamical timescales at those distances. Furthermore, I detected in the data a net inward motion of the halo stars (after accounting for reflex motion) in the MW that increases as a function of galactocentric distance. I found this compression to be a consequence of the mass the LMC deposits in the inner MW. I

verify this by showing that in simulations with increasing LMC mass, the amount of compression also increases. I discover in the data also a net prograde rotation in the halo, which were not explained by any LMC-MW simulation we analyse, hinting at primordial rotation in the MW halo. To provide a more complete interpretation of the reflex motion signal, I also show in the Appendix the effects of sky coverage on the measured reflex motion through simulations. I also test different halo tracers and verify that the results are consistent between them.

The work of chapter 3 highlights the host of effects the LMC causes in the MW. I also stress the need to correct for reflex motion when studying the kinematics of the MW halo stars, and provide the code required to perform corrections to kinematics. The reflex motion signature in Chapter 3 for nine simulations from the literature show large variations in the reflex motion signature, mostly in the travel velocity and apex directions. As each simulation differs in the pre-infall parameters for the MW and LMC (e.g. MW mass, halo concentration, LMC mass), the resulting reflex signatures are all different. The natural question arising from this analysis was - *How do the pre-infall parameters of the MW (and LMC) affect the reflex motion we measure at present day?* This was the motivation for Chapter 4.

In Chapter 4, I simulate the MW-LMC interaction in a controlled setting for a family of truncated NFW models, while keeping the mass of the LMC fixed. The models vary only in the outer slope of the MW, controlled by the β parameter while the MW halo profiles are all truncated at 50 kpc. For a range of outer slopes between $3.0 < \beta < 8.0$ the LMC-MW mass ratios vary from ($\frac{M_{\rm LMC}}{M_{\rm MW}} \sim 0.095-0.34$).

My main findings are as follows i) Despite a wide range of mass ratios, the travel velocity of the disc does not vary significantly between the models, supporting the idea that the travel velocity is driven strongly by the mass of the LMC prior to infall. This is also supported in Chapter 3, where with simulations increasingly large LMC mass produce significantly larger travel velocities in the disc. ii) The apex locations as a function of galactocentric distance vary systematically with the slope of the *outer* halo at intermediate radii, while at large radii they point at similar locations on the sky (close to a point on the past trajectory of the LMC). This indicates that at large radii, the direction of reflex motion is most sensitive to the LMC trajectory, while at intermediate radii, it is driven by the differential response of the MW halo that is set by the pre-infall density function.

I measure quantitatively through the BFE coefficients the relative amplitudes of

the monopole, dipole and quadrupole deformations in each simulation with time. I show that the change in apex locations is driven by the dipole and quadrupole deformations (See Appendix A.7 also). I discover here also a radial instability in the truncated NFW models, which arise due to the discontinuity in the derivative of the density profile, that seeds a feature in the distribution function of these models that grows into an instability. I showed that an instability of this type will be present in the $\langle v_r \rangle$ parameter of the reflex motion model, and imparts sinusoidal variation on top of the compression signal.

In conclusion, satellites in the MW affect the galaxy in a host of different ways and on large and small distance scales. At smaller scales, within the galactic disc there are clear signatures of phase mixing present in radial and vertical kinematics. At the largest scales, the LMC has displaced the barycentre of the disc relative to the outer halo and likely deposited a significant amount of it's halo already into the MW halo. The MW halo responds in density through the formation of monopole, dipole and quadrupole deformations. The LMC also affects other satellites in the MW, where their orbits will be affected by the infall of the LMC. The LMC also affects the observed kinematics of halo stars through reflex motion, which can be corrected for by measuring reflex motion in the MW.

At all these scales, the assumption of equilibrium is not favourable if the goal is to interpret features observed in MW data. My work in this thesis covered only a small part of disequilibrium features observed in MW data, and is no way all encompassing. The goal of all the work presented was not to find models or methods that are exact matches to the data. Rather, it was to build intuition on the dynamics so that the interpretation of the data is not biased by what is *expected* to happen. I have learned throughout this PhD, that it is better to start a project with a well-posed question, rather than to start from the data and work back to the question. The former builds intuition in a pedagogical manner, while the latter is easily susceptible to being corrupted by a desire to find or construct methods that matches the data, and leave the interpretation of the dynamics as a final step.

Chapter 6

Future work

In Chapter 2, the model I develop and test alongside the data shows promise as a way to perform likelihood-based fitting on the AM of stars in *Gaia*. Two avenues of further developing this work are as follows. Firstly, fitting the AM of of stars in *Gaia* with the tilt model and finding the best fit values of the tilt angle, line of nodes, time of tilting and the dispersion of the AM space prior to the tilt. I could also leave parameters of the MW disc model free such as the scale height, scale radius and mass as part of the fitting. The fitting will no doubt come at a large computational cost, as the dataset is comprised of $\approx 11,000,000$ stars. Secondly, the tilt (and kick) models are relatively simple implementations of disc perturbations. Further theoretical development on the modelling of how satellites (such as Sgr) perturb the disc stars' AM would be needed if the aim was to fold properties of the perturber into the modelling as well.

In Chapter 3, the paucity of the data at large radii leaves space to repeat the measurements of the reflex motion parameters with larger datasets extending the signal to the impulsive regime in the MW halo and decreasing the size of uncertainties on fitted parameters. Furthermore, the reflex motion model, comprised of a velocity dipole and bulk motions was fit binning the data in distance. A more robust approach would be adding a radial parametrisation to the model.

As we see in Chapter 4, the interplay between reflex motion and pre-infall parameters of the MW and the LMC is not trivial and a radial parametrisation grounded in dynamical arguments would be helped significantly by additional controlled simulations of the MW-LMC interaction, and therefore observing the

resulting reflex motion. Another extension to this work would be testing a family of stable ABG models varying the scale radius and the ABG parameters (α, β, γ). A grid of simulations that cover this parameter space may shed light which part of the assumed MW halo profile matters most for controlling the apex locations at intermediate radii. For example, is the transition between inner and outer halo (α parameter) impactful on reflex?

The works presented in my thesis here only begin to scratch the surface of what are multi-faced problems covering LMC-MW simulations, data interpretation of disequilibrium features, modelling phase mixing in the disc. There is indeed much work left to do in uncovering the current dynamical state of the MW, which will aid in understanding the history of the MW and its evolution through cosmic time.

Appendix A

Appendix A

A.1 Gaia query of dataset

The full RVS catalogue used in the paper was queried from the *Gaia* archive using the query below:

```
SELECT
    source_id,
    ra,dec,
    pmra, pmra_error,
    pmdec, pmdec_error,
    pmra_pmdec_corr,
    parallax,parallax_error,
    radial_velocity, radial_velocity_error
FROM
    gaiadr3.gaia_source
WHERE
    ruwe < 1.4
    AND radial_velocity IS NOT NULL
    AND parallax_over_error > 5
```

A.2 Modelling the spiral with a kick

In this Appendix we describe a velocity-kick perturbation model, in contrast to the tilt model presented in Section 2.4.3. We describe the resulting angular momentum distribution in L_R, L'_φ, resulting from a velocity kick to the disc.

We assume the perturbation has taken the form of a 'kick' of magnitude δ_v in vertical velocity v_z, so that for any given star, only L_φ is affected (c.f. Eq. 2.1). Assuming all stars are on circular orbits at $R = R_g$ (with R_g itself a function of L_z), the change in L_φ is $\delta L_\varphi = -R_g \delta_v$. We further assume that this perturbation applies instantaneously at time $t_{\rm kick}$ to all stars within an azimuthal 'wedge' centred on $\varphi_{\rm kick}$ with full-width $\Delta\varphi$. As in the main text, we take $t = 0$ for the present day, so that $t_{\rm kick}$ is negative.

Our model thus has a parameter set θ comprising 5 free parameters: $\theta = \{\sigma_L, \delta_v, t_{\rm kick}, \varphi_{\rm kick}, \Delta\varphi\}$. For an individual observed star, the likelihood of its observed L_R^0, L'^0_φ (the 0 superscripts here indicating the observed values at the present day) is

$$\begin{aligned} \ln l(\theta) &\equiv \ln p(L_R^0, L'^0_\varphi | L_z, \varphi, \theta) \\ &= -\frac{1}{2\sigma_L^2}\left({L_R^{t_{\rm kick}}}^2 + (L'^{t_{\rm kick}}_\varphi - \mu_L)^2 \right) - \ln(2\pi\sigma_L^2), \end{aligned} \tag{A.1}$$

where

$$\begin{aligned} L_R^0 &= L_R^{t_{\rm kick}} \cos(\Omega_z t_{\rm kick}) + L'^{t_{\rm kick}}_\varphi \sin(\Omega_z t_{\rm kick}); \\ L'^0_\varphi &= -L_R^{t_{\rm kick}} \sin(\Omega_z t_{\rm kick}) + L'^{t_{\rm kick}}_\varphi \cos(\Omega_z t_{\rm kick}), \end{aligned} \tag{A.2}$$

and

$$\mu_L = \begin{cases} -\frac{\Omega_\varphi}{\Omega_z} R_g \delta_v, & \text{if } |\varphi - \Omega_\varphi t_{\rm kick} - \varphi_{\rm kick}| \mod 2\pi < \Delta\varphi/2; \\ 0, & \text{otherwise.} \end{cases} \tag{A.3}$$

Figure A.1 shows the relative angular momentum density in the kick model in the MWpot model used in Section 2.5.1, as well as the same variations to the time since perturbation and potential as made in the main text. Here the chosen model parameters were $\sigma_L = 110 \mathrm{km\,s^{-1}kpc}, \delta_v = 14 \mathrm{km\,s^{-1}}, \varphi_{\rm kick} = 0°, \Delta\varphi = 280°$, for t_{kick} we choose a time of −0.6 Gyr (first column in Figure) and −0.9 Gyr (second column).

The choice of a large $\Delta\varphi$ here was made as smaller (i.e. $\Delta\varphi < 180°$) angles lead to the spiral appearing in half the L_z bin, the appearance (and disappearance) of the spiral in any individual bin depends strongly on this parameter. We arrive at the same conclusions that were made for the global tilt model we presented in the main text. One difference in this kick model is that when observing the stars in a single azimuthal bin, the amplitude of the spiral feature varies much more drastically from one L_z bin to another. This is a consequence of the more localised nature of the initial perturbation.

A.3 Derivation of Cylindrical Angular Momentum Components

In this appendix, I derive the cylindrical angular momentum components used in Chapter 2 by projecting Cartesian angular momentum components onto the cylindrical basis.

The Cartesian angular momentum vector is defined as

$$\mathbf{L} = \mathbf{r} \times \mathbf{v}, \tag{A.4}$$

which in Cartesian coordinates gives

$$\begin{aligned} L_x &= yv_z - zv_y; \\ L_y &= zv_x - xv_z; \\ L_z &= xv_y - yv_x. \end{aligned} \tag{A.5}$$

The transformations between Cartesian and cylindrical coordinates (R, ϕ, z) are

$$\begin{aligned} x &= R\cos\phi; \\ y &= R\sin\phi; \\ z &= z. \end{aligned} \tag{A.6}$$

The velocities are transformed via

$$\begin{aligned} v_x &= v_R\cos\phi - v_\phi\sin\phi; \\ v_y &= v_R\sin\phi + v_\phi\cos\phi; \\ v_z &= v_z, \end{aligned} \tag{A.7}$$

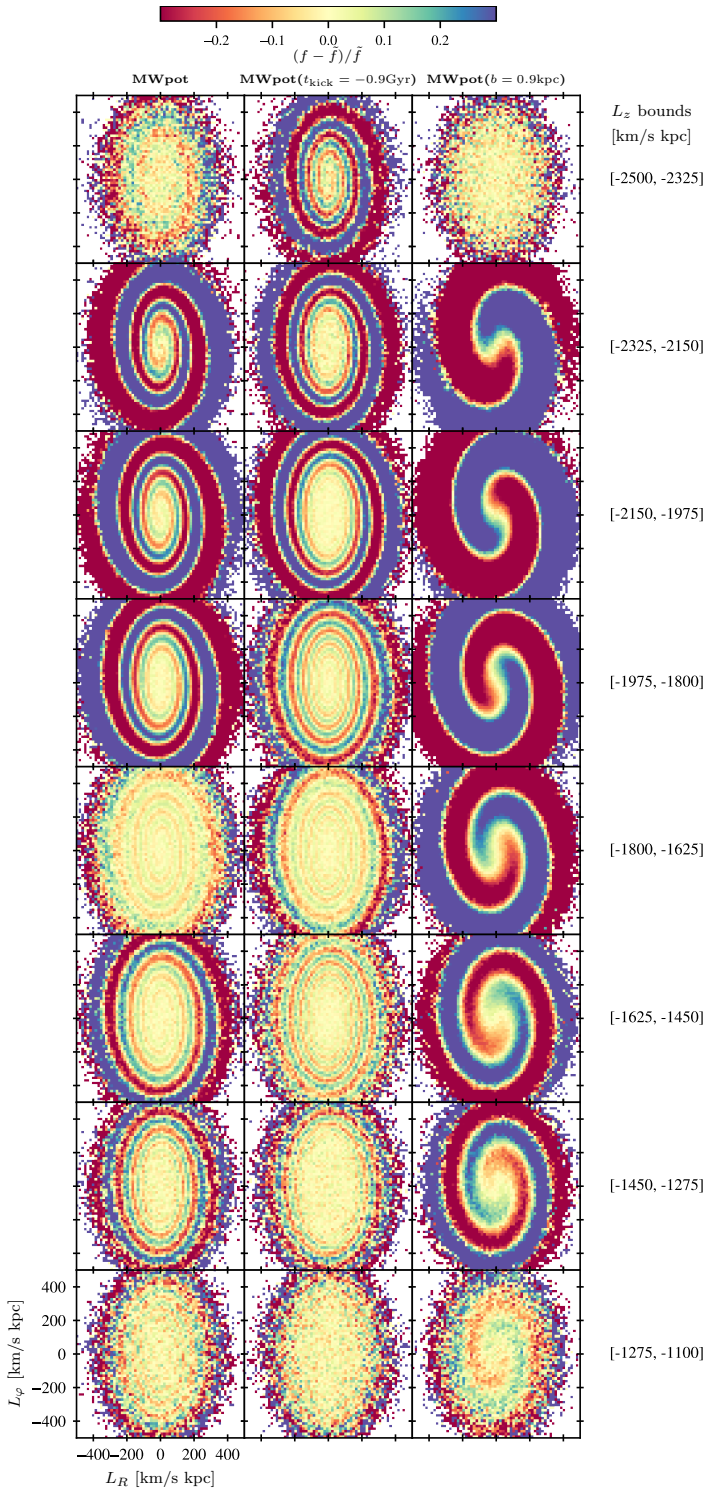

Figure A.1: The angular momentum residuals in $L_R - L_\varphi$ binned in L_z for the velocity-kick perturbation model in Appendix A.2. *First column:* A realisation of the MWpot model, sampled at the location of the data. *Second column:* A realisation of the MWpot model with $t_{\rm kick} = -0.9$ Gyr, the larger time shows a more wound spiral in all bins in comparison to the first model with $t_{\rm tilt} = -0.45$ Gyr. *Third column:* A realisation of the MWpot model with the same timing as the first column, but with the scale height of the disc increased to $b = 0.9$kpc. In the case of the kick model, the spiral feature appears in less L_z bins.

where $v_R = \dot{R}$ and $v_\phi = R\dot{\phi}$. The cylindrical basis vectors are related to the Cartesian basis through

$$\begin{aligned}
\hat{R} &= \cos\phi\,\hat{x} + \sin\phi\,\hat{y};\\
\hat{\phi} &= -\sin\phi\,\hat{x} + \cos\phi\,\hat{y};\\
\hat{z} &= \hat{z}.
\end{aligned} \tag{A.8}$$

Now, finding the cylindrical angular momenta is done trivially via dot product of equations (A.5) and (A.8), this yields

$$\begin{aligned}
L_R &= L_x\cos\phi + L_y\sin\phi;\\
L_\phi &= -L_x\sin\phi + L_y\cos\phi;\\
L_z &= L_z.
\end{aligned} \tag{A.9}$$

To find L_z in cylindrical coordinates, substitute Eqs. (A.6)–(A.7) into the Cartesian L_z expression:

$$\begin{aligned}
L_z &= xv_y - yv_x\\
&= R\cos\phi(v_R\sin\phi + v_\phi\cos\phi) - R\sin\phi(v_R\cos\phi - v_\phi\sin\phi)\\
&= Rv_\phi(\cos^2\phi + \sin^2\phi) = Rv_\phi.
\end{aligned}$$

Further, to find L_R I first express L_x and L_y in cylindrical coordinates:

$$\begin{aligned}
L_x &= R\sin\phi\cdot v_z - zv_R\sin\phi - zv_\phi\cos\phi,\\
L_y &= zv_R\cos\phi - zv_\phi\sin\phi - R\cos\phi\cdot v_z.
\end{aligned} \tag{A.10}$$

After which I apply the projection from Eq. (A.9):

$$\begin{aligned}
L_R &= L_x\cos\phi + L_y\sin\phi\\
&= (R\sin\phi\cos\phi - R\sin\phi\cos\phi)v_z + zv_R(\sin\phi\cos\phi - \sin\phi\cos\phi)\\
&\quad - zv_\phi(\cos^2\phi + \sin^2\phi)\\
&= -zv_\phi.
\end{aligned} \tag{A.11}$$

Finally, for L_ϕ, I follow the same steps as above (projection and substitution)

$$\begin{aligned} L_\phi &= -L_x \sin\phi + L_y \cos\phi \\ &= -Rv_z(\sin^2\phi + \cos^2\phi) + zv_R(\sin^2\phi + \cos^2\phi) \\ &= zv_R - Rv_z. \end{aligned} \tag{A.12}$$

Physical interpretation

The derived cylindrical angular momentum components are

$$\begin{aligned} L_R &= -zv_\phi; \\ L_\phi &= zv_R - Rv_z; \\ L_z &= Rv_\phi, \end{aligned} \tag{A.13}$$

as given in Eq. (2.1) of the main text. To interpret these components, it is useful to consider the geometric picture of an orbital plane traced by a star. For L_R, the component traces the inclination of the orbital plane (away from the galactic vertical axis). On the other hand, L_ϕ informs of the whether the line of nodes has precession due to either non-zero v_r or v_z. Finally, L_z is the standard vertical angular momentum component of the plane, which for a star orbiting in an axisymmetric potential, is conserved.

In the context of the phase spiral discussed in Chapter 2, stars trace ellipses in L_R–L_ϕ space following a disc perturbation. In the picture of orbital planes, the spiral is a correlation of the orbital planes of stars, whose differential precession leads to the formation of a spiral feature. The evolution of the spiral (winding) is governed by the precession of the line of nodes, which occurs as the phases of stars mix after perturbation.

Appendix B

Appendix B

B.1 Sky Coverage Effects

In this Appendix, we test the effects of sky coverage on the fitted model parameters by constructing three samples from the catalogues, an all-sky sample, and SDSS-footprint only sample and a sample with stars only in the northern galactic hemisphere ($b > 0°$).

Figures B.1 and B.2 show the result of the fits. In terms of the travel velocity, the north-only fits are not in agreement with either the 'true' underlying travel velocity (solid line) or the SDSS fit points, where between 20 and 40 kpc they are $> 1\sigma$ apart. The north only fits underestimate the travel velocity at all radii. Also, in the bottom panel of Figure B.1, we find that information about the apex latitude $b_{\rm apex}$ is completely lost, as the north only fit values are all consistent zero at all radii. This is not unexpected, as by definition, the apex direction is defined as the location of the stars with the highest travel velocity, which in the case of these simulations, lies in the region of b <0°.

Furthermore, the fit shows sensitivity to the footprint in which the data lie and $\langle v_r \rangle$ can be shifted towards more negative values as a result. In Figure B.2 we find that using only the SDSS footprint leads to a difference of approximately 10 kms^{-1} in $\langle v_r \rangle$, while $\langle v_\phi \rangle$ and $\langle v_\theta \rangle$ remain roughly consistent. Furthermore, using the all-sky data to fit the bulk motion parameters yields results that are consistent with the underlying mean spherical velocities of the shells of stars from simulation.

To compare the fitted results to the parameter values measured from the simulation in the figures, we include curves from the 20% LMC model from PP20. We show the tracks in Figures B.1 and B.2. The key result in this Appendix is the difference between the different fit points at a given radius, and the difference between the fit points and the model line.

B.2 Separate K Giants and BHB fits

In order to test biases arising from the choice of stellar halo tracer we fit the K giants and BHBs separately in this Appendix. To facilitate a comparison with other fits in this work, we keep the bins the same, with the exception of one fewer bin for the BHBs, as the sample is much smaller are 50+ kpc.

Figures B.3 and B.4 show the results of the fits. In the case of the reflex motion parameters, there is good agreement between the K Giants and BHBs for all three parameters. In the case of the apex longitude $\ell_{\rm apex}$, the BHB fit finds a significantly different result in the 30-40 kpc bin. This could be due to the presence of substructure such as streams. The stream scenario is supported by the result of $\langle v_\theta \rangle$ fits at that distance. The K Giants have ~15 kms^{-1}, while the BHBs have ~-10 kms^{-1}. Bulk polar motion of a subset of stars in the bin will drastically change the mean the bulk halo motion parameters if a stream, or comoving group of stars exists in that bin. All other bulk motion parameters are in agreement, with exception to the 50-60 kpc bin azimuthal velocity $\langle v_\phi \rangle$. We expect this case to also be caused by the presence of substructure, where in that bin the comoving group of stars is deviating the mean halo motion significantly. The travel velocity signal at that radius is underestimated compared to the K giants, and does not display the same increasing $v_{\rm travel}$ signal as the K giants, however the BHB fits at radii >40kpc all have relatively large error bars due to the small number of stars in those bins (< 100 stars).

As in Appendix B.1, to guide the eye between different figures, we include curves from the 20% LMC model from PP20. While we show the tracks in Figures B.1 and B.2, the curves should not be interpreted as targets: the key result in this appendix is the difference between the different fit points at a given radius.

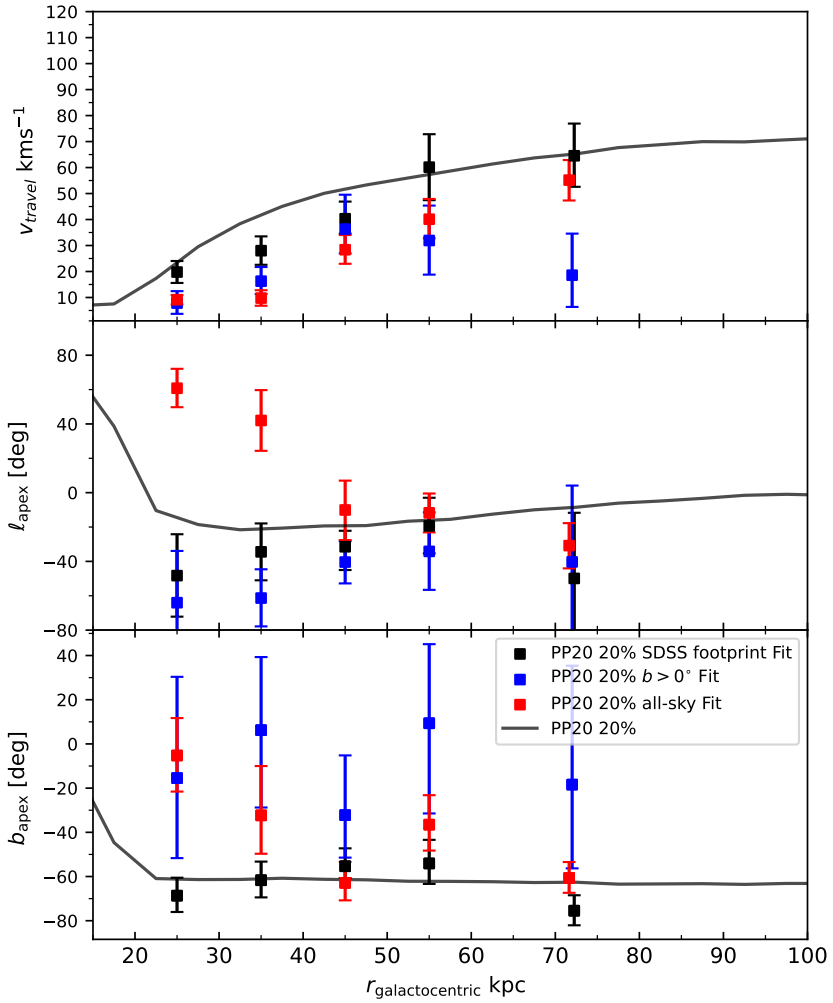

Figure B.1: Sky-coverage tests on a mock sample for recovery of the dipole parameters. The measured values of the travel velocity and apex directions for the PP20 20% model versus the median galactocentric distance of stars in each bin. Top panel: fitted travel velocity in each bin with uncertainties given as the standard deviation of the posterior chains of the parameters. Middle panel: Measured $\ell_{\rm apex}$ values for stars in each bin, note that we restrict the apex longitude to be between 100° and −80°. Bottom panel: Measured $b_{\rm apex}$ values for stars in each bin, where the range of latitude angles are limited to −90° and 60° In each panel, we plot corresponding measurement from the simulation (see text for details in calculating the simulation curves). Colours of model curves and points correspond to the sky coverage used in the test, where the colours red, blue, and black correspond to samples with all-sky, $b > 0°$ and SDSS footprint tests, respectively. Error bars indicate the 1σ width of the posterior distribution for each parameter.

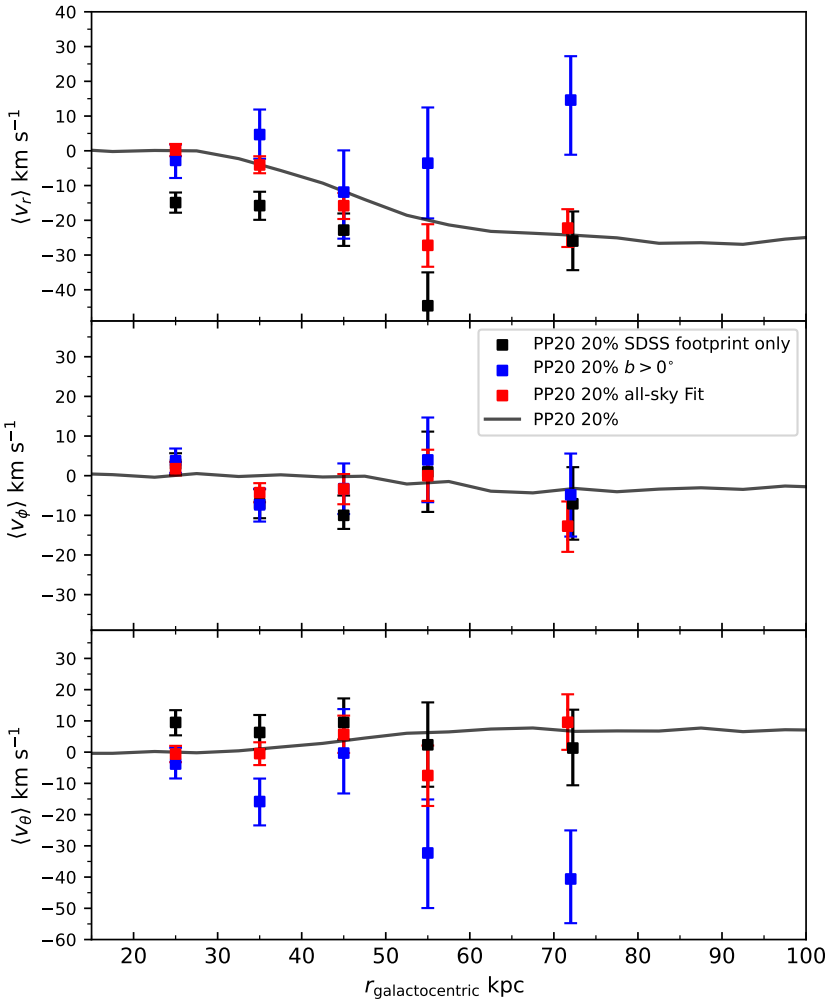

Figure B.2: The measured halo bulk motion parameters as a function of galactocentric radius. Top panel: Mean halo motion in the radial direction.This figure shows the sky-coverage tests on the mock sample in the bulk motion parameters. Middle panel: Mean halo motion in the azimuthal direction(cylindrical rotation). Bottom Panel: mean halo motion in the polar direction. In each panel, we plot corresponding measurements from the set of simulations, which have been reflex corrected. Colours of model curves and points correspond to the sky coverage used in the test, where the colours red, blue, and black correspond to samples with all-sky, $b > 0°$ and SDSS footprint tests, respectively. Error bars indicate the 1σ width of the posterior distribution for each parameter.

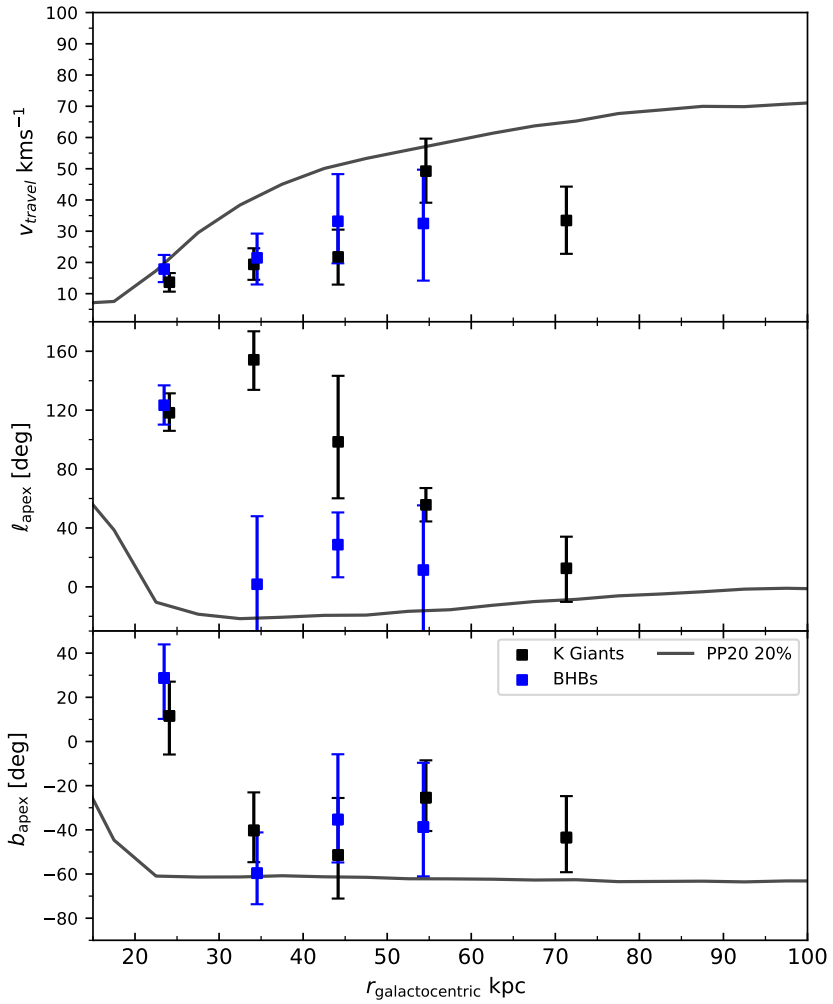

Figure B.3: The measured values of the travel velocity and apex directions for the samples of the K giants and BHBs separately, versus the median galactocentric distance of stars in each bin. Top panel: fitted travel velocity in each bin with uncertainties given as the standard deviation of the posterior chains of the parameters. Middle panel: Measured $\ell_{\rm apex}$ values for stars in each bin, note that we restrict the apex longitude to be between 180° and −20°. Bottom panel: Measured $b_{\rm apex}$ values for stars in each bin, where the range of latitude angles are limited to −90° and 60° In each panel, we plot the measurement from the PP20 simulation as a visual guide. Colours of the points correspond to the star type used in the test, where the colours blue and black correspond to BHBs and K giants respectively. Error bars indicate the 1σ width of the posterior distribution for each parameter.

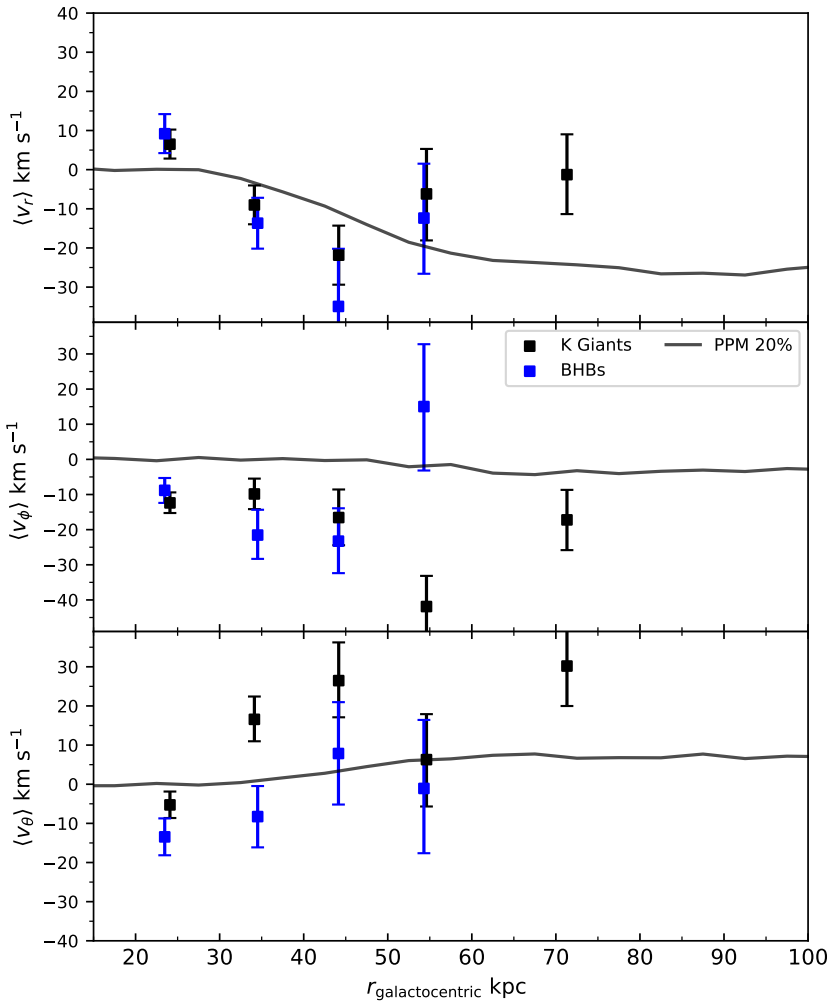

Figure B.4: The measured halo bulk motion parameters as a function of galactocentric radius for the K giant and BHBs tests. Top panel: Mean halo motion in the radial direction.This figure shows measured results for the separate BHB or K giants in the bulk motion parameters. Middle panel: Mean halo motion in the azimuthal direction(cylindrical rotation). Bottom Panel: mean halo motion in the polar direction. In each panel, we plot the measurement from the PP20 simulation as a visual guide. Colours of the points correspond to the star type used in the test, where the colours blue and black correspond to BHBs and K giants respectively. Error bars indicate the 1σ width of the posterior distribution for each parameter.

B.3 Model fits tested on Mock Data

In this Appendix, we test the reflex motion model in Section 3.3 using the PP21 models. In the PP21, an extensive description of the model parameters, live n-body models, LMC trajectory and catalog creation was presented[1]. In this work we perform additional analysis on testing the reflex motion model against the mock catalogues generated from those simulations. We bin the mock catalogues in similar bins as the data, and fit all three PP20 models, to verify the fits are able to recover the change in parameters when varying the mass of the LMC (using the three PP20 models with LMC-MW mass ratios of 0.1, 0.2 and 0.3). We bin the mock catalogs between 20 and 60 kpc with bins widths of 10 kpc, the final bin at 60+ kpc contains all stars with distances $r > 60$ kpc. The total number of stars in the mocks is limited to 5000 to mimic the numbers of stars in the real dataset. We fit the reflex motion model to the binned mock data. Figures B.5 and B.6 show the fitted $\vec{v}_{\rm travel}$ and bulk motion parameters. At most radii, the fit is 1σ consistent with the model lines computed directly from the simulations. In the lowest mass PP20 10% model, the uncertainties are large due to the weak reflex motion signal, while in the bulk motions, the nonzero radial velocity signal is modestly overestimated at all radii.

B.4 Bin Width Variations

In this Appendix we vary the bin centres of the sample to check whether there are significant biases arising from the choice of bin centre. Figures B.7 and B.8 show the results of tests with two different bin centres. We do not see evidence for significant changes when using different bins. Further, the re-centring of the bins exemplifies the continuous behaviour of the model parameters with distance.

As in Appendix B.1, to guide the eye between different figures, we include curves from the 20% LMC model from PP20. While we show the tracks in Figures B.7 and B.8, the curves should not be interpreted as targets: the key result in this Appendix is again the difference between the different fit points at a given radius.

[1]In the models as run with EXP, the LMC is in the wrong present-day position by 90°. In PP21, the coordinate system was rotated to more closely match the present-day location (a transformation that we are free to make, as it only applies a linear offset to $\ell_{\rm apex}$). In these Appendices, we choose not to rotate the coordinate system, to more readily match the simulation snapshots offered in the Data Availability section.

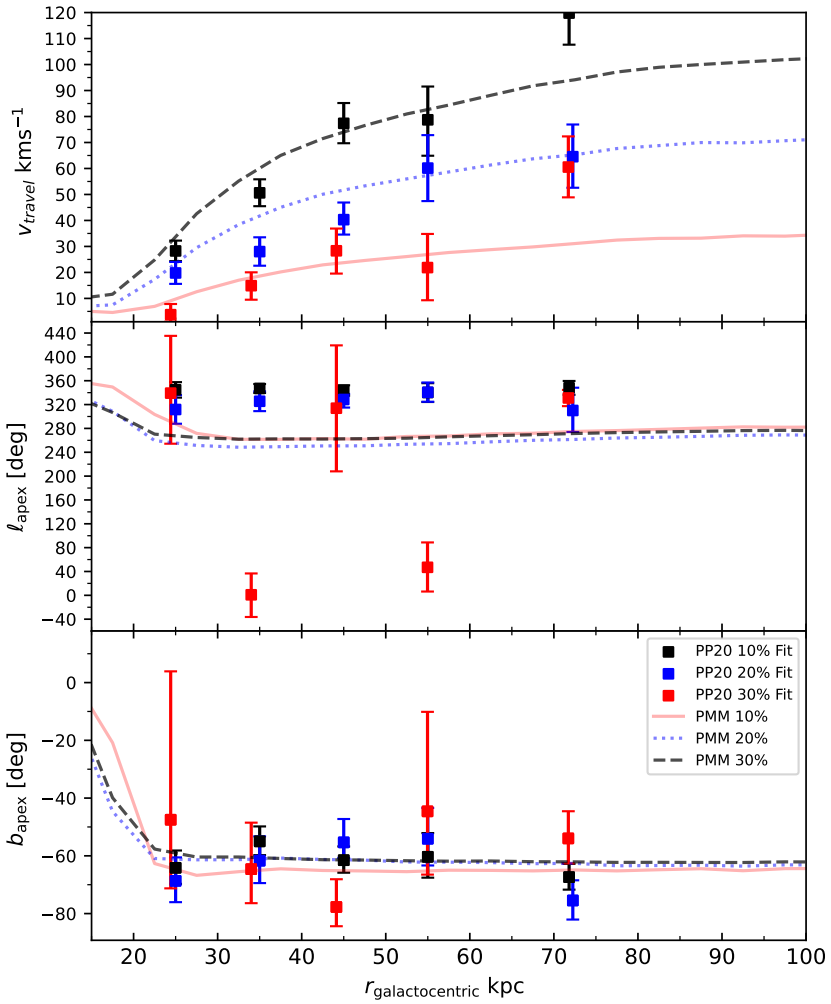

Figure B.5: The measured values of the travel velocity and apex directions for the PP20 models versus the median galactocentric distance of stars in each bin. Top panel: fitted travel velocity in each bin with uncertainties given as the standard deviation of the posterior chains of the parameters. Middle panel: Measured $\ell_{\rm apex}$ values for stars in each bin, note that we restrict the apex longitude to be between 100° and −160°. Bottom panel: Measured $b_{\rm apex}$ values for stars in each bin, where the range of latitude angles are limited to −90° and 15° In each panel, we plot corresponding measurements from the set of simulations (see text for details in calculating the simulation curves). Colours of model curves correspond to the ratio of initial LMC mass to MW mass, where the colours red, blue, and black correspond to the PP20 10%, 20% and 30% models. Error bars indicate the 1σ width of the posterior distribution for each parameter.

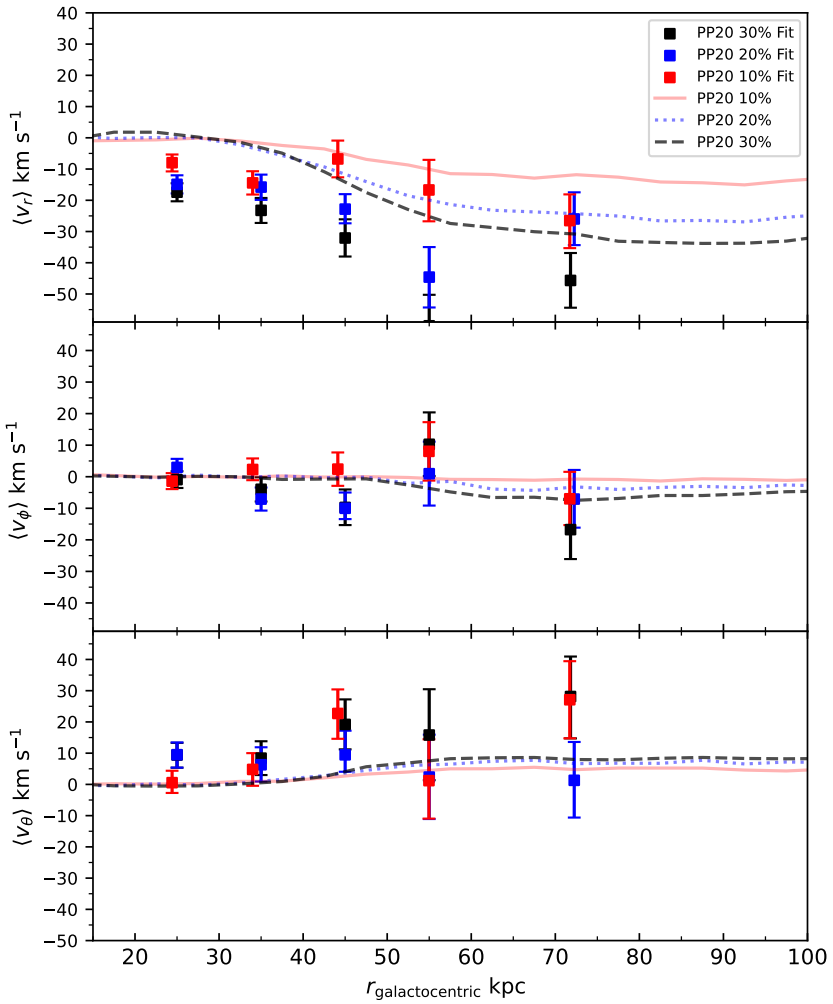

Figure B.6: The measured halo bulk motion parameters as a function of galactocentric radius. Top panel: Mean halo motion in the radial direction. Middle panel: Mean halo motion in the azimuthal direction(cylindrical rotation). Bottom Panel: mean halo motion in the polar direction. In each panel, we plot corresponding measurements from the PP20 set of simulations, which have been reflex corrected. Error bars indicate the 1σ width of the posterior distribution for each parameter.

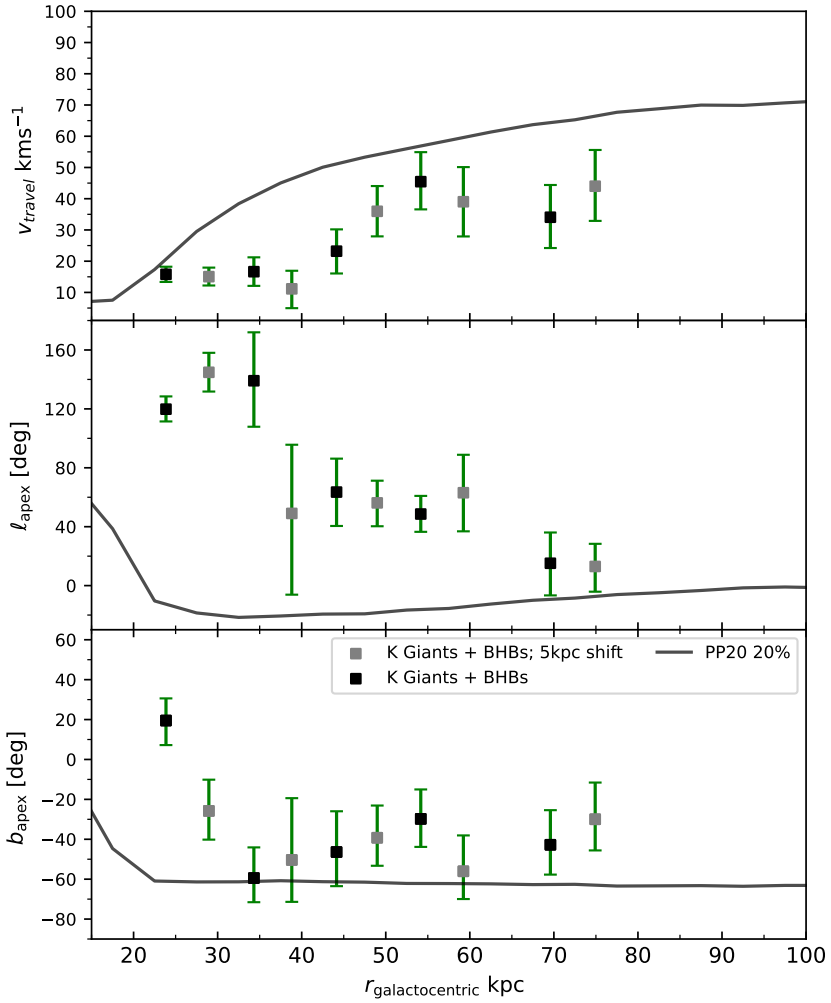

Figure B.7: Tests of the effect of bin choices on the dipole parameters for the combined K giants and BHBs sample. This figure shows measured values of the dipole parameters when varying the bin centre by 5 kpc. Top panel: fitted travel velocity in each bin with uncertainties given as the standard deviation of the posterior chains of the parameters. Middle panel: Measured $\ell_{\rm apex}$ values for stars in each bin, note that we restrict the apex longitude to be between 180° and −20°. Bottom panel: Measured $b_{\rm apex}$ values for stars in each bin, where the range of latitude angles are limited to −90° and 60° In each panel, we plot the measurement from the PP20 simulation as a visual guide. The colours of the model curves correspond to different bin centres, where the grey points are the results of the shifted bin centre, and the black points are the original bins between 20 and 60 kpc. Error bars indicate the 1σ width of the posterior distribution for each parameter.

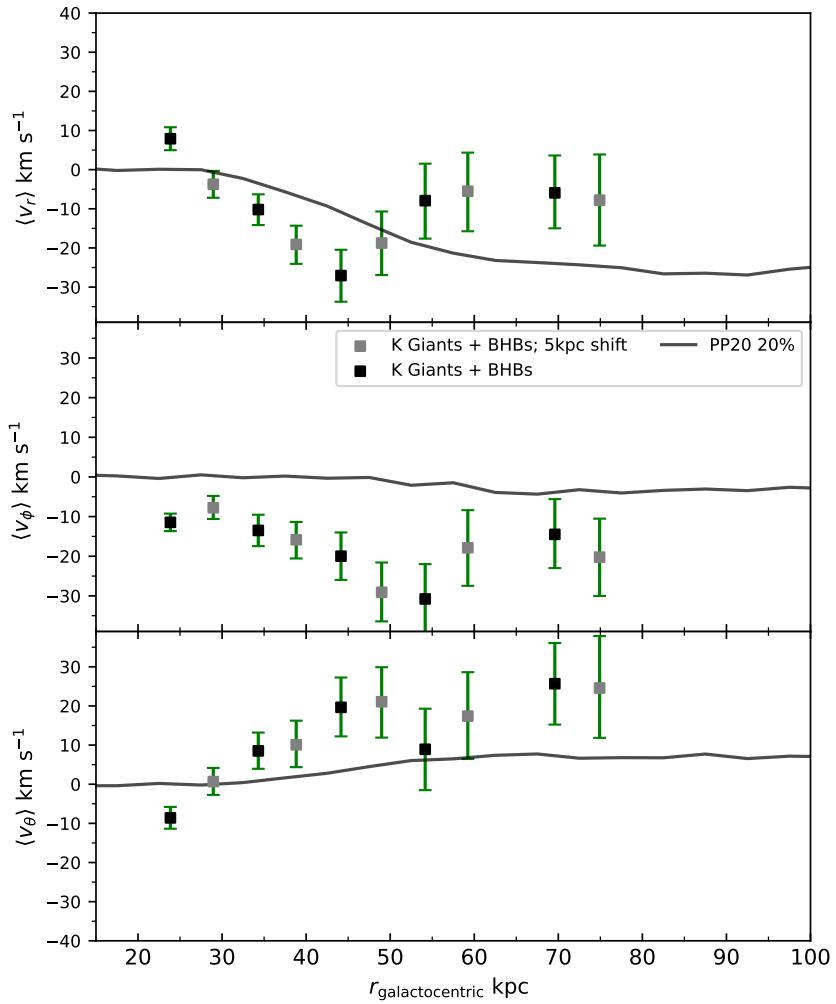

Figure B.8: Tests of the effect of bin choices on the bulk motion parameters for the combined K giants and BHBs sample. Top panel: Mean halo motion in the radial direction.This figure shows measured values of the bulk motion parameters when varying the bin centre by 5 kpc. Middle panel: Mean halo motion in the azimuthal direction(cylindrical rotation). Bottom Panel: mean halo motion in the polar direction. In each panel, we plot the measurement from the PP20 simulation as a visual guide.The colours of the model curves correspond to different bin centres, where the grey points are the results of the shifted bin centre, and the black points are the original bins between 20 and 60 kpc. Error bars indicate the 1σ width of the posterior distribution for each parameter.

Appendix C

Appendix C

C.1 Deformation restricted simulations

In this Appendix we simulate the $\beta = 8.0$ truncated NFW in EXP but restrict the type of deformations that the MW to three scenarios - monopole only, monopole and dipole, monopole, dipole and quadrupole. In the software this is done by running the simulations setting $l_{\rm max}$ to either 0, 1 and 2 respectively (See Table 4.1 for the values of $l_{\rm max}, n_{\rm max}$ used in the main text). These simulations were run to investigate which deformation type cause changes in the apex locations found for most models in Section 4.3 at $\sim$ 50 kpc, connecting density deformations to MW reflex. The results of these simulations are shown in Figure C.1. We find that for the monopole only simulation (red curve in figure) there is no significant change to the apex locations at intermediate radii. However, when a dipole deformation is allowed (green curve), $b_{\rm apex}$ shows a steep rise around 50 kpc followed by a falling after reaching it's maximal value and flattening at large radii. No significant changes in the profile of $b_{\rm apex}$ are found between $l_{\rm max} = 1$ and $l_{\rm max} = 2$ simulations. In $\ell_{\rm apex}$, MW halo deformations with $l_{\rm max} > 0$ both lead to a dip in the profile of the apex longitude at intermediate distances.

Our simple test here shows two main insights: i) the dipole (and monopole) drives changes in the apex locations in our simulations about 50 kpc ii) allowing a quadrupolar deformation (along with monopole and dipole) results in changes to only the apex longitude.

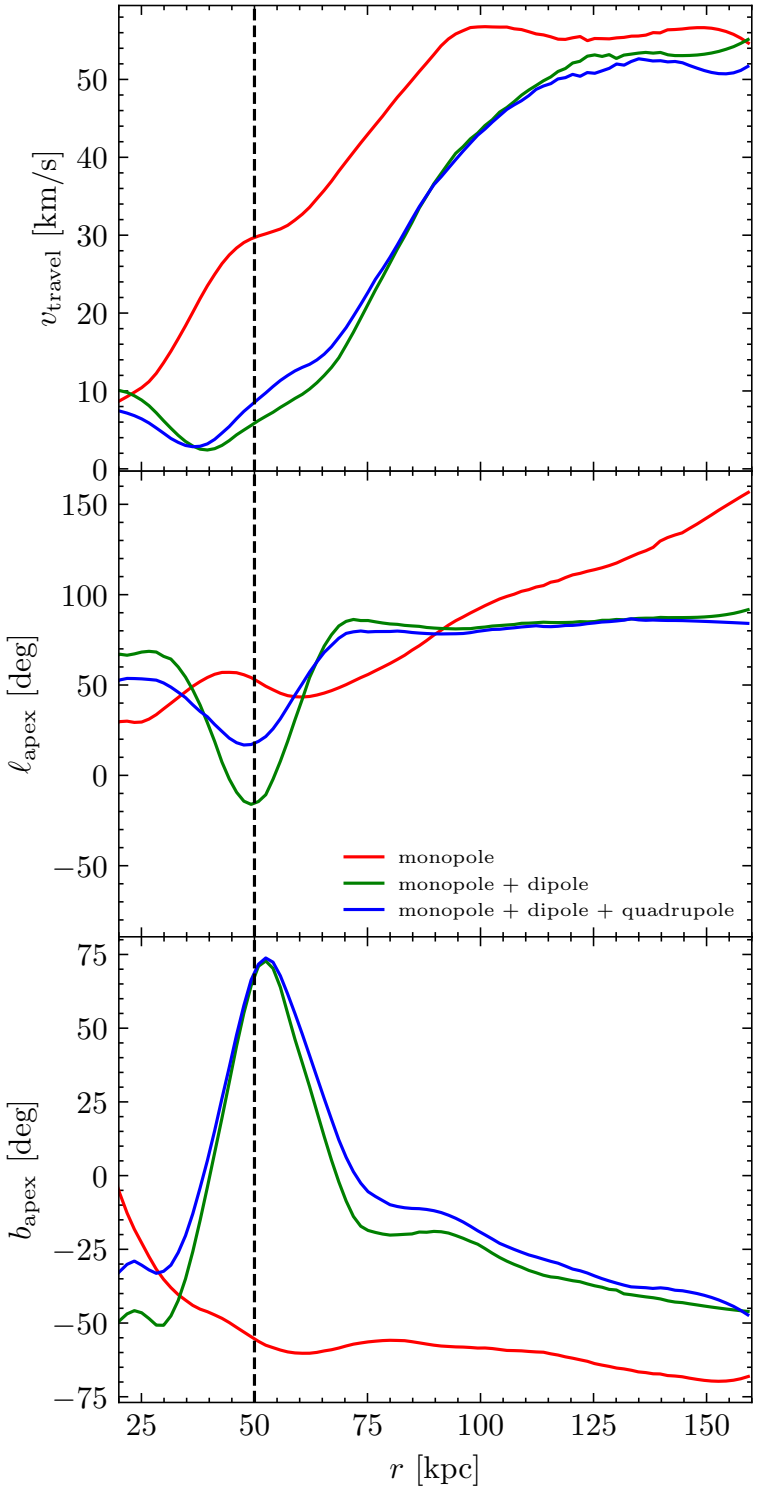

Figure C.1: This figure shows the present day disc travel velocity(top panel), apex longitude(middle panel) and apex latitude (bottom panel) in three simulations of the $\beta = 8.0$ model. Where the type of deformations was restricted to monopole only (red line), monopole and dipole (green line) and monopole, dipole and quadrupole (blue line). The dip in ℓ_{apex} and steep rise in b_{apex} are only present when higher order deformations are allowed. The monopole-only simulations shows little variations in the apex directions at intermediate radii.

Bibliography

Alinder S., McMillan P. J., Bensby T., 2023, A&A, 678, A46

Antoja T., et al., 2018, Nature, 561, 360

Antoja T., Ramos P., López-Guitart F., Anders F., Bernet M., Laporte C. F. P., 2022, A&A, 668, A61

Antoja T., Ramos P., García-Conde B., Bernet M., Laporte C. F. P., Katz D., 2023, A&A, 673, A115

Babcock H. W., 1939, Lick Observatory Bulletin, 498, 41

Banik U., Weinberg M. D., van den Bosch F. C., 2022, ApJ, 935, 135

Bennett M., Bovy J., 2018a, Monthly Notices of the Royal Astronomical Society, 482, 1417

Bennett M., Bovy J., 2018b, MNRAS, 482, 1417

Besla G., Kallivayalil N., Hernquist L., van der Marel R., Cox T., Kereš D., 2010, ApJ, 721, L97

Besla G., Kallivayalil N., Hernquist L., van der Marel R. P., Cox T. J., Kereš D., 2012, Monthly Notices of the Royal Astronomical Society, 421, 2109

Binney J., Schönrich R., 2018, MNRAS, 481, 1501

Binney J., Tremaine S., 2008, Galactic Dynamics: Second Edition

Bird S. A., Xue X.-X., Liu C., Shen J., Flynn C., Yang C., 2019, AJ, 157, 104

Bird S. A., Xue X.-X., Liu C., Shen J., Flynn C., Yang C., Zhao G., Tian H.-J., 2021, ApJ, 919, 66

Bland-Hawthorn J., Gerhard O., 2016, Annual Review of Astronomy and Astrophysics, 54, 529

Bland-Hawthorn J., Tepper-García T., 2021, MNRAS, 504, 3168

Bovy J., 2015, ApJS, 216, 29

Bovy J., Bahmanyar A., Fritz T. K., Kallivayalil N., 2016, The Astrophysical Journal, 833, 31

Buchner J., et al., 2014, A&A, 564, A125

Bullock J. S., Johnston K. V., 2005, The Astrophysical Journal, 635, 931

Byström A., et al., 2024, arXiv e-prints, p. arXiv:2410.09149

Candlish G. N., Smith R., Fellhauer M., Gibson B. K., Kroupa P., Assmann P., 2014a, MNRAS, 437, 3702

Candlish G. N., Smith R., Fellhauer M., Gibson B. K., Kroupa P., Assmann P., 2014b, MNRAS, 437, 3702

Cao C., Li Z.-Y., Schönrich R., Antoja T., 2024, APJ, 975, 292

Chandra V., et al., 2024, arXiv e-prints, p. arXiv:2406.01676

Clowe D., Bradač M., Gonzalez A. H., Markevitch M., Randall S. W., Jones C., Zaritsky D., 2006, The Astrophysical Journal, 648, L109

Conroy C., et al., 2019, The Astrophysical Journal, 883, 107

Conroy C., Naidu R. P., Garavito-Camargo N., Besla G., Zaritsky D., Bonaca A., Johnson B. D., 2021a, Nature, 592, 534

Conroy C., Naidu R. P., Garavito-Camargo N., Besla G., Zaritsky D., Bonaca A., Johnson B. D., 2021b, Nature, 592, 534

Cooper A. P., et al., 2010, MNRAS, 406, 744

Cooper A. P., et al., 2023, ApJ, 947, 37

Correa Magnus L., Vasiliev E., 2021, Monthly Notices of the Royal Astronomical Society, 511, 2610

Correa Magnus L., Vasiliev E., 2022, MNRAS, 511, 2610

Cunningham E. C., et al., 2020, ApJ, 898, 4

Darling K., Widrow L. M., 2019, MNRAS, 484, 1050

Darragh-Ford E., Hunt J. A. S., Price-Whelan A. M., Johnston K. V., 2023, ApJ, 955, 74

Dattathri S., van den Bosch F. C., Weinberg M. D., Banik U., 2025, arXiv e-prints, p. arXiv:2505.23905

Deason A. J., Belokurov V., Koposov S. E., Gómez F. A., Grand R. J., Marinacci F., Pakmor R., 2017, MNRAS, 470, 1259

Deason A. J., et al., 2021, MNRAS, 501, 5964

Dehnen W., 2000, AJ, 119, 800

Dodge B. C., Slone O., Lisanti M., Cohen T., 2022, MNRAS, 518, 2870

Donaldson K., Petersen M. S., Peñarrubia J., 2022, MNRAS, 513, 46

Earp S. W. F., Debattista V. P., Macciò A. V., Cole D. R., 2017, MNRAS, 469, 4095

Eilers A.-C., Hogg D. W., Rix H.-W., Ness M. K., 2019a, ApJ, 871, 120

Eilers A.-C., Hogg D. W., Rix H.-W., Ness M. K., 2019b, ApJ, 871, 120

Einasto J., Saar E., Kaasik A., Chernin A. D., 1974, Nature Astronomy, 252, 111

Erkal D., Belokurov V. A., 2020, MNRAS, 495, 2554

Erkal D., et al., 2019a, Monthly Notices of the Royal Astronomical Society, 487, 2685

Erkal D., et al., 2019b, Monthly Notices of the Royal Astronomical Society, 487, 2685

Erkal D., Belokurov V. A., Parkin D. L., 2020, MNRAS, 498, 5574

Erkal D., et al., 2021a, MNRAS, 506, 2677

Erkal D., et al., 2021b, Monthly Notices of the Royal Astronomical Society, 506, 2677

Fardal M. A., van der Marel R. P., Law D. R., Sohn S. T., Sesar B., Hernitschek N., Rix H.-W., 2018, Monthly Notices of the Royal Astronomical Society, 483, 4724

Feng J. L., 2010, Annual Review of Astronomy and Astrophysics, 48, 495

Feroz F., Hobson M. P., 2008, Monthly Notices of the Royal Astronomical Society, 384, 449

Frankel N., Bovy J., Tremaine S., Hogg D. W., 2023, MNRAS, 521, 5917

Frankel N., Hogg D. W., Tremaine S., Price-Whelan A., Shen J., 2024, arXiv e-prints, p. arXiv:2407.07149

GRAVITY Collaboration et al., 2019, A&A, 625, L10

GRAVITY Collaboration et al., 2021, A&A, 647, A59

Gaia Collaboration et al., 2016, A&A, 595, A1

Gaia Collaboration et al., 2023, A&A, 674, A1

Garavito-Camargo N., Besla G., Laporte C. F. P., Johnston K. V., Gómez F. A., Watkins L. L., 2019a, ApJ, 884, 51

Garavito-Camargo N., Besla G., Laporte C. F. P., Johnston K. V., Gómez F. A., Watkins L. L., 2019b, The Astrophysical Journal, 884, 51

Garavito-Camargo N., Besla G., Laporte C. F. P., Price-Whelan A. M., Cunningham E. C., Johnston K. V., Weinberg M., Gómez F. A., 2021, ApJ, 919, 109

Gómez F. A., Besla G., Carpintero D. D., Villalobos Á., O'Shea B. W., Bell E. F., 2015a, The Astrophysical Journal, 802, 128

Gómez F. A., Besla G., Carpintero D. D., Villalobos Á., O'Shea B. W., Bell E. F., 2015b, The Astrophysical Journal, 802, 128

Grand R. J. J., Pakmor R., Fragkoudi F., Gómez F. A., Trick W., Simpson C. M., van de Voort F., Bieri R., 2023, MNRAS, 524, 801

Guo R., Li Z.-Y., Shen J., Mao S., Liu C., 2024, ApJ, 960, 133

Hernquist L., 1990, ApJ, 356, 359

Hernquist L., Ostriker J. P., 1992, ApJ, 386, 375

Huang S., Carlberg R. G., 1997, ApJ, 480, 503

Hubble E. P., 1926, ApJ, 64, 321

Hubble E., 1929, Proceedings of the National Academy of Science, 15, 168

Hunt J. A. S., Stelea I. A., Johnston K. V., Gandhi S. S., Laporte C. F. P., Bédorf J., 2021, MNRAS, 508, 1459

Hunt J. A. S., Price-Whelan A. M., Johnston K. V., Darragh-Ford E., 2022, MNRAS: Letters, 516, L7

Hunt J. A. S., Price-Whelan A. M., Johnston K. V., McClure R. L., Filion C., Cassese B., Horta D., 2024, MNRAS, 527, 11393

Hunter G. H., et al., 2024, A&A, 692, A216

Iorio G., Belokurov V., 2021, MNRAS, 502, 5686

Jethwa P., Erkal D., Belokurov V., 2016, MNRAS, 461, 2212

Johnston K. V., Law D. R., Majewski S. R., 2005, The Astrophysical Journal, 619, 800

Jónsson V. H., McMillan P. J., 2024, A&A, 688, A38

Kahn F. D., Woltjer L., 1959, ApJ, 130, 705

Kallivayalil N., van der Marel R. P., Besla G., Anderson J., Alcock C., 2013, The Astrophysical Journal, 764, 161

Khoperskov S., Di Matteo P., Gerhard O., Katz D., Haywood M., Combes F., Berczik P., Gomez A., 2019, A&A, 622, L6

Kollmeier J. A., et al., 2017, SDSS-V: Pioneering Panoptic Spectroscopy (arXiv:1711.03234)

Koposov S. E., et al., 2023b, MNRAS, 521, 4936

Koposov S. E., et al., 2023a, Monthly Notices of the Royal Astronomical Society, 521, 4936

Lancaster L., Koposov S. E., Belokurov V., Evans N. W., Deason A. J., 2019, MNRAS, 486, 378

Laporte C. F. P., Minchev I., Johnston K. V., Gómez F. A., 2019, MNRAS, 485, 3134

Law D. R., Majewski S. R., 2010a, ApJ, 714, 229

Law D. R., Majewski S. R., 2010b, The Astrophysical Journal, 714, 229

Li H., Widrow L. M., 2021, MNRAS, 503, 1586

Lilleengen S., et al., 2022, Monthly Notices of the Royal Astronomical Society, 518, 774

Lilleengen S., et al., 2023, MNRAS, 518, 774

Majewski S. R., Skrutskie M. F., Weinberg M. D., Ostheimer J. C., 2003, ApJ, 599, 1082

McMillan P. J., 2016, Monthly Notices of the Royal Astronomical Society, 465, 76

Michtchenko T. A., Barros D. A., Pérez-Villegas A., Lépine J. R. D., 2019, ApJ, 876, 36

Navarro J. F., Frenk C. S., White S. D. M., 1997, ApJ, 490, 493

Newton I., Cotes R., 1713, Philosophiae naturalis principia mathematica. Auctore isaaco newtono, doi:10.3931/e-rara-1237.

Peñarrubia J., Petersen M. S., 2021, MNRAS, 508, L26

Peñarrubia J., Gómez F. A., Besla G., Erkal D., Ma Y.-Z., 2015, Monthly Notices of the Royal Astronomical Society: Letters, 456, L54

Peñarrubia J., Gómez F. A., Besla G., Erkal D., Ma Y.-Z., 2016, MNRAS, 456, L54

Petersen M. S., Peñarrubia J., 2020a, MNRAS, 494, L11

Petersen M. S., Peñarrubia J., 2020b, Monthly Notices of the Royal Astronomical Society: Letters, 494, L11

Petersen M. S., Peñarrubia J., 2021a, Nature Astronomy, 5, 251

Petersen M. S., Peñarrubia J., 2021b, Nature Astronomy, 5, 251

Petersen M. S., Weinberg M. D., 2025, Journal of Open Source Software, 10, 7302

Petersen M. S., Weinberg M. D., Katz N., 2022a, MNRAS, 510, 6201

Petersen M. S., Peñarrubia J., Jones E., 2022b, MNRAS, 514, 1266

Planck Collaboration et al., 2020, A&A, 641, A6

Plummer H. C., 1911a, MNRAS, 71, 460

Plummer H. C., 1911b, MNRAS, 71, 460

Price-Whelan A. M., 2017, The Journal of Open Source Software, 2

Roberts M. S., Rots A. H., 1973, A&A, 26, 483

Rozier S., Famaey B., Siebert A., Monari G., Pichon C., Ibata R., 2022, ApJ, 933, 113

Rubin V. C., Ford Jr. W. K., 1970, ApJ, 159, 379

Schönrich R., Binney J., Dehnen W., 2010a, MNRAS, 403, 1829

Schönrich R., Binney J., Dehnen W., 2010b, Monthly Notices of the Royal Astronomical Society, 403, 1829

Sellwood J. A., Sánchez R. Z., 2010, MNRAS, 404, 1733

Sersic J. L., 1968, Atlas de galaxias australes

Shipp N., et al., 2021, The Astrophysical Journal, 923, 149

Solway M., Sellwood J. A., Schönrich R., 2012, MNRAS, 422, 1363

Toivanen S., Sipila H., 2025, What Is the Milky Way Called in Different Languages, `https://sto.iki.fi/milkyway/`

Tremaine S., 1999, MNRAS, 307, 877

Tremaine S., Frankel N., Bovy J., 2023, MNRAS, 521, 114

Vasiliev E., 2019, MNRAS, 482, 1525

Vasiliev E., 2023a, Galaxies, 11

Vasiliev E., 2023b, Monthly Notices of the Royal Astronomical Society, 527, 437

Vasiliev E., 2024, MNRAS, 527, 437

Vasiliev E., Belokurov V., Erkal D., 2020, Monthly Notices of the Royal Astronomical Society, 501, 2279

Vasiliev E., Belokurov V., Erkal D., 2021, \mnras, 501, 2279

Vera-Ciro C., D'Onghia E., 2016, ApJ, 824, 39

Weinberg M. D., 2023, Monthly Notices of the Royal Astronomical Society, 525, 4962

White S. D. M., Frenk C. S., 1991, ApJ, 379, 52

Widmark A., Laporte C., de Salas P. F., 2021, A&A, 650, A124

Widmark A., Laporte C. F. P., Monari G., 2022a, A&A, 663, A15

Widmark A., Widrow L. M., Naik A., 2022b, A&A, 668, A95

Widrow L. M., 2023, MNRAS, 522, 477

Yaaqib R., Petersen M. S., Peñarrubia J., 2024b, Monthly Notices of the Royal Astronomical Society, 531, 3524

Yaaqib R., Petersen M. S., Peñarrubia J., 2024a, MNRAS, 531, 3524

Yaaqib R., Naik A. P., Peñarrubia J., Petersen M. S., 2025a, MNRAS,

Yaaqib R., Petersen M. S., Peñarrubia J., 2025b, MNRAS, 544, 1820

Yanny B., et al., 2009, The Astronomical Journal, 137, 4377

Zhao H., 1996, MNRAS, 278, 488

de Vaucouleurs G., 1948, Journal des Observateurs, 31, 113

van Albada T. S., Bahcall J. N., Begeman K., Sancisi R., 1985, ApJ, 295, 305

van der Marel R. P., Kallivayalil N., 2014, ApJ, 781, 121